Design and Characterization of a Dust Injector for Future Studies of Tungsten Dust in the STOR-M Plasma

A Thesis Submitted to the College of

Graduate and Postdoctoral Studies

In Partial Fulfilment of the Requirements

For the Degree of Master of Science

In the Department of Physics and Engineering Physics

University of Saskatchewan

Saskatoon

By

Nathan Howard Nelson

Permission to Use

In presenting this thesis in partial fulfillment of the requirements for a Postgraduate degree from the University of Saskatchewan, I agree that the Libraries of this University may make it freely available for inspection. I further agree that permission for copying of this thesis in any manner, in whole or in part, for scholarly purposes may be granted by the professor or professors who supervised my thesis work or, in their absence, by the Head of the Department or the Dean of the College in which my thesis work was done. It is understood that any copying or publication or use of this thesis or parts thereof for financial gain shall not be allowed without my written permission. It is also understood that due recognition shall be given to me and to the University of Saskatchewan in any scholarly use which may be made of any material in my thesis.

Requests for permission to copy or to make other uses of materials in this thesis in whole or part should be addressed to:

Head of the Department of Physics and Engineering Physics
116 Science Place
University of Saskatchewan
Saskatoon, Saskatchewan S7N 5E2
Canada

Dean
College of Graduate and Postdoctoral Studies
University of Saskatchewan
116 Thorvaldson Building, 110 Science Place
Saskatoon, Saskatchewan S7N 5C9
Canada

Dedicated to my family, whom guided me, taught and continue to teach me whilst instilling responsibility and the value of hard work.

Abstract

Dust generation from Plasma Facing Components (PFC) is a problem for tokamaks as they approach suitable reactor conditions. Tungsten dust is especially detrimental in the core, due to associated high Z bremsstrahlung power losses. As Tungsten is a primary candidate for PFC materials in large projects such as ITER, this remains a pressing issue. In order to better understand dust dynamics in tokamaks, a dust injection experiment is proposed for the Saskatchewan Torus-Modified (STOR-M). This experiment will utilize calibrated, spherical tungsten micro-particles. A known mass of these tungsten micro-particles are to be injected into the STOR-M tokamak, with control over the position of the dust plume. This will enable future observation and study of dust dynamics within STOR-M.

In preparation for this experiment, a new dust injector has been designed, based on the fast gas valve for the University of Saskatchewan Compact Torus Injector and subsequently fabricated. An experimental test apparatus was developed to characterize the dust injector. In the experiment, nitrogen gas and dust particles are injected into a test vacuum chamber under various dust injector parameters. Vacuum chamber pressures range from 10^{-4} - 10^{-5} Torr, which is within the operation range of STOR-M. These particles are made visible via laser light scattering and then imaged with a high-speed camera. The collected raw image data with 12-bit intensity resolution was then processed and analysed. This analysis fully characterizes the dust injector in terms of the following parameters: evolution of the injector dust plume, dust particle velocities, amount of gas injected and injected dust mass. These parameters may be controlled by selection of the sieve size which particles pass through and the voltage of a capacitor bank in an electric circuit, used to activate the injector.

Acknowledgments

Thank you to my mother, Holly Nelson for your adamant declaration that I can do whatever I put my mind to, and teaching me to never give up! Thank you to my father, Aaron Nelson for always supporting me to pursue my education and being the first person to show me the joy of problem solving!

To my little brothers, Todd Nelson and Dustin Nelson, thank you for challenging me! Todd, you consistently encourage me to embrace change whilst keeping my mind open to new horizons. Dustin, thank you for guiding me to articulate my ideas in an effective way.

Thank you to my supervisors. Prof. Chijin Xiao, you generously offer your expertise and inspire me with insighful answers to my many questions about fusion, plasma physics and engineering design. Prof. Lénaïc Couëdel, you dedicate even more than what you expect of me! I admire your ethic and am grateful for your influence as we work together.

To my committee members, I am grateful for your supportive feedback and the opportunities to communicate together throughout these years. Prof. Michael Bradley, thank you for the energizing conversations on history, philosophy and physics! Thank you Prof. Doug Degenstein for bearing with me since my undergrad, even though I don't believe in the Leafs.

Thank you Ted Toporowski, James McGregor, Ian Knutson and formerly Dustin Archdekin from the Machine shop, as you ameliorate my approaches to design and making things from scratch!

Thank you to my best friend, Oleksander Ulan Hohol! I cherish how your family has warmly welcomed me throughout the years. Who would have though, all those long miscellaneous conversations really do amount to something important.

Gerald Harrison, you are my mentor! Our evening conversations about science and technological design, along with our many projects have been crucial for me. You shape the practicality of my thinking, which has been an asset throughout this project.

Contents

List of Tables

List of Figures

List of Abbreviations and Symbols

Abbreviation	**Definition**
AC, DC	Alternating Current, Direct Current
ASDEX	Axially Symmetric Divertor Experiment
AUG	Axially Symmetric Divertor Experiment Upgrade
CAD	Computer-Aided Design
CDF	Cumulative Distribution Function
CEA	French Alternative Energies and Atomic Energy Commission
CF	ConFlat
CT	Compact Torus
CTI	Compact Torus Injector
DT	Deuterium - Tritium
FE	Field Emission
FRC	Field-Reversed Configuration
H-Mode	High-Confinement Mode
IDS	Ion Doppler Spectroscopy
IEA	International Energy Agency
ISO	International Organization for Standardization
ITER	International Thermonuclear Experimental Reactor
JET	Joint European Torus
JT-60	Japan Torus-60
K	Large Flange Standard
LHS, RHS	Left Hand Side, Right Hand Side
MHD	Magnetohydrodynamics
N, Ne, Ar	Nitrogen, Neon, Argon
OML	Orbital Motion Limited

PFC	Plasma Facing Component
PTV	Particle Tracking Velocimetry
PWI	Plasma Wall Interactions
SCR	Silicon-Controlled Rectifier
SEE	Secondary Electron Emission
SEM	Scanning Electron Microscope
SOL	Scrape-Off Layer
STOR-M	Saskatchewan Torus-Modified
TEXTOR	Tokamak Experiment for Technology Oriented Research
USCTI	University of Saskatchewan Compact Torus Injector
W	Tungsten

Symbol	**Definition**
a	Secondary resistance scaling
a_{screen}	Screen calibration factor
A	Normalization constant
$\bar{A}_{10\mu m}$	Average area of particles through the 10 μm screen
$\bar{A}_2$	Average area of particles through the secondary screen
$A(t)$	Time dependant amplitude
A_{coil}	Coil area
A_R	Richardson's constant
$\mathbf{A}$	Magnetic vector potential
B	Magnetic field magnitude
B_0	Constant magnetic field
B_r, B_z, B_ϕ	Magnetic field components in cylindrical coordinates
$\mathbf{B}$	Magnetic field
∇B	Magnetic field gradient
c	Speed of light in vacuum
c_s	Specific heat capacity
C	Capacitance
C_{bl}	Background illumination constant

d	Wire gauge
D_0	Inner coil diameter
e	Fundamental charge
E_{avg}	Average energy
E_{max}	Energy of maximum secondary electron emission coefficient
E_s	Plasma species energy
E_e	Electron kinetic energy
$\mathbf{E}$	Electric field
$\mathbf{E}_{ind}$	Induced electric field due to charge separation
$f(s)$	Dust grain size distribution function
$f(v)$	Maxwellian velocity distribution function
$f(x,t)$	Normal distribution function for captured light intensity
f_α	Velocity distribution function of species α
f_{char}	Characteristic frequency
f_1, f_2	Diverging and converging lens focal lengths
F_{ij}	Filtered image matrix elements
F_{roc}	Rocket force magnitude
$\mathbf{F}_{Epst}$	Epstein drag force
$\mathbf{F}_{fric}$	Friction force
$\mathbf{F}_{id}$, $\mathbf{F}_{nd}$	Force of ion and neutral drag
$\mathbf{F}_e$	Electrostatic force
$\mathbf{F}_g$	Gravitational force
$\mathbf{F}_i$	i^{th} force acting on a dust grain
$\mathbf{F}_L$	Lorentz force
$g, \mathbf{g}$	Acceleration due to gravity on earth scalar and vector
G	Gaussian kernel matrix
h_s	Height of the dust injector above the laser sheath
H_α	Radiation produced by hydrogen de-excitation
ΔH	Plasma bulk position
I	Unfiltered image matrix
I_{see}	Secondary electron current
I_{th}	Thermal current

I_e, I_i	Electron and ion current
I_p	Plasma current
I_Z	Impurity ion current
J_0, J_1	Bessel functions of the first kind
$\mathbf{J}$	Current density
k_B	Boltzmann constant
k_z, k_r	Wave number components in cylindrical coordinates
K	Helicity
L_{coil}	Coil inductance
L_{eq}	Equivalent inductance
L_K	Volumetric helicity density
L_p, L_s	Transformer primary and secondary inductance
L_R	Minimum Lawson triple product required for a fusion reactor
L_W	Volumetric energy density
m	Particle mass
m_α	Mass of species, α
m_ν	Evaporated mass
m_{avg}, m_{total}	Average and total mass
m_d	Dust grain mass
m_e, m_i, m_n	Mass of electrons, ions and neutrals
M	Fourier mode number
n	Number density
$\bar{n}_e$	Line average density
n_{0e}	Number Density of electrons far from an external potential
n_{0i}	Number Density of ions far from an external potential
n_{e0}, n_{i0}	Electron and ion number density, far from dust particles
n_{ps}	Primary to secondary turns ratio
n_g	Gas Particle number density
n_i, n_n	Number density of ions and neutrals
N	Number of turns
N_d	Number of injected dust particles
∇	Gradient operator

p	Pressure
P_{loss}	Power loss
P_{rad}	Radiation power
P_F	Fusion power
P_H	Plasma heating and confinement power
$\|\|$	Parallel direction
q	Electric charge
$\|q\|$	Magnitude of electric charge
Q	Ratio of fusion power to plasma heating
Q_{DT}	Ratio of deuterium - tritium fusion power to plasma heating
Q_d	Dust charge
r	Radius
r_0	Initial laser beam radius
r_c	Mean coil radius
r_d	Dust grain radius
r_L	Larmor radius
r_s	Laser sheath radius
R	Electrical resistance
R_{coil}	Coil resistance
R_{dyn}	Dynamic resistance
R_{eq}	Equivalent resistance
R_c	Magnitude of the radius of curvature
R_p, R_s	Transformer primary and secondary resistance
$\mathbf{R}_c$	Radius of curvature
$\bar{s}_{10\mu m}$	Average diameter of particles through the 10 μm screen
$\bar{s}_2$	Average diameter of particles through the secondary screen
s_{avg}	Average diameter
s_{max}	Maximum diameter
S	Particle count scaling factor
t	Time
t_0	Time of dust particle injection
t_{fall}	Time till dust particle arrives in the laser sheath

T	Temperature
T_s	Plasma species temperature
T_d	Dust grain temperature
T_e, T_i, T_n	Temperature of electrons, ions and neutrals
$\mathbf{u}$	Fluid velocity
$\mathbf{u}_i, \mathbf{u}_n$	Ion and neutral fluid velocities
v	Particle speed
v_ν	Speed of evaporated particles
$v_\parallel$	Particle velocity parallel to the magnetic field
$v_\perp$	Particle velocity perpendicular to the magnetic field
v_{ith}	Ion thermal velocity
v_{x0}	Initial horizontal velocity
v_{y0}	Initial vertical velocity
v_x	Horizontal velocity
v_y	Vertical velocity
$\mathbf{v}$	Particle velocity
$\mathbf{v}_d$	Dust particle velocity
V_{int}	Integrated voltage
V_l	Loop voltage
w	Laser beam width
W	System energy
W_B	Magnetic energy
W_f	Work function
Z	Atomic number
$\langle Z \rangle$	Charge State of Ions
α	Eigenvalue of magnetic field curl
β	Ratio of plasma to magnetic pressure
γ_{sei}	Secondary electron emission coefficient due to ions
Γ_ν	Evaporation flux
δ_{Epst}	Epstein drag coefficient
δ_{max}	Maximum secondary electron emission coefficient
δ_{see}	Secondary electron emission coefficient due to electrons

δ_s	Skin depth
ϵ_0	Permittivity of free space
η	Ion drag coefficient
η_d	Dust charge distribution coefficient
θ	Angle made by laser and dust plume
λ	Constraint constant
λ_D	Debye Length
μ	Mean
μ_0	Permeability of free space
$\boldsymbol{\mu}$	Magnetic moment
ν_{nd}	Dust-neutral collision frequency
ξ	Evaporation symmetry factor
Ξ_{net}	Total power flux incident on the dust grain surface
ρ	Resistivity
$\rho(\mathbf{r})$	Plasma charge density
σ	Standard deviation
σ_c, σ_s	Collection and scattering momentum transfer cross sections
σ_d, μ_d	Size distribution function parameters
τ	Time constant
τ_E	Confinement time
$\phi(\mathbf{r})$	Local plasma potential
ϕ_s	Surface electric potential
Φ	Magnetic flux
$\tilde{\Phi}_f$	Plasma potential fluctuation
ψ	Gauge function
ω	Angular frequency
ω_c	Cyclotron frequency
$\boldsymbol{\Omega}$	Angular velocity

Chapter 1

Introduction

1.1 A New Source of Energy

What fundamentally drives this project is the same as many others in the field of plasma physics. Plasma is considered the fourth and most abundant form of matter in the universe and thus, understanding its behaviour is paramount to understanding many phenomena in our universe [1]. Furthermore, fusion energy holds the promise to supply humanity with the energy required to sustain our current ways of life, and carry ourselves forward through to a new age of human endeavour.

In our modern world there is a constant demand for energy, a staggering 80% of which is met by fossil fuels [2, 3]. Based on present known supply, when inferring future usage rates, one arrives at the conclusion that oil and natural gas supplies will start to decline within 50-60 years from the current date [3]. However, one must insist on the fact that these are consumption models, and as such, are dependant on proper initial conditions. The location and extraction of new reserves is obviously one of these conditions. Confidence in these models is indeed, further enhanced by the decline in new oil discoveries over the past 40 years [4].

Energy consumption trends are currently on the rise (Figure 1.1). The International Energy Agency (IEA) is anticipating this increase in demand, and that fossil fuels will fill the vast majority of it until 2030 [5]. The increasing short term demand on fossil fuels cannot stand to help humanities situation, with an ever diminishing primary resource. If

one takes a pessimistic approach, and sees that our dependence on fossil fuels continues to grow as our supplies dwindle, a very bleak mood is set for the future. What is certain, is that a new energy scheme is needed. We just don't know how soon, or how gradual the change will be.

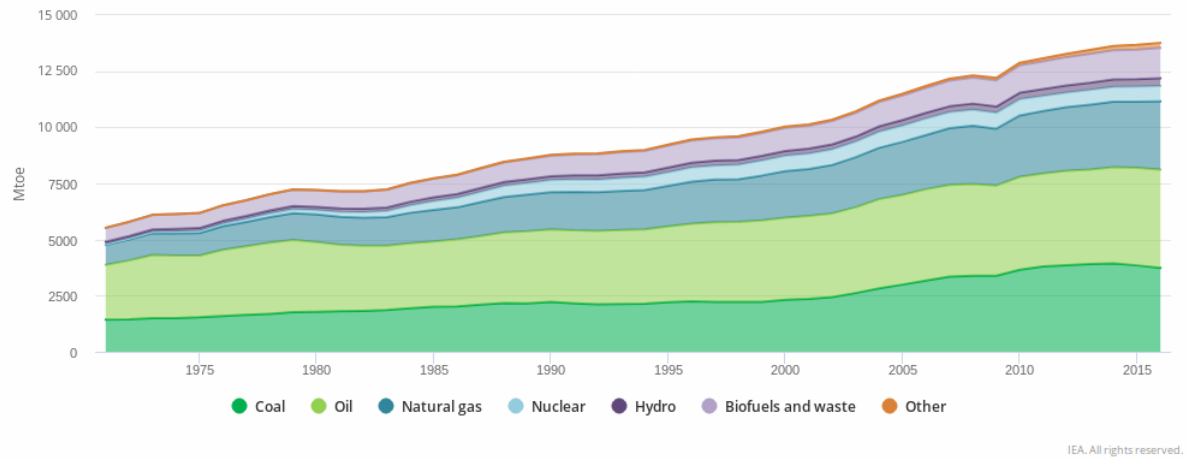

Figure 1.1: World Energy Supply [6].

1.2 Why Fusion?

Fusion energy is generated from the union of two light nuclei. This releases massive amounts of energy per fusion reaction. A single deuterium - tritium reaction in particular, produces 17.6 MeV worth of energy [7]. For reference, this is five orders of magnitude higher than the heat released per combustion reaction of octane (utilized in hydrocarbon blends for gasoline [8]). We hope to harness as many such reactions as possible to produce power in a fusion reactor. Current fission power is at least an order of magnitude more energy dense than solar power in terms of geographic space required for production [9]. Nuclear fusion power output should also be scalable, past that of a nuclear fission reactor, with enhanced safety and sustainability.

Unfortunately, multiple popular scheme's for nuclear fusion reactors will still contain radioactive materials, such as the tritium in the fuels and the activated materials from the chamber wall. However, a relatively low amount of nuclear material is present when compared to fission reactors. In particular, high energy neutron bombardment

as a consequence of the deuterium - tritium reactions within the reactor, will result in transmutations of the reactor wall materials, rendering them radioactive. Fortunately, this would still generate only a fraction of the waste produced in fission reactors.

1.3 Advances in Fusion Devices

There are multiple issues in achieving net fusion energy gain. Perhaps the predominant issue is that fusion plasmas are prone to many different instabilities, which have been researched extensively and continue to be to this day. Though problems still remain in confinement of hot fuels in the plasma state, much progress has been made. In particular, the performance of fusion research devices has increased dramatically over the last 50 years [10]. This is a definite credit to advances in technology along with a better understanding of plasma dynamics.

The requirement for fusion power production is represented by the Lawson Triple Product (Lawson Criterion) [7]:

$$nT_i\tau_E > L_R, \tag{1.1}$$

Here, n and T_i are respectively the plasma density and ion temperature and L_R is a constant which represents the minimum value for reactor conditions, varying for different types of fusion reactions. τ_E is the confinement time defined as:

$$\tau_E = \frac{W}{P_{loss}}, \tag{1.2}$$

where, W is the energy of the system and P_{loss} is the energy loss rate from the system. Progress in the production of fusion power is best visualized through Figure 1.2. Here the light blue section highlights the operation regime with appropriate ion temperature and Lawson criterion, where bremsstrahlung losses are tolerable. The Upper right hand corner encloses regions with three blue arcs, showing conditions for various energy gains of 0.1 - 1 and the ignition condition where fusion gain is much greater than unity, enabling self heating of the fuel in order to produce net power output for generation of electricity. Note

the values of Q_{DT} indicated along theses blue arcs. DT represents the deuterium-tritium reaction, which is the easiest fusion reaction to achieve on earth. By definition, Q is the ratio of fusion power produced (P_F) to the power required to heat and confine the plasma (P_H), succinctly written as:

$$Q = \frac{P_F}{P_H}. \tag{1.3}$$

$Q = 1$, known as break-even, has already been surpassed in the JT-60 tokamak. Unfortunately, this was interpreted based on the plasma parameters achieved without actually using tritium. JET holds the record for DT fusion, with a $Q \approx 0.67$. Currently, a new large tokamak reactor, ITER is under construction in France as an international collaborative effort to achieve net energy gain fusion. This will serve as a proof of concept for future reactor designs. ITER will aim for $Q \geq 10$, in hopes of reaching ignition conditions, where the DT plasma will produce enough energy to sustain itself [11]. In addition to this, enough energy must be created to power the various systems which the tokamak relies on.

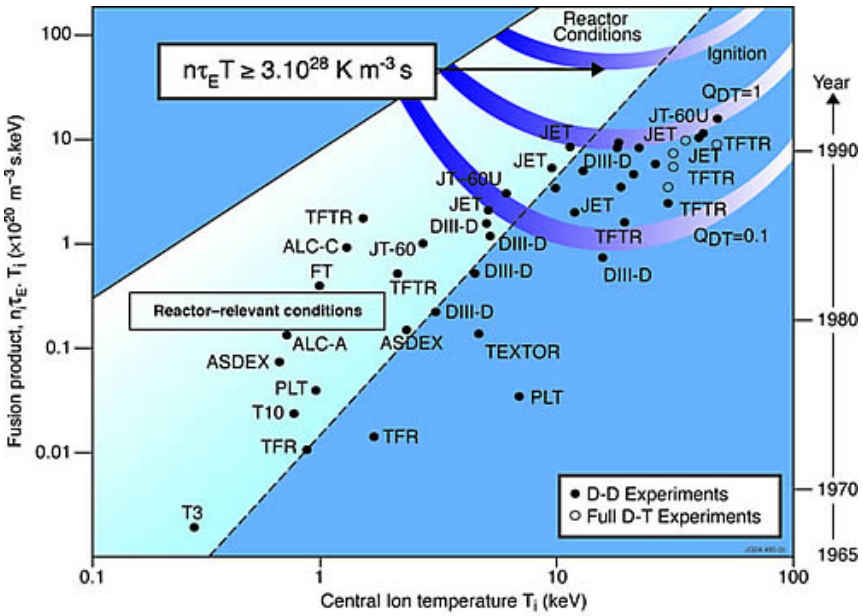

Figure 1.2: Progress of Tokamak Parameters Towards Break-Even [12].

1.4 Motivation

As noted in Section 1.3, much has been done in the effort to achieve terrestrial fusion. However, these advances have still left us with multiple remaining issues. In particular, the plasma interaction with the chamber wall is very important, especially in the effort to advance plasma confinement time and steady-state operation. Plasma-wall interactions (PWI) are essentially a collection of processes which occur when a plasma exchanges mass and energy with its container.

PWI have the potential to cause material to sputter off the chamber wall and enter the plasma [13]. Some of these materials may be in the form of particle grains which are relatively large in size (approximately nm to μm scale in diameter). These particle grains are known as plasma dust [14]. Dust may migrate through the plasma in a complex manner, essentially merging with the plasma as a new species, serving only to increase the complexity of the situation. Dust is an impurity, which generally has a negative impact on plasma parameters. High heat flux regions, such as the divertor plates in an ITER like tokamak, can possibly generate even more dust, due to the high number of energetic particles impinging on the material surface. If enough dust happens to reach the plasma core, the entire reaction may be quenched due to enhanced radiation loss caused by impurities [15].

As the reactor wall necessarily experiences extreme temperatures, caused by particle bombardment from the plasma, effort has been made to direct this heat flux in an intelligent way. The previously mentioned divertor plates are a result of this effort. In a region known as the scrape-off layer (SOL), open magnetic field lines intercepted by the divertor plates adjacent to the chamber wall, guide the plasma towards these divertor plates [16]. Upon colliding with these plates, particles may be exhausted from the tokamak via the pump, located below the divertor. Figure 1.3 illustrates the interception of open field lines by the divertor plates with a cross-sectional diagram of a tokamak.

With the use of a divertor which directs high heat fluxes towards itself, most of the wall which surrounds the plasma may be composed of a low Z material with lesser thermal resistance than that of the divertor material [17]. Low Z materials are generally favourable

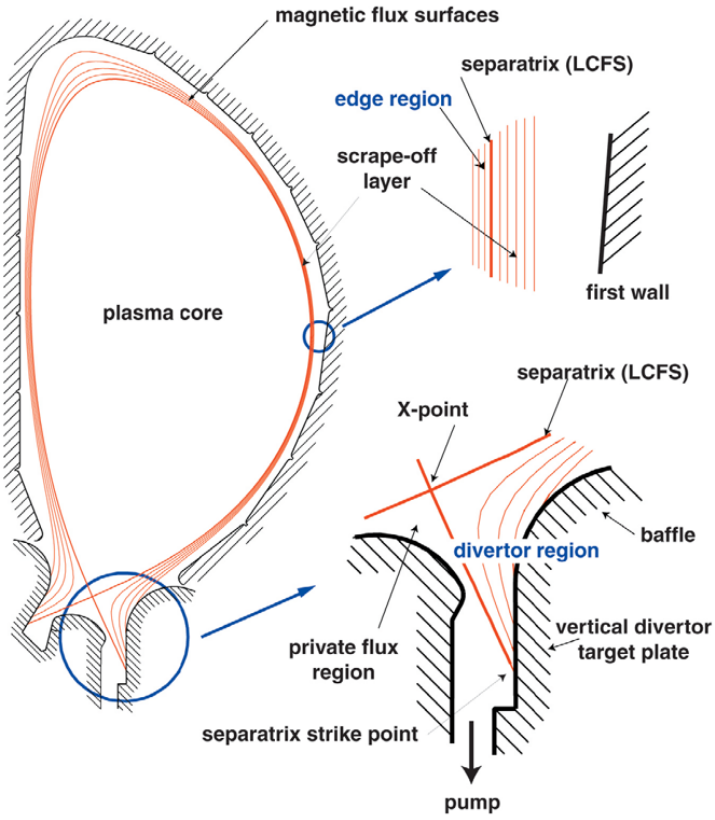

Figure 1.3: Directing the Scrape-Off Layer in an ITER-Like Tokamak [16]. Displayed is a cross sectional view of an ITER-Like tokamak. The core plasma is encircled by closed magnetic flux surfaces, as opposed to the open field lines, past the separatrix, along the wall and divertor. These open magnetic field lines guide particles in the scrape of layer past the x-point, where they strike the divertor. Afterwards, these particles may be pumped out of the tokamak.

for the plasma facing wall, as bremsstrahlung radiation, which is $\propto Z^2$, detrimentally cools the fusion plasma. Beryllium could be used for a suitable first wall material, on account of having the lowest Z of any stable material and sufficient thermal and mechanical properties when a divertor is used [18].

Any material chosen for the divertor plates must be able to withstand bombardment by particles from the plasma [19], at least for long enough to give the fusion reactor sufficiently long operation time between maintenance. As such, tungsten appears to be an obvious choice, possessing the highest melting point of any known element. Tungsten also possess other favourable characteristics. In particular, tungsten has low tritium fuel retention compared to other carbon-based alternatives [20]. Tungsten has a very high thermal conductivity, which makes it effective for heat exchange in order to lower the

divertor plate temperature and extract energy from the reactor. Tungsten is also resistant to sputtering and erosion from incident particles [21]. Additionally, tungsten is resistant to neutron damage and activation caused by incident neutrons produced from the DT fusion reaction within the plasma [22].

Unfortunately, tungsten is not a perfect divertor material. Hydrogen causes the surface of tungsten to swell and blister [23]. These blisters may retain tritium fuel inside the surface. If blisters were to pop, the influx of tritium fuel may have adverse effects on operation. Furthermore, tritium retention in the wall yields a potential explosion hazard during a loss of coolant event [24]. Such an incident would cause a pressure increase in the chamber and potentially form oxygen, via electrolysis. This may cause the retained tritium within the wall to violently react.

Tungsten also interacts unfavourably with helium, as it tends to destroy the integrity of the surface, resulting in the growth of long, tendril like nanostructures known as fuzz [25]. This fuzz is easily removed from the surface and facilitates one key mechanism of dust generation from tungsten.

It should be noted that, dust impurity build up over the operation time span of a fusion reactor is yet another issue that must be addressed. Even if dust may be kept from the core, it should optimally be managed without reactor shutdown to clean the machine.

In order to prevent core dust accumulation and reactor shutdown, we must have a greater understanding of dust dynamics. This type of research can be carried out either in larger tokamaks where dust production occurs naturally or in smaller tokamak, such as STOR-M in the Plasma Physics Laboratory at the University of Saskatchewan, where the plasma parameters are not high enough to produce appreciable amount of dust to be observed. In the latter case, a controlled dust injection experiment may be designed and implemented. This research project to study the behavior of artificially introduced tungsten dust particles is inspired by the need to solve problems caused by dust in future fusion reactors.

1.5 Thesis Objective

In order to study tungsten dust dynamics in the Saskatchewan Torus Modified (STOR-M) plasma, a dust injector needs to be designed, tested and characterized. The dust injector will allow for appropriate dust delivery amounts and dust positioning within a STOR-M discharge. Machined, spherical tungsten micro particles will be used as the dust in this experiment, simulating the type of material liberated from a tungsten divertor, exposed to a fusion plasma.

Many new, custom pieces of equipment are required for characterization and operation of the dust injector. A particular procedure has been devised for dust injector calibration. Additionally, a particle tracking velocimetry (PTV) algorithm, utilizing trackpy software is programmed and implemented to analyze the trajectory of dust particles dispersed from the dust injector [26]. From this data, the velocity and time-dependent spatial distribution of dust particles may be determined for various dust injector parameters.

1.6 Thesis Outline

This thesis is divided into 7 Chapters. Chapters 2-4 deal with the theory and equipment that will be needed for experiment. Chapter 2 provides background information on the physics of magnetic confinement fusion, relevant to tokamak devices. Chapter 3 goes into detail on impurities in reactor plasmas, with focus on dust generation and dynamics within a tokamak. Chapter 4 focuses on the equipment used for both dust injector calibration, and the foreseen dust injection experiment.

The proceeding chapters 5-7 concern themselves with the experiments and data analyses conducted in this thesis. Chapter 5 focuses on the dust injector characterization and calibration. Chapter 6 is a summary of the results of the experiments conducted and a proposal for the dust injection experiment in STOR-M.

Chapter 2

Background

2.1 Plasma Physics Fundamentals

2.1.1 Plasma Temperature

For a gas in thermal equilibrium, the most likely distribution of gas particle velocities is given by the Maxwellian distribution function [7]. For one-dimension this is given as follows:

$$f(v) = A \exp\left(-\frac{1}{2}\frac{mv^2}{k_B T}\right). \tag{2.1}$$

Here, m is the mass of gas particles, v is the speed of gas particles, k_B is the Boltzmann constant and T is the temperature of the gas. A serves as a normalization constant, such that:

$$n_g = A \int_{-\infty}^{\infty} \exp\left(-\frac{1}{2}\frac{mv^2}{k_B T}\right) \mathrm{d}v, \tag{2.2}$$

where, n_g is the number density of gas particles. From this velocity distribution function, we define the average kinetic energy of the system (E_{avg}) as follows:

$$E_{avg} = \frac{\int_{-\infty}^{\infty} \frac{1}{2} m v^2 f(v) \mathrm{d}v}{\int_{-\infty}^{\infty} f(v) \mathrm{d}v}. \tag{2.3}$$

For one dimensional particle velocity, this integral simplifies to:

$$E_{avg} = \frac{1}{2} k_B T. \tag{2.4}$$

In general, there is an additional $\frac{1}{2}k_BT$ of energy per degree of freedom. In order to avoid confusion based on the dimensionality of the problem, it is convention in plasma physics to drop the factor of $\frac{1}{2}$ and give the temperature (T_s) for a particular plasma species in units of its energy:

$$E_s = k_B T_s. \tag{2.5}$$

As an example, for a plasma which contains electrons at an energy of 1 eV, the electron temperature is, $\frac{1\text{eV}}{k_B} = 11600\text{K}$. For equal ion and electron temperatures within the plasma, a single plasma temperature may be declared.

2.1.2 Debye Length

A plasma is defined as a quasi-neutral ionized gas. The effect of quasi-neutrality is associated with Debye screening, which serves to limit the range of electrostatic forces within the plasma. Over distances much larger than the Debye length of a charged particle, the overall number of ions and electrons within the plasma tends to be the same, as local charge imbalances average out. The effects of the screened plasma potential may be seen from Poisson's equation:

$$\nabla^2 \phi(\mathbf{r}) = \frac{-\rho(\mathbf{r})}{\epsilon_0}, \tag{2.6}$$

where, $\phi(\mathbf{r})$ is the electric potential within the plasma, due to an applied electric field, $\rho(\mathbf{r})$ is the charge density of the plasma and ϵ_0 is the permittivity of free space. For Boltzmann distributed electrons, responding to the potential $\phi(\mathbf{r})$ and relatively slow ions due to their significantly larger mass, we attain:

$$\rho(\mathbf{r}) = e n_{0e} \exp\left(\frac{-e\phi(\mathbf{r})}{k_B T}\right) - e\langle Z \rangle n_{0i}. \tag{2.7}$$

Here, e is the fundamental charge, n_{0e} and n_{0i} are respectively the density of electrons and ions far from the potential and $\langle Z \rangle$ is the charge state of ions.

With the assumption that $k_B T >> e\phi(\mathbf{r})$, the exponential term may be Taylor expanded, yielding:

$$\rho(\mathbf{r}) = e n_{0e} \left(1 - \frac{e\phi(\mathbf{r})}{k_B T}\right) - e\langle Z \rangle n_{0i}. \tag{2.8}$$

Considering quasi-neutrality far away from the potential $\phi(\mathbf{r})$, we have:

$$n_{0e} = \langle Z \rangle n_{0i} = n, \tag{2.9}$$

where, n is the plasma number density. As a result, equation 2.8 becomes:

$$\rho(\mathbf{r}) = -\frac{e^2 n \phi(\mathbf{r})}{k_B T}. \tag{2.10}$$

Substituting equation 2.10 into equation 2.6, results in:

$$\nabla^2 \phi(\mathbf{r}) = \frac{e^2 n}{\epsilon_0 k_B T} \phi(\mathbf{r}). \tag{2.11}$$

The solution to this equation is an exponential, which decays with distance, $\mathbf{r}$. This decay constant is a characteristic length scale known as the Debye length:

$$\lambda_d = \sqrt{\frac{\epsilon_0 k_B T}{e^2 n}}. \tag{2.12}$$

2.1.3 Basic Magnetic Confinement

Consider the Lorentz force acting on a single charged plasma particle in a uniform magnetic field. The particle will rotate as a simple harmonic oscillator with a frequency known as the cyclotron frequency [7]:

$$\omega_c = \frac{|q|B}{m}, \tag{2.13}$$

where, $|q|$ is the magnitude of the particles charge and B is the magnitude of the magnetic field. This rotation is around a single magnetic field line, who's position is known as the

guiding center. The fixed radius of particle rotation is known as the Larmor radius [7]:

$$r_L = \frac{mv_\perp}{|q|B}, \tag{2.14}$$

where, $v_\perp$ is the speed of the particle perpendicular the the magnetic field. The magnetic field only confines the motion of the particle perpendicular to the field line, thus, the particle is still free to move parallel to the magnetic field. This results in a final helical trajectory illustrated by Figure 2.1.

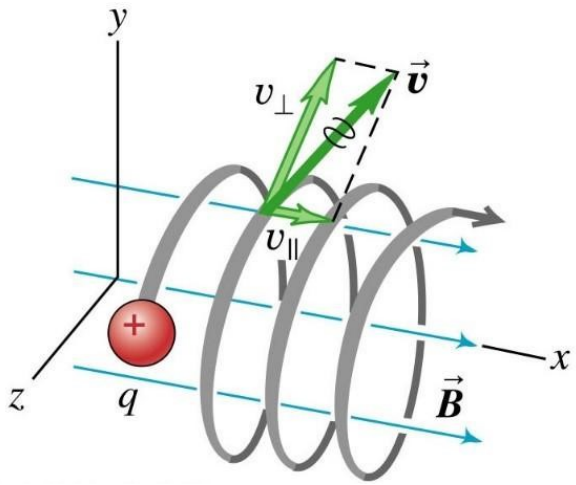

Figure 2.1: Gyromotion of a Positively Charged Particle [27]. Figure from Harvard University. The helical path of a positively charged particle is shown. Here, the particle rotates clockwise around the magnetic field, though a negative charge would rotate counterclockwise.

2.2 Toroidal Magnetic Confinement

2.2.1 Toroidal Geometry

A torus/toroid is essentially a cylinder, which has been uniformly bent into a symmetric ring, such that the ends of the cylinder connect with one another. This shape is illustrated in Figure 2.2. From this geometry, we define two primary directions. The toroidal direction follows the torus as it connects with itself as indicated by the blue arrow, while the poloidal direction wraps around the torus, through the hole at the center as indicated by the red arrow.

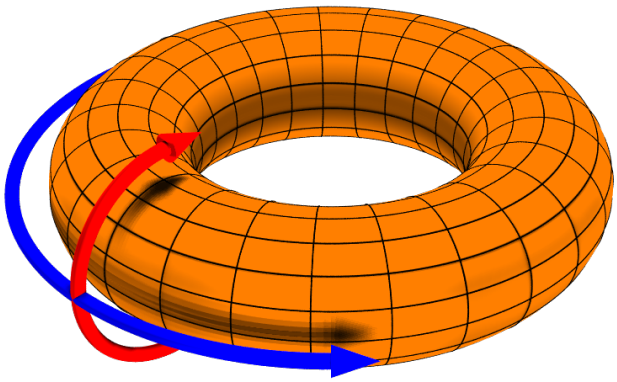

Figure 2.2: Geometry of a Torus [28]. Figure from Dave Burke. Here the toroidal direction is indicated in blue, while the poloidal direction is indicated in red, looping through the apparent donut hole.

Toroidal geometry serves as an improvement to linear confinement, as it removes losses associated with particles travelling parallel to magnetic field lines. This is a simple consequence of the fact that the magnetic field lines of a torus may wrap around themselves indefinitely. Unfortunately, new problems arise as a consequence of toroidal geometry.

2.2.2 Magnetic Field Configuration

The magnetic field strength within a toroid reduces at increasing radius, r, from the center (illustrated in Figure 2.3). This is a natural consequence of the higher density of field lines located at smaller radii compared to larger radii, resulting from the curved magnetic field. This results in a magnetic field gradient, causing particles within the torus to experience a grad-B drift given by [7]:

$$\mathbf{v}_{\nabla B} = \pm\frac{1}{2}v_{\perp}r_L\frac{\mathbf{B}\times\nabla B}{B^2}. \tag{2.15}$$

Here, $v_{\perp}$ is the velocity of charged particle perpendicular to the magnetic field, r_L is the Larmor radius, $\mathbf{B}$ is the magnetic field of the toroidal plasma, ∇B is the magnetic field gradient and B is the magnitude of the magnetic field. Additionally, the curved magnetic field of the torus leads to a curvature drift given by [7]:

$$\mathbf{v}_R = \frac{mv_{\parallel}^2}{qB^2}\frac{\mathbf{R}_c\times\mathbf{B}}{R_c^2}, \tag{2.16}$$

where, $v_{\parallel}$ is the particle velocity parallel to the magnetic field, q is the particle charge, $\mathbf{R}_c$ is the radius vector of the curved magnetic fields and R_c is the magnitude of magnetic field radius. Both grad-B and curvature drift share a common characteristic. They act in opposite directions for negative and positively charged particles. This ultimately results in charge separation, indicated by the gyromotion of electrons and ions in Figure 2.3. The separation of charge in the torus generates an electric field, which results in $\mathbf{E} \times \mathbf{B}$ drift, given as follows [7]:

$$\mathbf{v}_{\mathbf{E}\times\mathbf{B}} = \frac{\mathbf{E}_{ind} \times \mathbf{B}}{B^2}. \tag{2.17}$$

where, $\mathbf{E}_{ind}$ is the induced electric field in the torus, due to charge separation. This $\mathbf{E} \times \mathbf{B}$ drift causes charged particles to move towards the chamber wall as shown in Figure 2.3, thus breaking confinement. In order to counteract this, a toroidal current, producing a poloidal magnetic field is utilized to rotate the plasma in the poloidal direction. As the plasma twists, the direction of the $\mathbf{E} \times \mathbf{B}$ drift changes. Over one full poloidal rotation, the net outward drift is effectively negated, as on average, particles will drift the same amount in opposing directions.

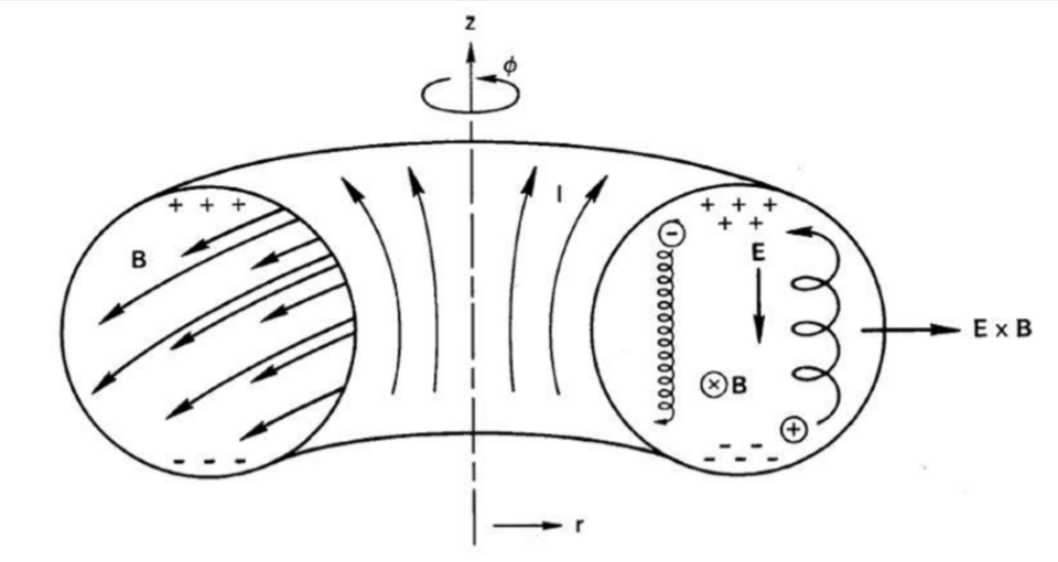

Figure 2.3: Particle Drifts in a Toroidal Field [29]. Figure from Chen F.F.

2.3 Tokamak

2.3.1 Basics

A tokamak is a particular type of magnetic confinement fusion device. The purpose of this device is to confine a hot fusion plasma, with as high a density as possible, for as long as possible. This enables ignition condition and maximizes energy output of the device.

Tokamaks generally operate with a large toroidal magnetic field, generated by the high current discharge of a large capacitor bank, through the toroidal field coils. This large magnetic field serves to confine the motion of particles along toroidal magnetic field lines. The magnetic field of another high current discharge is coupled to the inner poloidal (direction indicated by Figure 2.4) field coils (Ohmic heating coils) of the tokamak, via iron core transformer. This field creates a current, via transformer action in the conductive plasma (Section 2.3.2) acting as the secondary coil in the transformer. The plasma current then heats the plasma via Ohmic heating. The other important role of the plasma current is to produce a magnetic field around it in the poloidal direction. This poloidal field is combined with the externally induced toroidal magnetic field, producing helical magnetic field lines, which are a favorable magnetic configuration for plasma equilibrium and stability. The current carrying plasma column has a tendency to expand horizontally in the radial direction via the so called hopping effect. In order to counterbalance this expanding force, a set of coils is needed to generate a vertical magnetic field which interacts with plasma to generate an radially inward force.

The Saskatchewan Torus - Modified (STOR-M) is the tokamak that will be used for the foreseen dust injection experiment [30]. The discharge duration for this device is typically between 30 - 60 ms. This sets the time scale for experiments which may be conducted in the device.

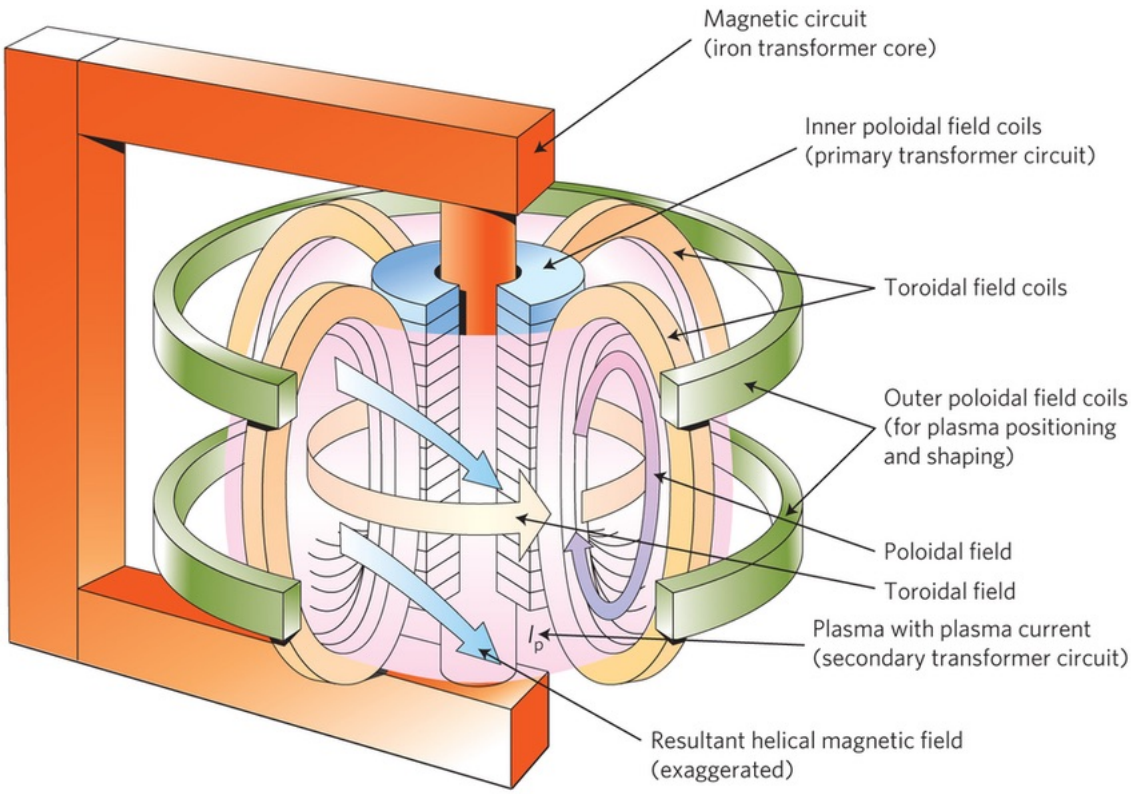

Figure 2.4: General Tokamak Schematic [31]. Figure from the Anthropocene Institute.

2.3.2 Ideal MHD

Ideal MHD is the treatment of plasma as a conductive, quasi-neutral fluid. This model works especially well for fusion plasma's. In general, a tokamak plasma follows the generalized ohm's law [32]. The plasma resistivity is taken to be sufficiently low that it can be neglected.

$$\mathbf{E} + \mathbf{u} \times \mathbf{B} = \rho \mathbf{J} \approx 0, \tag{2.18}$$

where $\mathbf{E}$ is the electric field of the tokamak plasma, $\mathbf{u}$ is the fluid flow velocity, ρ is the plasma resistivity and $\mathbf{J}$ is the tokamak current density. We can now show that the magnetic flux (Φ) remains static in the tokamak [33].

$$\Phi = \int \mathbf{B} \cdot \mathrm{d}\mathbf{S}, \tag{2.19}$$

thus,

$$\frac{\mathrm{d}}{\mathrm{d}t}\Phi = \int_S \frac{\partial}{\partial t}\mathbf{B} \cdot \mathrm{d}\mathbf{S} + \int_l \mathbf{B} \times \mathbf{u} \cdot \mathrm{d}\mathbf{l}. \tag{2.20}$$

Here, d$\mathbf{S}$ represents the differential surface element which the plasma flux tube passes through and d$\mathbf{l}$ represents the line element corresponding to the boundary of d$\mathbf{S}$. Application of Faraday's law and Stokes Theorem yields:

$$\frac{\mathrm{d}}{\mathrm{d}t}\Phi = -\int_S \nabla \times (\mathbf{E} + \mathbf{u} \times \mathbf{B}) \cdot \mathrm{d}\mathbf{S}. \tag{2.21}$$

The RHS of equation (2.21) is equal to zero by equation (2.18), therefor magnetic flux is static. The result of this "Frozen in flux" is that the magnetic field is now confined to move with the plasma. From this, we may determine the plasma flow and position in the tokamak by measuring the magnetic field. These quantities give crucial information on plasma confinement and stability which we wish to control.

Finally, appreciation is warranted for the complexity of magnetized fusion plasmas. The purpose of the magnetic field is to confine the plasma in a particular configuration. However, it is clear that the motion of the plasma fluid affects magnetic field and vice versa. Succinctly, the magnetic field is a part of the plasma.

2.3.3 Fueling

Unlike fission reactors, where a large amount of fuel is inserted into the reactor until spent and replaced, fusion reactors limit the amount of fuel in the reactor at any given time to ensure they are heated to the high temperature required for fusion. Common fueling schemes include gas puffing and frozen pellet injection. With these methods, fuels will be ionized quickly in the peripheral and trapped by the magnetic field there. Only a small fraction of fuel migrates to the reactor core to participate in fusion reactions and the majority of fuel, together with the exhaust gas, is pumped out to be separated for re-use.

The core of the fusion plasma, where most fusion events occur, has the highest thermal pressure. This thermal pressure tends to force fresh fuel from the core. Thus, a mechanism is required which can directly fuel the core. This is not a trivial task. Based on the view of many experts, the only promising central fuelling scheme is the injection of the compact torus at high velocities.

2.4 Compact Torus

2.4.1 Basics

The Compact Torus (CT) is one particular type of stable, self contained magnetic structure/ plasmoid [34]. The magnetic field structure of the CT is similar to that of a tokamak, however, both toroidal and poloidal magnetic field components are induced by the current in the plasmoid (Figure 2.5) [35]. The toroidal current produced a magnetic moment, $\boldsymbol{\mu}$. Also, the poloidal field of the CT is comparable to the toroidal field, as opposed to the tokamak, where the toroidal field is dominant. A synonym for the CT is the aptly named Spheromak.

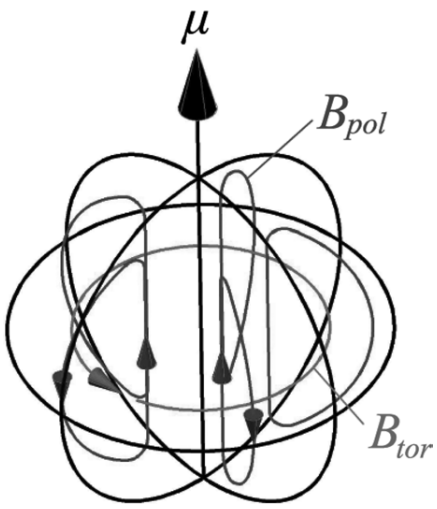

Figure 2.5: Compact Torus Field [35]. Figure from Olynyk G. and Morelli J.

2.4.2 Equilibrium

The CT represents a particular form of plasma equilibrium. In particular, this is a Taylor state. In this state, an equilibrium (minimum energy level) is achieved while conserving magnetic helicity. Magnetic helicity is essentially a measure of the twist of the magnetic field lines. In addition, an essential property of the plasma is determined by it's beta value (the ratio of the plasma thermal pressure to the magnetic pressure). In a low beta plasma we have [7, 32]:

$$\beta = \frac{p}{\frac{B^2}{2\mu_0}} \approx 0, \tag{2.22}$$

where $p = nk_BT$ is the thermal pressure. n, k_B, and T are respectively density, Boltzmann's constant and temperature. $\frac{B^2}{2\mu_0}$ is the magnetic pressure and B is the magnetic field of the CT. We ignore the thermal pressure term in the equation of motion since it is negligible compared to the magnetic pressure, resulting in:

$$\rho\frac{\mathrm{d}\mathbf{u}}{\mathrm{d}t} = \mathbf{J}\times\mathbf{B} - \nabla p \approx \mathbf{J}\times\mathbf{B} = 0. \tag{2.23}$$

Thus, we find that non-trivial solutions for $\mathbf{B}$ occur only with $\mathbf{B} \parallel \mathbf{J}$. In this case, Ampere's law yields [36]:

$$\nabla\times\mathbf{B} = \mu_0\mathbf{J} = \alpha\mathbf{B}. \tag{2.24}$$

Note that from this, α is a scalar function.

It can now be shown that the conserved magnetic helicity and minimized energy in the CT is synonymous with the force free field configuration given by equation (2.24). In order to do so, we must minimize the energy of the CT, which is approximately its magnetic energy (W_B) with respect to constrained helicity (K). This is equivalent to the following first order variational problem [36]:

$$\delta W_B - \lambda\delta K = 0, \tag{2.25}$$

where,

$$W_B = \frac{1}{2\mu_0}\int B^2\,\mathrm{d}V = \int L_W\,\mathrm{d}V, \tag{2.26}$$

$$K = \int \mathbf{A}\cdot\mathbf{B}\,\mathrm{d}V = \int L_K\,\mathrm{d}V. \tag{2.27}$$

Here, L_W and L_K simply represent their corresponding integrands and $\mathrm{d}V$ represents the differential volume element of the compact torus. $\mathbf{A}$ is the magnetic vector potential, which establishes the usual relationship:

$$\mathbf{B} = \nabla\times\mathbf{A}. \tag{2.28}$$

From this point, we can now show that K is purely a functional of B. Utilizing equations (2.24) and (2.28) we find:

$$\nabla \times \mathbf{A} = \frac{1}{\alpha} \nabla \times \mathbf{B}, \tag{2.29}$$

which yields an explicit equation for $\mathbf{A}$, defined up to an arbitrary gauge dependant function, ψ:

$$\mathbf{A} = \frac{1}{\alpha} \mathbf{B} + \nabla \psi. \tag{2.30}$$

Substituting equation (2.30) into equation (2.27) gives:

$$K = \int \left(\frac{1}{\alpha} \mathbf{B} + \nabla \psi \right) \cdot \mathbf{B} \, \mathrm{d}V = \int \frac{1}{\alpha} B^2 \, \mathrm{d}V + \int_S \psi \mathbf{B} \cdot \mathrm{d}\mathbf{S}. \tag{2.31}$$

Since $\nabla \cdot \mathbf{B} = 0$, the second term in K may be turned into an integral over the surface of the CT, utilizing divergence theorem. For magnetic configurations where $\mathbf{B} = 0$ on the surface of the CT, this second term vanishes. From the form of equation (2.31), we see that the magnetic energy of the CT is directly related to it's helicity. Thus, in the same way the magnetic energy of the CT is conserved while the configuration is stable, so too must helicity be conserved [37]. Finally, we may now simply show our variational equation is satisfied. Evaluating the LHS of equation (2.25) we have:

$$\int \left(\frac{\partial L_W}{\partial B} - \lambda \frac{\partial L_K}{\partial B} \right) \delta B \mathrm{d}V = \int \left(\frac{B}{\mu_0} - \frac{2\lambda B}{\alpha} \right) \delta B \mathrm{d}V = 0, \tag{2.32}$$

which holds in the case of constant α and for the appropriate choice of the constraint parameter λ.

The analytic solution to equation (2.24) has the following basis in Bessel functions for a cylindrical symmetry [38]. The solution is periodic along the axial direction (z direction), with no azimuthal variation. The equations which describe the magnetic field of the CT are as follows:

$$B_r = -B_0 \frac{k_z}{k_r} J_1(k_r r) \cos(k_z z), \tag{2.33}$$

$$B_z = -B_0 J_0(k_r r) \sin(k_z z), \tag{2.34}$$

$$B_\phi = -B_0 \frac{\alpha}{k_r} J_1(k_r r) \sin(k_z z). \tag{2.35}$$

When plotted, the vector fields yields a familiar physical result, provided the application of appropriate boundary conditions. k_r can be determined at $r = a$ (the wall used to generate the plasmoid). The axial length of the plasmoid determines k_z. The following solution was generated in MATLAB:

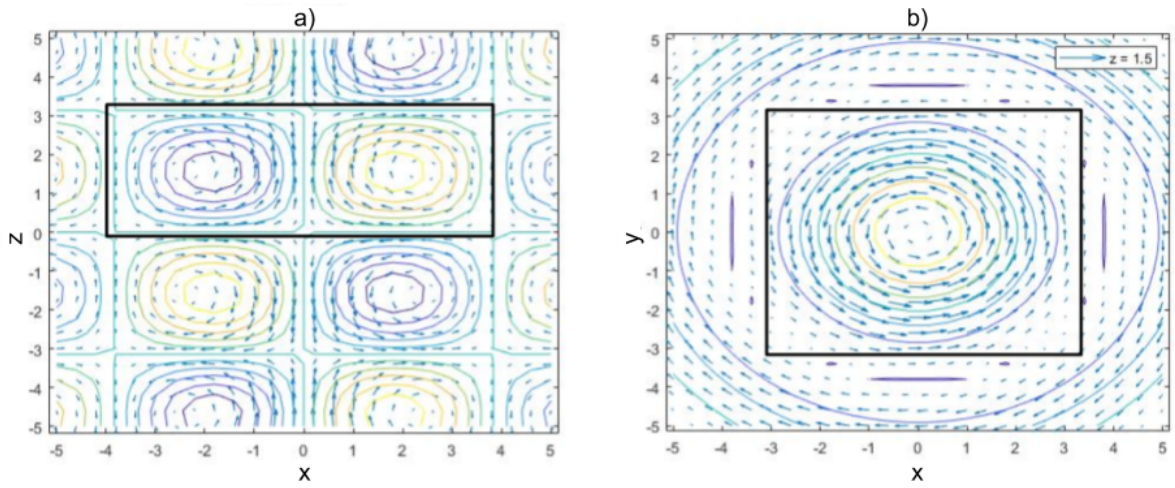

Figure 2.6: Two-dimensional Plots of the Vector Field of the Compact Torus. These plots were attained by using equations (2.33) - (2.35) (Physical solution is inside the black box). Both the Bessel function and sinusoidal functions go to zero at the boundary of the CT's container. Here z is the symmetric axis of the CT. a) represents the x-z field slice of the CT at y = 0. b) represents the x-y field slice at z = 1.5. For simplicity $k_r = k_z = B_0 = \alpha = 1$ in this image.

2.5 Importance of CT Fuelling in Fusion

The ability to fuel a fusion reaction is of utmost importance for a functional reactor. The CT is especially well suited for this role. The CT is able to inject fuel directly into the core of the reactor, add toroidal (direction indicated by Figure 2.4) momentum and suppress modal fluctuations of the plasma. In particular, the CT increases the plasma's Lawson triple product [39].

Another benefit to the CT is the large amount of fuel that can be ejected at one time. A similar type of plasmoid injection serves as the fueling method of choice for General

Fusion's magnetized target fusion reactor [40].

There are however other candidates for reactor fueling. Neutral Beam injection is also capable of injecting energetic particles to heat the plasma, but is not an efficient fueling scheme. This serves as the fueling method of choice for Tri-Alpha Energy's reactor named "Norman" [41]. However, the field-reversed configuration (FRC) which is similar to the CT, also plays a key role in device operation. In addition to this, the company also deals with CT injection.

2.6 CT-Tokamak Interaction

There is a wealth of physics to be explored concerning plasmoid interactions with the tokamak. The onset of high confinement mode (H-mode) is a particularly interesting phenomena. When a CT is injected into a tokamak plasma, the magnetic fields in the CT and tokamak reconnect. The resulting plasma confinement has been found to improve in the STOR-M tokamak in the experiments conducted at the University of Saskatchewan. Additionally, certain poloidal MHD modes are suppressed while others are enhanced within the original tokamak plasma [42, 43].

The yellow section of Figure 2.7 shows the effect of the STOR-M discharge due to CT injection. Loop voltage (V_l) and plasma current(I_p) remain unaffected. Line average density ($\bar{n}_e$) and confinement time (τ_E) both increase significantly. This represents an increase in plasma confinement and shows that the CT successfully penetrated the tokamak plasma. The plasma bulk position (ΔH) is seen to move outwards significantly, indicating increased thermal pressure causing this expansion. H_α is seen to decrease. This particular hydrogen emission is used to characterize the plasma interaction with the wall. Reduced H_α essentially characterizes better confinement. Finally, $\tilde{\Phi}_f$ represents the fluctuation of the plasma potential. These fluctuations seem to be stabilized by the CT. The M = 2 Fourier mode of magnetic fluctuations is shown to be suppressed.

It should be pointed out that the time scales of the tokamak discharge duration (see Figure 2.7) is about 20-30 ms, while the CT penetration time is on the order of 10 μs, due to its high velocity, in the range of 100 km/s or 0.1 m/μs within STOR-M.

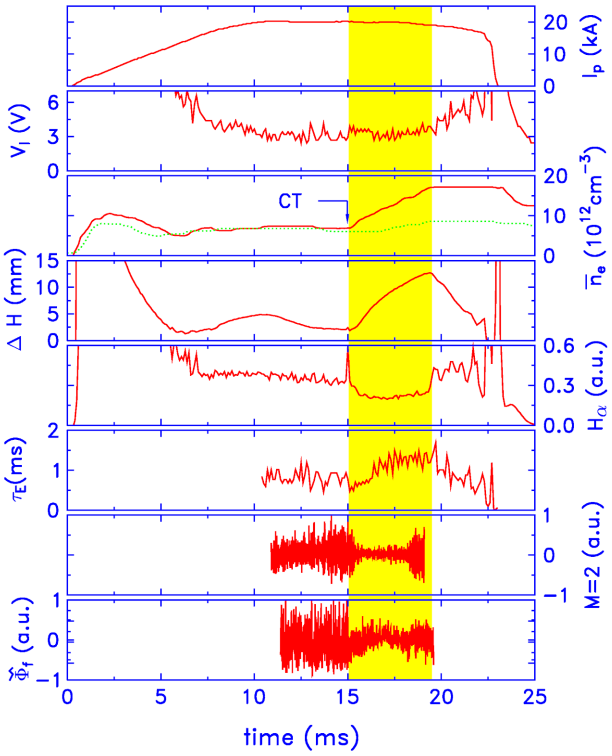

Figure 2.7: Effect of CT on STOR-M Plasma [39]

2.7 Generation of Dust in Tokamaks

2.7.1 Basics

Plasma confinement is not perfect in reality, enabling us to extract thermal energy from the wall of a fusion reactor. Naturally, unconfined particles from the plasma interact with the reactor wall, sending various shapes and sizes (on the order of μm to nm) of material from the wall into the plasma. These small impurity particles are termed, dust. Dust particles within the plasma typically acquire various amounts of negative charge, though may become heavily positively charged when heated, due to high levels of thermionic electron emission [44]. These charged particles may then start to exhibit motion which is heavily influenced by their interaction with the initial plasma. This leads to the generation of a new type of plasma, termed a Dusty Plasma.

In the case of reactors like ITER, high energy neutrons produced by the plasma are intended to strike the tungsten divertor plates. High thermal stress on these divertor plates will lead to increased material sputtering, potentially resulting in significant tungsten (W)

dust generation [45, 46]. Mitigating the negative effects of tungsten dust is therefore of crucial importance for producing fusion energy. In order to do this, we must understand how W dust behaves in a tokamak.

2.7.2 Effects of Tungsten Dust on Tokamak Plasma

Dust tends to be detrimental to a fusion plasma, and should be considered as a plasma pollutant. Fortunately, dust particles are often sufficiently slow in tokamak plasmas, such that bremsstrahlung losses are generally not of primary concern. Rather, this dust is generally harmful due to the fact that it can alter plasma dynamics and absorb much needed tritium [47]. In addition to this, dust particles can be highly mobile within the fusion plasma.

During the liberation of a dust grain from it's parent material, it may be quickly heated and evaporate into the plasma as an ionized impurity particle. Dust Particles which are not evaporated entirely are accompanied by a shielding layer of ablation material. This shielding allows the particle to penetrate further into the fusion plasma [48]. Sufficiently large particles may be able to penetrate into the reactor core, where contamination effects are especially disruptive. Core W dust is incredibly harmful as it can absorb great amounts of tritium from where it is needed most. This dust also tends to leach energy away from the plasma via electron excitation/ radiation. Excessive core dust can be lethal to a fusion reactor. In particular, core tungsten injection rates on the order of mg/s are enough to potentially destabilize the fusion plasma [48]. Finally, excessive amounts of W dust represents a safety hazard. Large quantities of W dust and hydrogen, reacting with air in an ITER like reactor may cause an explosion capable of breaching the system. [49].

Chapter 3

Impurities in a Fusion Plasma

3.1 Introduction

When considering a fusion reactor, impurities in the plasma may be generally defined as any substances which find themselves inside the confined plasma, not participating in fusion energy generation and/or sustaining the bulk plasma. Some impurities may be useful to a fusion reactor, for purposes such as thermal load control and/or plasma stabilization. For example, impurity seeding is utilized to radiatively cool the plasma near the divertor region, in order to prevent the divertor from melting [50]. This is done via injection of various impurity gases such as N, Ne and Ar into the divertor region. Used intelligently, impurities may be key to sustaining a fusion reaction. However, most impurities are found to be metal compounds from atomic to μm sizes which originate from the plasma facing wall [51, 52]. These impurities generally have detrimental effects on the plasma, scaling with the quantity found inside the machine. In particular, core plasma cooling via bremsstrahlung radiation must be reduced. As such, the spatial distribution of impurities within the reactor is crucial. Impurities found in the bulk plasma, where the majority of fusion reactions occur are generally more harmful to plasma sustainment and quality.

In the effort to reduce impurity content in the bulk plasma of the tokamak reactor, the divertor configuration was invented. Here, neutral particles liberated from the wall would be ionized before migrating past the separatrix and directed via the poloidal magnetic

field in the scrape-off layer, towards the divertor plates. Upon striking the divertor plates, impurities may be neutralized and subsequently pumped from the edge of the divertor region. In modern tokamaks with the divertor configuration, impurities are directed with this scheme, though impurity particles are still able to migrate from the wall and divertor plates, into the bulk plasma. This is effectively due to the fact that particles in the scrape-off layer (SOL) may posses enough energy to overcome ion friction, holding them in this region [50]. This could be due to a variety of reasons, such as sputtering from the wall with a large amount of energy, or particles gaining energy through some event in the SOL. Neutral particles crossing the separatrix before ionization may also contribute to bulk plasma contamination. Once the particle passes the separatrix, it may then migrate towards the plasma core, through a variety of mechanisms [53].

3.2 Impurities Resulting from the Tungsten Divertor

The tokamak divertor will experience the most extreme thermal loading of any part of the reactor. In fact, special control over heat flux impinging on the divertor is required for operation in ITER, despite the use of an advanced, actively cooled tungsten divertor, rated for 10 MW/m^2 incident power flux density [54]. Heat flux control measures such as distancing the plasma wall contact and x-point geometry are used to better distribute the thermal load over the surface of the divertor. Additionally, the particle flux may be reduced on the divertor by increasing the local pressure, resulting in a decrease in the flux linkage to the plates [55]. This is accomplished via the previously mentioned mechanism of impurity seeding 3.1. While in this state, the divertor is said to be partially detached.

Though a tungsten divertor may be maintained at tolerable operating temperatures, the effects a massive heat load on the divertor remain a problem for plasma purity. Different particles entering the divertor region interact with tungsten in unique ways. Neutrons radiated from the plasma tend to cause embrittlement of the surface, worsening the damage from other sources [56]. Hydrogen (unused tritium and deuterium fuel) creates surface blisters which warp the surface and may burst (Figure 3.1). Helium generated as a byproduct of the deuterium-tritium reaction, causes etching in the surface of tungsten,

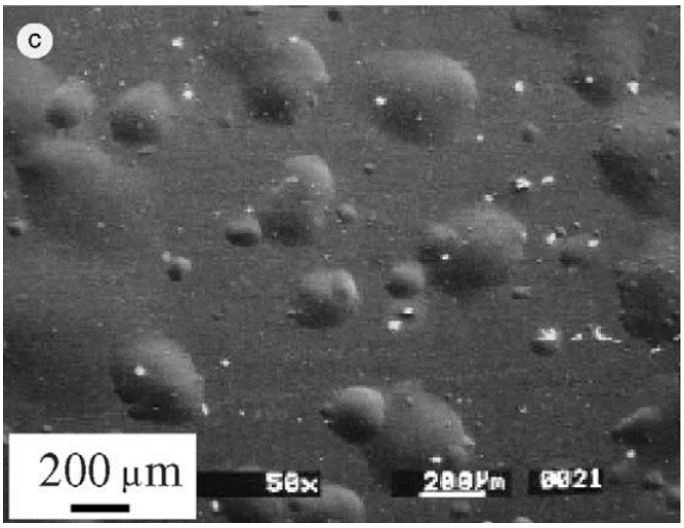

Figure 3.1: Hydrogen Blistering on the Surface of Tungsten [23]

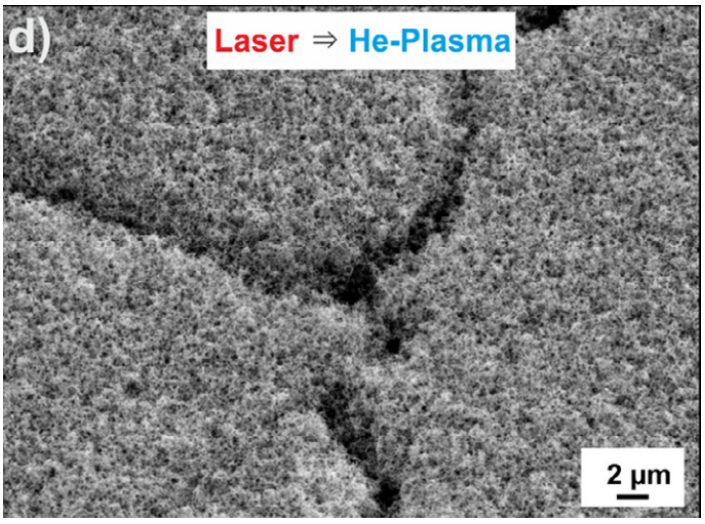

Figure 3.2: Fuzz Growth on the Surface of Tungsten [25]

leaving behind thin, tall vertical structures known as fuzz (Figure 3.2). This fuzz is mechanically weak, and is easily liberated from the surface. All previously mentioned effects aid in the liberation of particles from the tungsten surface. Most troublesome are those which do not entirely evaporate when passing the separatrix, resulting in large dust particles in the plasma. Dust is massive compared to atomic scale impurities, thus, even small amounts contribute greatly to reducing overall plasma quality.

3.3 Dusty Plasma Dynamics

3.3.1 Basics

A Dusty plasma contains impurities on the approximate order of μm's and smaller, which can play a significant, though not dominant role in plasma dynamics. In this thesis, we limit our consideration of dusty plasmas to those with a low number density of dust particles. All impurities within such dusty plasma, are spaced on a length scale greater than their associated Debye sphere diameters. This eliminates collective behaviour of the impurities within the plasma. However, the motion of impurities may still be strongly influenced by the plasma. Through various interactions with the surrounding plasma, dust particles can acquire a large negative or positive charge [44]. The motion of dust particles within a plasma are governed by multiple forces, many of which are influenced by dust charge and charging effects. Figure 3.3 illustrates the motion of such dust particles within a tokamak.

3.3.2 Charging Mechanism

Dust charges in a tokamak plasma due to several primary mechanism, including [44, 58]:

1. Plasma ion and electron interaction.
2. Secondary electron emission.
3. Thermionic emission.
4. Dust particle vaporization.
5. Radiation.

Figure 3.4 illustrates the processes involved in dust particles charging. A useful way of looking at dust particles in a plasma, is to treat them like any other conductor placed within a plasma, essentially as a floating Langmuir probe. Additionally, we need to consider all currents which will be collected at the dust grain surface. These currents are generated via the aforementioned dust charging mechanisms. The steady state charge on

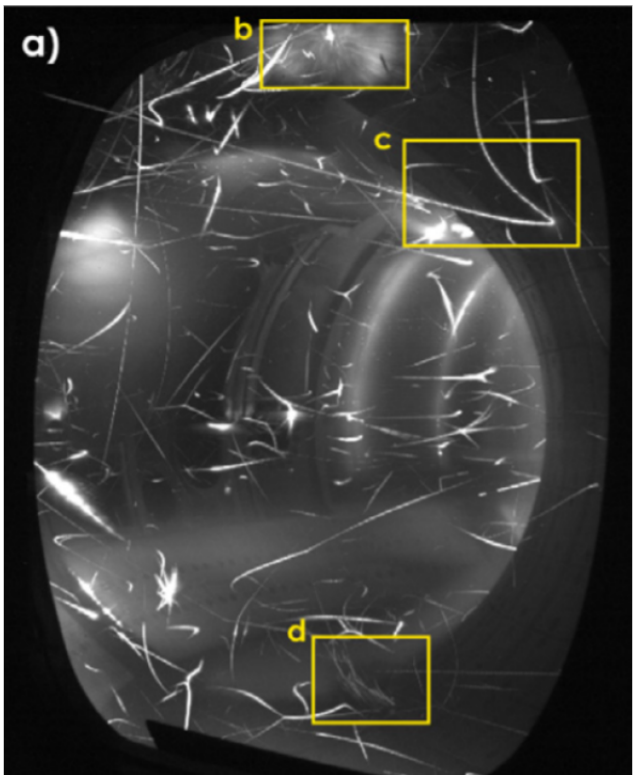

Figure 3.3: Dust Particle Trajectories in TEXTOR (Tokamak Experiment for Technology Oriented Research) [57]. a) Complex motion of pre-characterized carbon and tungsten dust is observed in a plasma discharge from 50 to 400 ms. Dust particles are found to b) disintegrate upon collision with the walls, c) reflect off the chamber wall and d) seems to actively migrate past the scrape-off layer, back into the main plasma.

a dust particle is found by solving for the surface potential of the dust grain (ϕ_s) in the equilibrium current condition [59]:

$$I_e + I_i + \sum_Z I_Z + I_{th} + I_{see} = 0. \tag{3.1}$$

Here, I_e and I_i are respectively the plasma electron and ion currents, I_z represents impurity ion current of various charge states (Z), I_{th} and I_{see} are respectively thermionic emission and secondary electron emission currents from the dust grain. ϕ_s appears implicitly within these current terms. Once ϕ_s is determined, the dust charge (Q_d) may be simply calculated, treating the dust grain as a spherical capacitor:

$$Q_d = 4\pi\epsilon_0 r_d \phi_s, \tag{3.2}$$

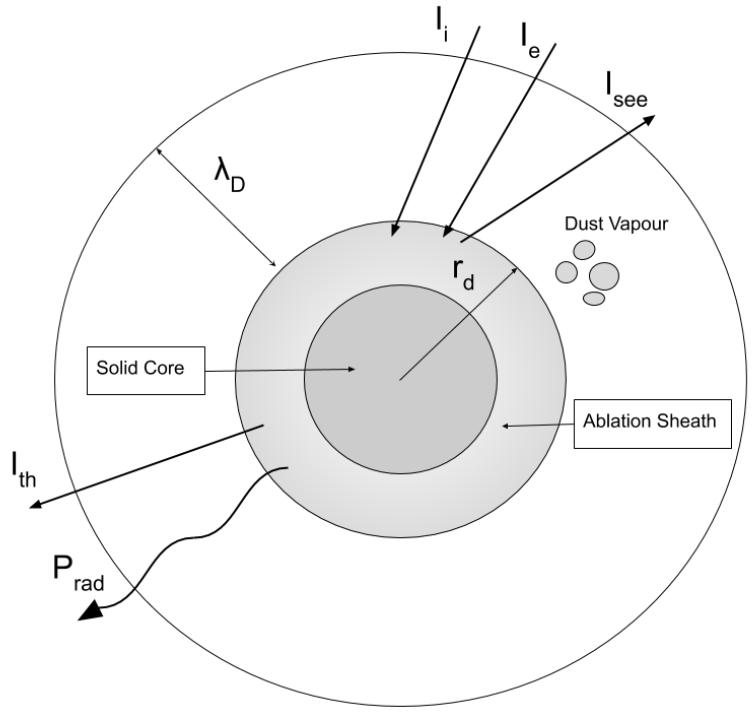

Figure 3.4: Dust Grain in a Plasma. Electron and ion currents (I_e and I_i, respectively) are collected on the dust particle surface. In a hot fusion plasma, this surface is generally an ablated cloud of material (ablation sheath), which evaporates due to heating. Additionally, a secondary plasma containing a significant amount of dust ions, may form around the sheath region, indicated by λ_D [58]. A secondary electron current (I_{see}) is produced by interactions of incident particles on the dust grain surface. Heating of the dust grain results in radiated power (P_{rad}) and the generation of a thermionic emission current (I_{th}).

where, ϵ_0 is the electric permittivity of free space and r_d is the dust grain radius.

When considering electron and ion currents, basic orbital-motion-limited (OML) theory may be applied for simplicity. Here, the assumption of Maxwellian ion and electron velocity distributions are made. The standard equations for the floating Langmuir probe result, assuming negatively charged dust grains [60, 61]:

$$I_e = -4\pi e r_d^2 n_{e0} \sqrt{\frac{k_B T_e}{2\pi m_e}} \exp\left(\frac{e\phi_s}{k_B T_e}\right), \tag{3.3}$$

$$I_i = 4\pi Z^2 e r_d^2 n_{i0} \sqrt{\frac{k_B T_i}{2\pi m_i}} \left(1 - \frac{Ze\phi_s}{k_B T_i}\right), \tag{3.4}$$

where, n_{e0} and n_{i0} are respectively the electron and ion densities away from the dust

sheath, k_B is the Boltzmann constant, T_e and T_i are respectively the electron and ion temperatures, m_e and m_i are respectively the electron and ion masses, e is the fundamental charge and Z is the degree of ionization. Equation 3.4 may be additionally utilized to determine the impurity ion currents (I_Z), so long as the corresponding ion parameters are utilized. More accurate modeling of I_Z is given in [59].

Thermionic emission is the process by which electrons are liberated from a sufficiently hot material. In this case, a dust particle heated by the surrounding plasma, ejects electrons from its surface. This results in the following current from the dust surface, based of the Richardson-Dushman equation [62]:

$$I_{th} = 16\pi^2 r_d^4 A_R T_d^2 \exp\left(-\frac{W_f}{k_B T_e}\right). \tag{3.5}$$

Here, $A_R = 1.20173 \times 10^6 Am^{-2}K^{-2}$ is Richardson's constant, T_d is the dust grain temperature and W_f is the work function for the dust material (tungsten in this case). Here the dust is assumed to be negatively charged. As the dust temperature rises, the dust grain may develop a net positive charge due to increased thermionic emission. [59] gives the equation describing I_{th} for a positively charged dust grain.

Secondary electron emission (SEE) is the process whereby electrons are ejected from a material, due to bombardment of particles with sufficiently high kinetic energy. In this case, particles from the plasma impinge on the surface of the dust grain, resulting in SEE. The secondary electron current, originating from the dust grain due to electron and ion bombardment is:

$$I_{see} = \delta_{see} I_e + \gamma_{sei} I_i, \tag{3.6}$$

where,

$$\delta_{see} = (2.72)^2 E_e \left(\frac{\delta_{max}}{E_{max}}\right) \exp\left(-2\Big(\frac{E_e}{E_{max}}\Big)^{1/2}\right). \tag{3.7}$$

Here, δ_{see} is the secondary electron emission coefficient (determined by utilizing the Sternglass approach) [63], E_e is the incident electron kinetic energy, δ_{max} and E_{max} are respectively the maximum SEE coefficient and the energy at which it occurs, γ_{sei} is the secondary electron coefficient due to ion bombardment and I_i is the ion current for that

species. γ_{sei} is given empirically for various charges of hydrogen ions in [64]. In order to better explain the dominant role of SEE in dust charging within a tokamak, the more complex “R-model" may be implemented [65].

As seen within the analysis above, even a simple model of dust charging requires knowledge of plasma parameters, material properties for the dust, dust temperature (T_d) and potential (ϕ_s). Consequently, T_d remains an unsolved variable, in our hopes to determine the net, steady state charge on a dust particle. T_d may be solved utilizing the heat equation, assuming heating to be uniform over the dust grain [66]:

$$m_d(t, T_d)c_s(T_d)\frac{\mathrm{d}T_d}{\mathrm{d}t} = 4\pi r_d^2 \Xi_{net}, \tag{3.8}$$

where, m_d is the mass of the dust particle, c_s is the specific heat capacity of the dust and Ξ_{net} represents the summation of all power fluxes on the dust particle surface. m_d is shown to be an explicit function for t and T_d as evaporation of the dust particle may be considerable. Both m_d and c_s may be modelled as constants for simplicity. Ξ_{net} is determined by many processes, including: radiated power, evaporation and other neutral particle emission, recombination and power fluxes caused by the dust grain current generation mechanisms including: plasma electrons, SEE, etc. [44].

3.3.3 Motion Inside the Tokamak

Dust motion within a tokamak may be quite complex, as it is governed by multiple forces. Additionally, the dust grain itself has some degree of internal structure, which adds further details to the problem. Internal dust grain structure includes a possible ablation sheath (shown in figure 3.4) and asymmetries which may result in additional effects, including: radiated power, various rotations, etc. For the sake of simplicity, assuming the effects due to the internal structure of the dust are small with respect to the translational forces acting on it, the equation of motion for the dust particle becomes:

$$m_d\frac{\mathrm{d}\mathbf{v}_d}{\mathrm{d}t} = \sum_i \mathbf{F}_i. \tag{3.9}$$

Here, m_d is the dust mass, $\mathbf{v}_d$ is the dust particle velocity and $\mathbf{F}_i$ represents the various forces acting on the dust particle [67]. The dominant forces determining the motion of a metallic dust grain in a tokamak include [67, 68]:

1. Electrostatic force
2. Magnetic force
3. $\mathbf{E} \times \mathbf{B}$ forces
4. Lorentz force
5. Force due to gravity
6. Rocket force
7. Drag forces due to ions and neutral particle collisions

Electric forces result in charged dust particle motion influenced by electric fields within the plasma, such as those of the tokamak current drive. Gravitational force on its own, simply causes the particle to fall, while the Lorentz force causes dust particles to rotate around magnetic field lines. The electrostatic force ($\mathbf{F}_E$), gravitational force ($\mathbf{F}_g$) and Lorentz force ($\mathbf{F}_L$) on the particle are respectively:

$$\mathbf{F}_E = -Q_d \mathbf{E}, \tag{3.10}$$

$$\mathbf{F}_g = m_d \mathbf{g}, \tag{3.11}$$

$$\mathbf{F}_L = Q_d \mathbf{v}_d \times \mathbf{B}. \tag{3.12}$$

Here, Q_d is the dust charge, $\mathbf{E}$ is the electric field, $\mathbf{g}$ is the acceleration due to gravity, $\mathbf{v}_d$ is the dust particle velocity and $\mathbf{B}$ is the magnetic field. The effect of magnetic forces on a dust particle (included in [67]) may be significant on a ferromagnetic grain. For Tungsten

divertor dust, this force is not present. Additionally, the induced magnetic moment for a spherical, rotating, charged dust grain is [69]:

$$\boldsymbol{\mu} = -\left(1+\eta_d\right)\frac{Q_d r_d^2}{2c}\boldsymbol{\Omega}, \tag{3.13}$$

where, η_d is a coefficient which characterizes the charge distribution within the grain, $\boldsymbol{\Omega}$ is the angular velocity of the grain and c is the speed of light. The presence of a dust grain magnetic moment would cause it to align it's $\boldsymbol{\mu}$ axis with $\mathbf{B}$ within the plasma.

The rocket force on a dust particle is due to uneven evaporation from the grain surface. This would result in thrust being produced by the dust grain, allowing it to maneuver in various ways, dependant on the evaporated flux from the grain. This may be represented as [67]:

$$F_{roc} = \xi m_\nu v_\nu \Gamma_\nu, \tag{3.14}$$

where ξ is the evaporation symmetry factor, m_ν and v_ν are respectively the mass and speed of evaporated particles and Γ_ν is the evaporation flux. The rocket force represented in this form is very general, including the flux of particles evaporated from the surface by various methods, including various forms of thermophoresis.

The friction force on dust particles due to various species within the plasma ($\mathbf{F}_{fric}$) may be analysed at the kinetic level, utilizing the following equation [70, 71]:

$$\mathbf{F}_{fric} = m_\alpha \int \left(\sigma_c(v) + \sigma_s(v)\right)\mathbf{v} v f_\alpha(\mathbf{v}) \mathrm{d}^3 v, \tag{3.15}$$

where, m_α is the mass of the species, $\sigma_c(v)$ and $\sigma_s(v)$ are respectively, the momentum-transfer cross sections due to collection by and scattering off of the dust particle, v and $\mathbf{v}$ are respectively the speed and velocity of the species and $f_\alpha(\mathbf{v})$ is the velocity distribution function of the species. Once $f_\alpha(\mathbf{v})$ is determined, the complexity in calculating $\mathbf{F}_{fric}$ resides in determining the momentum-transfer cross sections. There are however, other methods which simplify the calculation of friction forces acting upon dust in the plasma. MHD theory may be applied, resulting in the following equation for ion drag ($\mathbf{F}_{id}$) [68,

70]:

$$\mathbf{F}_{id} = \eta\pi r_d^2 n_i m_i v_{ith} \left(\mathbf{u}_i - \mathbf{v}_d\right), \tag{3.16}$$

where, η is a constant dependant on dust size and difference between electron and ion temperatures, n_i is the ion number density, m_i is the ion mass, v_{ith} is the ion thermal velocity and $\mathbf{u}_i$ is the ion fluid velocity. The ion drag force results in dust particle motion influenced by the fluid velocity of plasma ions.

A tokamak is designed for the confinement of a fully ionized plasma. As such, interactions in the bulk will be coulomb dominated due to the high density of ions compared to neutral particles [72]. Despite this, neutral particles in a tokamak are still present. Neutral interactions near the tokamak edge region become more significant as the density of neutral particles increases further from the core plasma [73]. As a result, dust neutral drag may be significant in the plasma edge region. The dust neutral drag may also be determined in a general fashion as follows [68, 70]:

$$\mathbf{F}_{nd} = m_d \nu_{nd} \left(\mathbf{u}_n - \mathbf{v}_d\right), \tag{3.17}$$

where, ν_{nd} is the dust-neutral collision frequency and $\mathbf{u}_n$ is the neutral fluid velocity. Similar to the ion drag force, the neutral drag force results in dust particle motion influenced by the fluid velocity of neutral particles. In the case of slow moving dust particles relative to the neutral thermal velocity, $\mathbf{F}_{nd}$ simplifies to the Epstein drag force [74]:

$$\mathbf{F}_{Epst} = \frac{4\pi}{3} \delta_{Epst} r_d^2 n_n m_n \sqrt{\frac{8 k_B T_n}{\pi m_n}} \left(\mathbf{u}_n - \mathbf{v}_d\right) \tag{3.18}$$

where, δ_{Epst} is the Epstein drag coefficient, n_n, m_n, T_n are respectively the neutral number density, mass and temperature.

Chapter 4

Equipment

4.1 Compact Torus Injector

4.1.1 Basics

The USCTI (Figure 4.1) is the device utilized to form and subsequently accelerate a CT. It is essentially a coaxial rail gun, where the projectile is a plasmoid, instead of a solid object. The gun is aimed tangentially into the STOR-M plasma in the toroidal direction. The STOR-M plasma serves as the target for the incident CT.

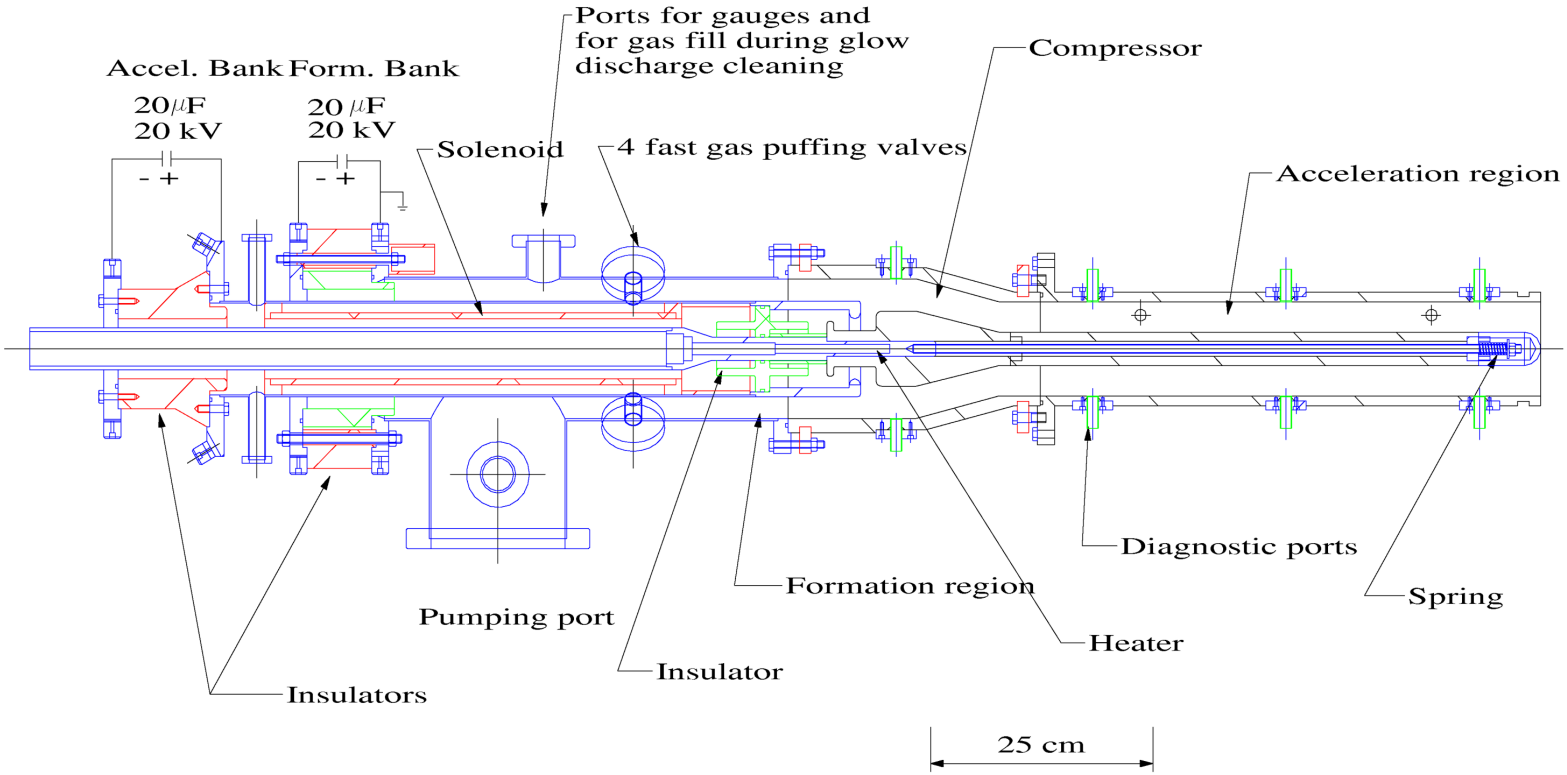

Figure 4.1: University of Saskatchewan Compact Torus Injector (USCTI) Schematic. Reprinted from the University of Saskatchewan Department of Plasma Physics archive.

4.1.2 Formation

The CT formation process requires multiple high voltage banks and precise timing. Figure 4.2 illustrates a cross section of this process. The first stage involves engagement of the solenoid bank. This develops a quasi static solenoid field (i). Secondly, the gas puffing bank is engaged, allowing hydrogen fuel to enter the chamber (ii). The switch for the formation bank is then closed, creating a current through the plasma which results in a large return current (iii). This return current sets up a magnetic field in the azimuthal direction. Interaction of this azimuthal field with the radial current through the plasma creates a Lorentz force, which accelerates the plasma to the right, analogously to the bar and rail problem. The plasma is pushed against the solenoid flux until it fully reconnects unto itself and separates from the solenoid field (iv). The plasma is thus, forced into the acceleration region of the CTI.

4.1.3 Acceleration

When the CT enters the acceleration region, the acceleration bank is engaged. A current flows through the CT as a short, in a similar manner to Figure 4.2 (iii). However, in this case the radial current interacts with the azimuthal field of the CT to produce a net Lorentz force on the CT to the right. Since the completely formed CT is a self contained magnetic structure, it remains intact through this process. In this manner, the CT can reach muzzle velocities up to 210 km/s.

4.1.4 Magnetic Probes

In order to determine the the velocity of the CT, simply wound coils functioning as magnetic probes are located at three evenly spaced locations along the acceleration region of the CTI. The delay in the peak of the magnetic field waveform, between magnetic probes at various fixed distances along the CTI barrel is utilized to determine the motion of the CT. The voltage signal of the magnetic probes is determined from a passive RC

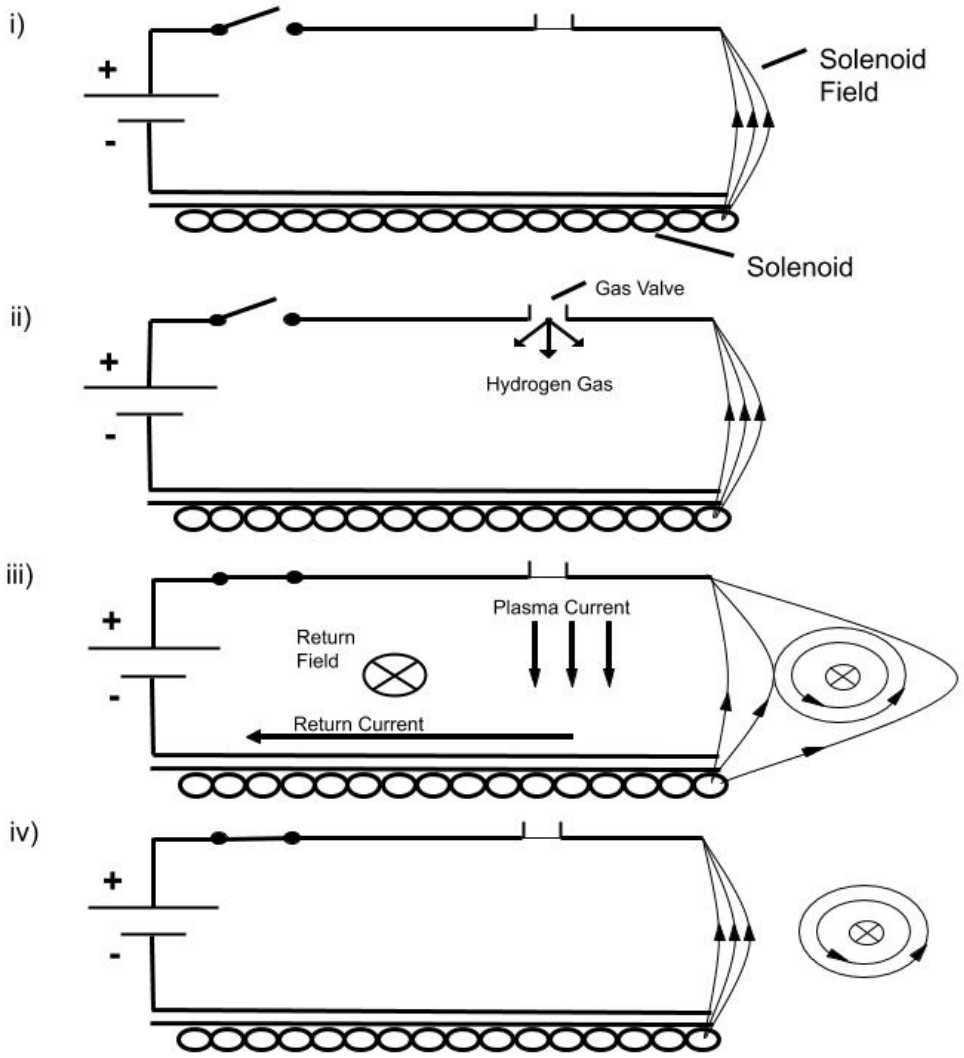

Figure 4.2: CT Formation Process

integrator. The integrated output signal is as follows:

$$V_{int} = -\frac{NA_{coil}B}{RC}, \tag{4.1}$$

where N is the number of turns of the magnetic probe coil, A_{coil} is the area of the coil, B is the magnetic field magnitude, R and C are respectively the integrator resistance and capacitance.

4.1.5 Repetitive Firing

Thus far, the USCTI has not achieved the capability to fire more than one CT into the same tokamak discharge. A maximum fire rate of 10 Hz for 3 discharges has currently been achieved [75]. A. Pant in his 2009 M.Sc. thesis [76] outlines multiple changes that were made to the system in order to facilitate repetitive firing. These changes include faster charging high current power supplies for the formation and acceleration banks, faster switches and improved gas valve insulation. In addition to these changes, the resistance of the current limiting resistor from the new power supplies was decreased. In order to further reduce charge time, this resistance will be further decreased in the future. The option of repetitive CT injection, further enables the possibility of new experiments involving dust injection in STOR-M. Modifications to the repetitive firing mode of the CT remain ongoing.

4.2 Dust Injector

Reactors operating under fusion conditions will produce dust naturally, through various plasma wall interactions. In order to simulate this in STOR-M, we require an artificial source of dust. Dispersing this dust within the reactor for a controlled experiment requires a dust injector. The dust injector has the following constraints to its design:

- Requires adjustable electrical input which can be triggered remotely.
- Must respond consistently under the same initial input for appropriate dust placement. Injector timing may be offset if necessary. Timing precision on the order of at least milliseconds allows for accuracy in positioning injected dust on the order of millimeters.
- Must be leak tight for use in ultra high vacuum. CF-40 flange connection is required.

The CT fast gas valve was chosen as the frame for the dust injector, as it already meets these requirements when operating with hydrogen gas. Furthermore, this design will allow for the dust injector to operate independently, while being implemented in a variety

of experiments concerning tokamak and CT operation. The current gas valve design is nevertheless unable to inject solid material. However, the gas camber within the gas valve has enough room to allow modifications to the piston, which enables gas output (discussed in detail in Chapter 4.2.3). Proper modification will allow the piston to also disperse solid material at the injector outlet. Essentially, the only distinction between the gas valve and the dust injector will be the choice of piston. The gas valve may be converted between a standard fast gas valve and a dust injector by simply changing the piston.

4.2.1 Operating Principle of the Injector

The dust injector (Figure 4.6) utilizes an input voltage pulse, in order to generate a high current, capable of moving an inductively coupled conductive piston. This may essentially be represented as a transformer, where the primary (p) moves relative to the secondary (s). A coil positioned below the piston serves as the primary, while the piston serves as the secondary. Figure 4.3 represents this circuit. The initial voltage pulse, powering the activation of the piston, is generated by the discharge of capacitor Cd via the closing of switch s1.

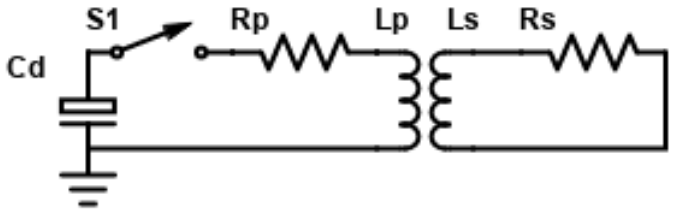

Figure 4.3: Injector Circuit

The coil has both an inductance and a non-negligible resistance which can be calculated. Derivation of realistic inductance formula are actually quite complex, due to the combined interaction of magnetic fields in various wire geometries. The following semi-empirical formula by Wheeler [77], gives a good approximation for the inductance of a round planar coil, wound over most of it's area:

$$L_{coil} \approx 31.33\mu_0 N^2 \frac{r_c^2}{8r_c + 11d}, \tag{4.2}$$

where N is the number of coil turns, r_c is the mean coil radius and d is the diameter of the wire.

The resistance of the entire wire is calculated utilizing concentric wire loops, in order to estimate the total wire length for simplicity. This results in the following formula for the coils resistance :

$$R_{coil} \approx \frac{4\rho N(D_0 + d(N-1))}{d^2} \tag{4.3}$$

where ρ represents the resistivity of the wire and D_0 represents the inner coil diameter.

One should note, that equations 4.2 and 4.3 assume the current to be evenly distributed throughout the wire. The accuracy of this assumption may be quickly checked by comparing the skin depth with the diameter of the coil wire. The skin depth (δ_s) for a good conductor is:

$$\delta_s = \sqrt{\frac{2\rho}{\omega\mu_0}}, \tag{4.4}$$

where ω is the angular frequency of radiation, incident on the conductor. Utilizing the characteristic frequency of the current waveform (Figure 4.4): $f_{char} \approx 2$kHz, the skin depth for copper wire is computed to be approximately 2 mm, which is twice the diameter of the coil wire. Thus, the skin effect will be negligible and our assumptions for equations 4.2 and 4.3 are justified.

Equations 4.2 and 4.3 yield a coil inductance of 35 μH and and resistance of 0.04 Ω. However, these values are not compatible with those obtained from the discharge current of the injector, shown in figure 4.4, when the device was activated. The red line shown in this figure is a linear model of the current waveform, which agrees well with the actual current. The schematic circuit for this waveform is shown in figure 4.5. Here, the transformer has been replaced by an equivalent inductance and resistance. Fitting these parameters to the actual current, we find $L_{eq} = 10$ μH and $R_{eq} = 0.46$ Ω. Apparently, the coil resistance is too low and it's inductance too high to describe the current waveform observed. This is obviously to be expected, as we have not included the impact that the secondary has on these parameters.

Utilizing the fitted parameters, the current waveform is over-damped, with a damping

ratio of 1.82. The over-damped behaviour of this waveform ensures that there is no reverse voltage or ringing across the large polarized capacitors utilized to produce this current. This ensures appropriate and safe operation of the injector power supply.

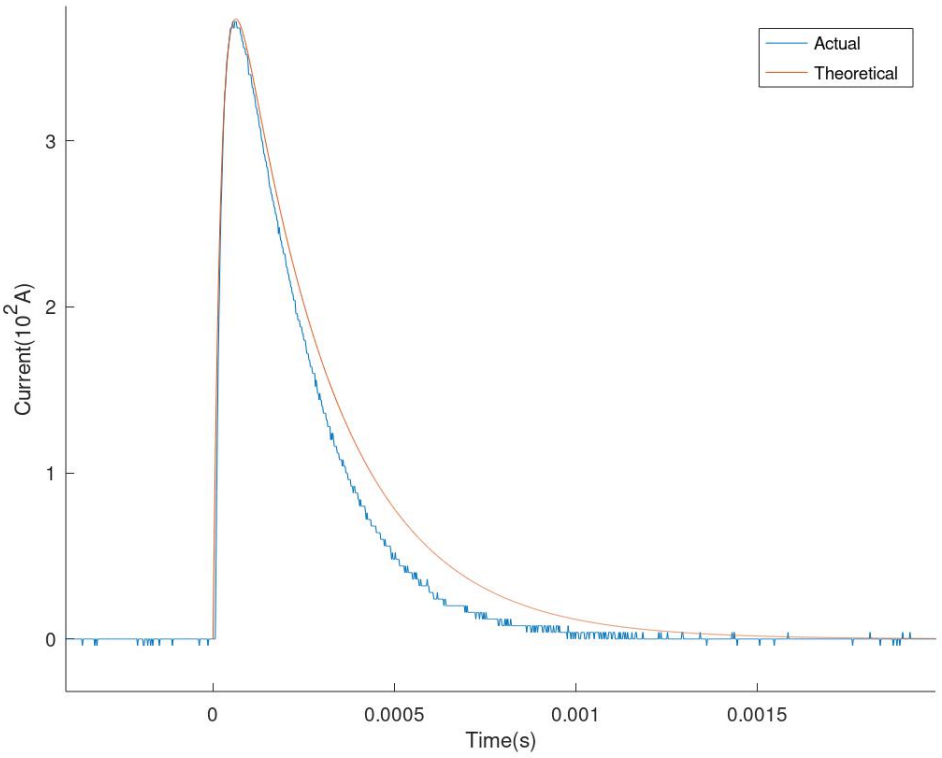

Figure 4.4: Dust Injector Current. Utilizing a linear RLC circuit model, a theoretical best fit for the actual dust injector current is determined. The actual and theoretical curves do not agree perfectly, due to the time dependant mutual inductance in the moving transformer of the dust injector.

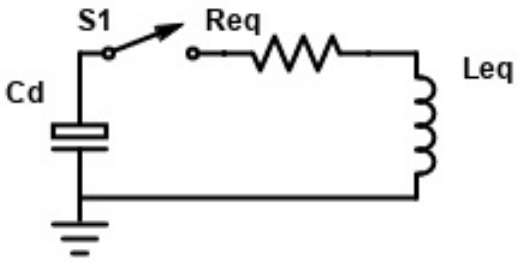

Figure 4.5: Approximate Linear Injector Circuit

The equivalent resistance we see in this circuit will significantly increase when we consider the load of the moving secondary. This may be modelled by the following equation:

$$R_{eq} = R_p + an_{ps}^2 R_s + R_{dyn}. \tag{4.5}$$

Here, n_{ps} is the turns ratio of the primary to the secondary, a is a scaling in the resistance, in order to account for imperfect flux linkage and R_{dyn} represents the effective resistance introduced to the system as a consequence of the moving secondary. The equivalent inductance we see should actually decrease, as movement of the secondary results from opposing the flux of primary. This may be modelled by the following equation:

$$L_{eq} = L_p + L_s - 2C\sqrt{L_p L_s}, \tag{4.6}$$

where C is a number between 0 and 1, representing how well coupled the flux of the primary and secondary are. 1 represents perfect coupling, 0 represents no flux linkage between primary and secondary.

4.2.2 Fast Gas Valve Components

The USCTI gas valve serves as the frame for the the new dust injector. Figure 4.6 shows a cross sectional schematic of the gas valve. The device consists of multiple components, given in Table 4.1.

Table 4.1: Dust Injector Schematic (Figure 4.6) Item Numbers

1	Securing Screw	15	Left Gas Port
2	Spring Adjustment Knob	16	None
3	Spring Adjustment Screw	17	Piston Through Holes
4	Securing Nut	18	Piston Seal
5	Insulated Mount Point	19	Outer Gasket
6	Top Housing	20	Inner Gasket
7	Electric Control Terminals	21	Piston
8	Top Screw Points	22	Inductive Coil
9	Middle Housing	23	Bottom Screw Points
10	Center Shaft Seal	24	Bottom Housing
11	Alignment Ball Bearing	25	Injector Outlet
12	Spring Plunger	26	Bottom Housing Seal
13	Restoring Spring	27	CF Flange
14	Right Gas Port	28	Flange Through Holes

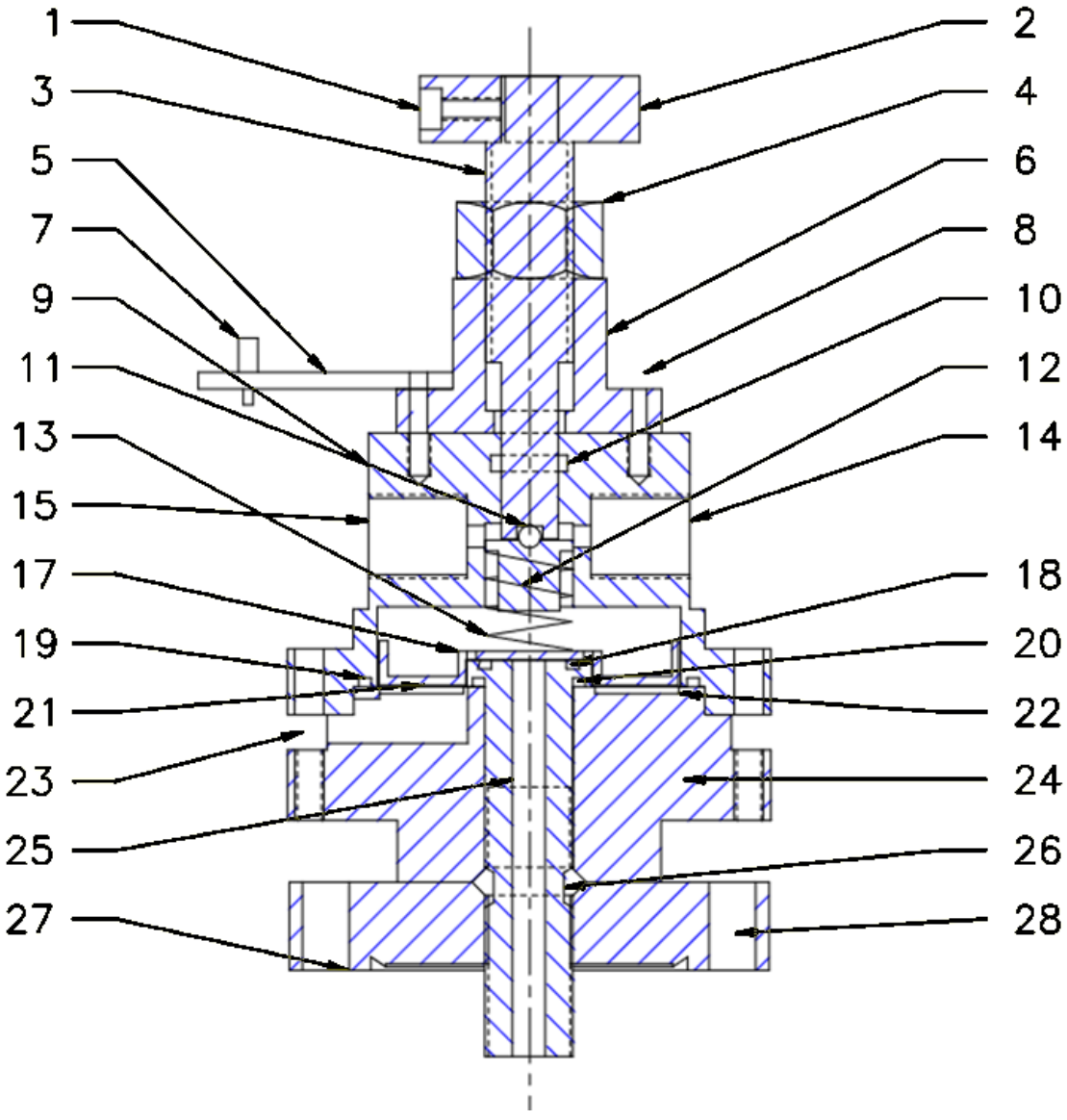

Figure 4.6: Fast Gas Valve/ Dust Injector Body Schematic

From Table 4.1, (1) secures the knob to the adjustment screw. (2) and (3) are respectively the spring adjustment knob and screw. Rotating the adjustment knob enables the compression to be set on the restoring spring (13). Turning the adjustment knob right, drives the adjustment screw down, and compresses the spring. Turning the adjustment knob left reduces compression on the spring. (4) secures the adjustment knob to the top housing (6). The top housing is not vacuum tight. It is required to support the adjustment screw and the insulated mount point (5), where the power supply leads are connected to (7). (8) is required to connect the top portion of the housing, to the middle housing (9).

The central shaft in the middle housing is kept isolated from the top housing and vacuum tight via (10). Located below the adjustment screw is the spring plunger (12), which secures the restoring spring in place against the set screw. In order to avoid misalignment issues with the plunger and the spring, a ball bearing (11) is utilized.

In order for gas feed to be connected to the injector, a right and left gas port are present (13)(14). These gas ports are connected through the central shaft, and lead to the main gas chamber. The piston (21) is located at the base of this chamber .The main gas chamber is kept vacuum tight through the use of multiple gaskets (19)(20). These gaskets are inserted at the interface between the middle and bottom housings.

When power is not applied to the device, the piston is sealed against a gasket at the top of the lower housing via (18). Only when power is applied to the inductive coil below the piston (22) is the piston pushed upward and the seal broken. Through holes in the piston (17) fill with gas from the chamber. This gas is then readily able to enter the injector outlet (25) when the piston seal is broken.

The bottom housing (24) is connected to the middle housing via (23), and the connection made vacuum tight with (26). The bottom housing serves as a connection point for a CF flange (27) to allow connection via (28) to a vacuum system.

4.2.3 Dust Injector Piston

The current fast gas valve for the USCTI has all the necessary components for a working dust injector. However, the design lacks the ability to deposit solid material. For this

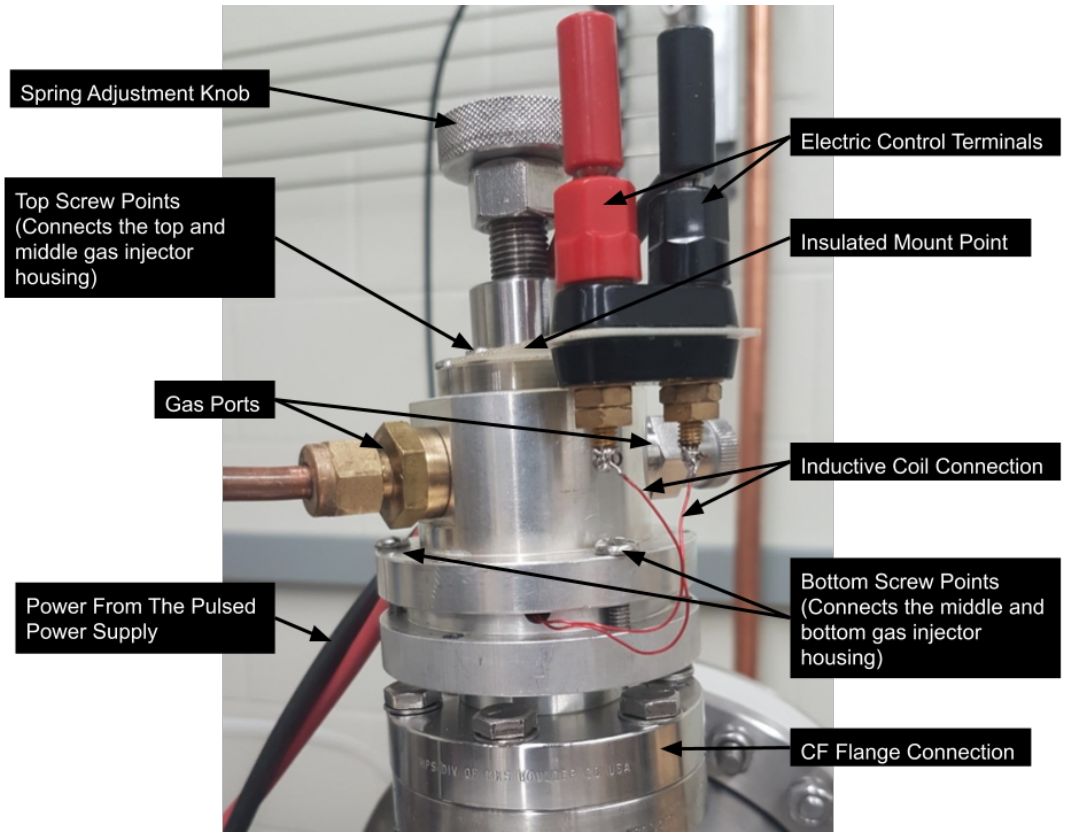

Figure 4.7: Dust Injector

reason, a new piston has been designed and machined for the CT gas valve. The CAD schematic for the piston is shown in Figures 4.8 and 4.9. The length scale values of the piston are given in inches.

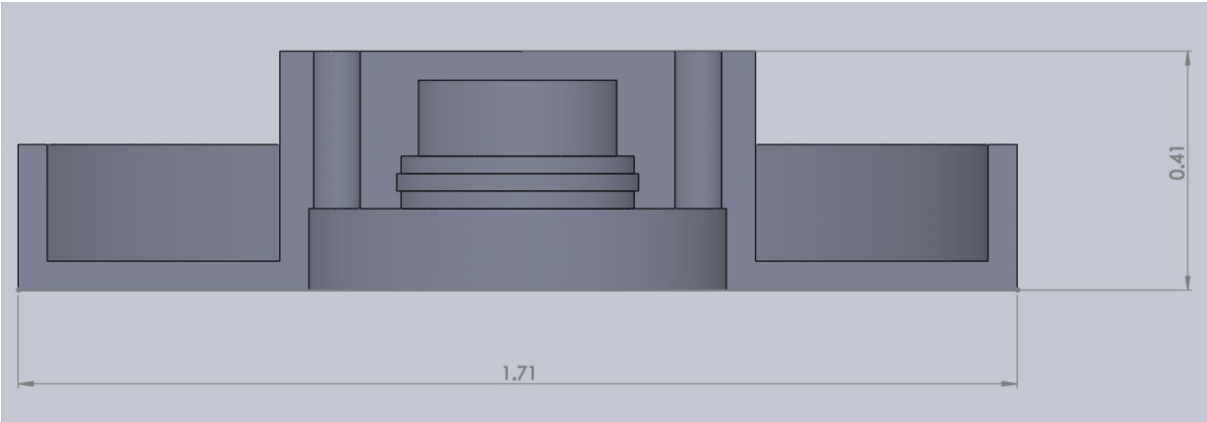

Figure 4.8: Dust Injector Piston (Front View) [78]

In order for the dust injector to inject solid material, a chamber for this material is required. This chamber is located at the top center of the dust injector piston (see figure

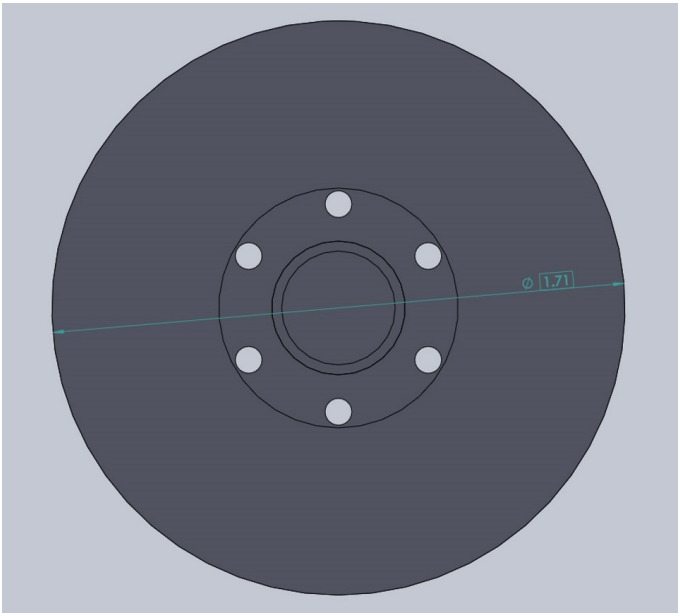

Figure 4.9: Images/Dust Injector Piston (Bottom View) [78]

4.8). Beneath this chamber there are located three concentric ring grooves. A screen is to be positioned within the top ring, in order to ensure particles cannot fall while the piston is stationary. A rubber o-ring is then secured within the second piston ring, in order to keep the screen secured in position. The third, bottom concentric piston ring is then required to secure the rubber o-ring.

Depending on the particle size which is intended for injection, various screens may be used. For this reason, screens must be able to be swapped with minimal difficulty. Also, as screens must be custom made for the injector, screens should be reusable and removal should not destroy the screen. The bottom concentric piston ring is thus, sized so that the screen may be easily swapped and yet, hold the retaining o-ring in place.

In order for the piston to inject gas, six through holes are located concentrically around the solid particle chamber. The bottom concentric piston ring and through holes are spaced so that the piston seal (which prevents gas flow when the piston is in its rest position) seats properly against the bottom of the piston.

Finally, The dust injector piston has a thin base, which revolves around the outer portion of the piston. This provides a large surface area for eddy currents to form, and drive the motion of the piston in the dust injector column. This driving mechanism is able

to break the piston seal, and allow gas injection. Additionally, two small ball bearings are contained within the upper piston chamber. As the piston moves, these ball bearings perturb the micro particles in the chamber and allow some of them to pass through the screen.

4.2.4 Screens

The piston screen serves to limit the size and amount of particles which may be injected by the dust injector. Screen sizes of 5, 10, 14 and 20 μm's have been made for use with the dust injector piston. Choice of screen size here is not arbitrary. Dust sizes on the order of 10 - 100 μm's are anticipated to be produced in large scale, energy producing tokamaks such as ITER [79]. As a particular example, the ASDEX Upgrade (AUG) has characterized the size of tungsten dust produced within the reactor. This is especially relevant due to the fact that AUG operates with full Tungsten PFC's. The dust collection experiment found some particles with 100 μm sizes, though 55% of the particles collected were under 5 μm in diameter [80]. Thus, the current choice of screens provides the correct order of magnitude for particle size filtering, relevant to tokamak fusion conditions.

Screens are made from stainless steel for strength and corrosion resistance. They are woven in a twill dutch weave pattern as shown in Figure 4.10. Particle sizes less than the screen size may be filtered individually through the screen, while particle sizes less than half of the screen size may result in an avalanche effect. This would result in many small dust particles being liberated at once, due to a small local flow, which overcomes the force of static friction and electrostatic interactions on closely pact particles.

For optimal dust injection control, we wish to avoid any dust avalanche effect. This control is also, necessary due to the fact that tokamak plasmas are very sensitive to core W dust. Core tungsten injection rates on the order of mg/s are enough to destabilize the plasma [48]. For perspective, assuming constant flow rate of 20 μm tungsten dust particles to the STOR-M plasma core, around 400 injected particles is enough to potentially cause disruption during a 35 ms discharge. This number should become even smaller for direct injection of W dust to the STOR-M core.

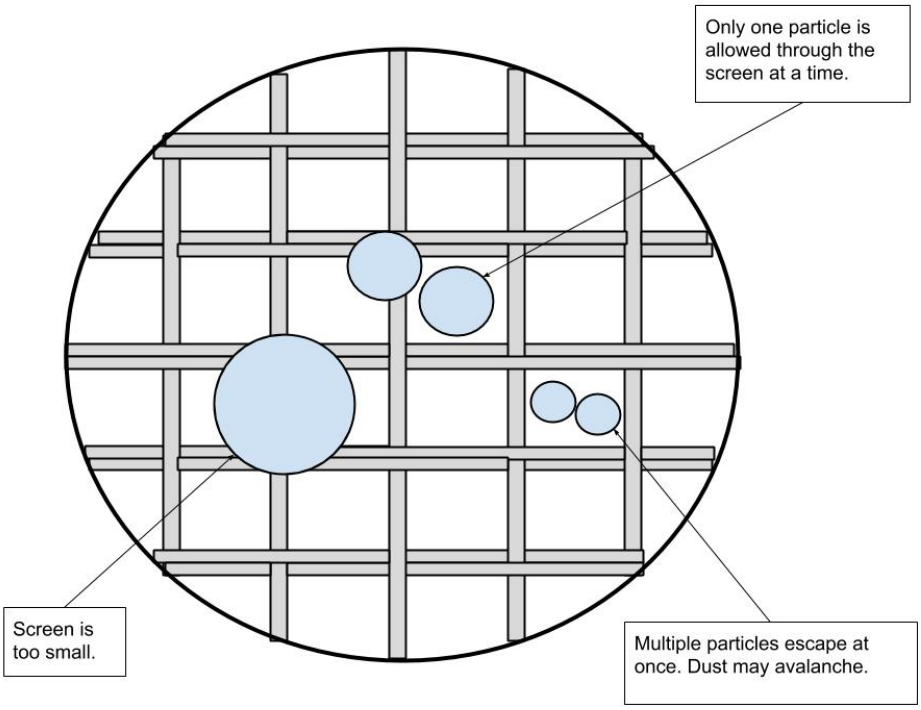

Figure 4.10: Sifting Particles Through the Micro Mesh Screen (Idealized Twill Dutch Weave)

SEM images of the dust injector screens were taken to check the manufacturer specification of the sieve sizes and condition of the mesh. Figure 4.11 shows images of all four screen types. The scale is set at 300 μm, displayed in the bottom right hand corner of the image.

4.3 Pulsed Power Supply

A new modular power supply has been designed to drive the dust injector. The design was based of the USCTI gas puffing fast bank [81]. A full schematic of the device is shown in figure 4.12. Essentially, the pulsed power supply utilizes the P05HA12MT, Acopian adjustable power supply in order to charge capacitor, C1. The silicon controlled rectifier (SCR) may then be triggered, connecting C1 to the banana plug output (OUT) located on the insulated panel. C1 is then directly discharged through the dust injector, when connected to OUT.

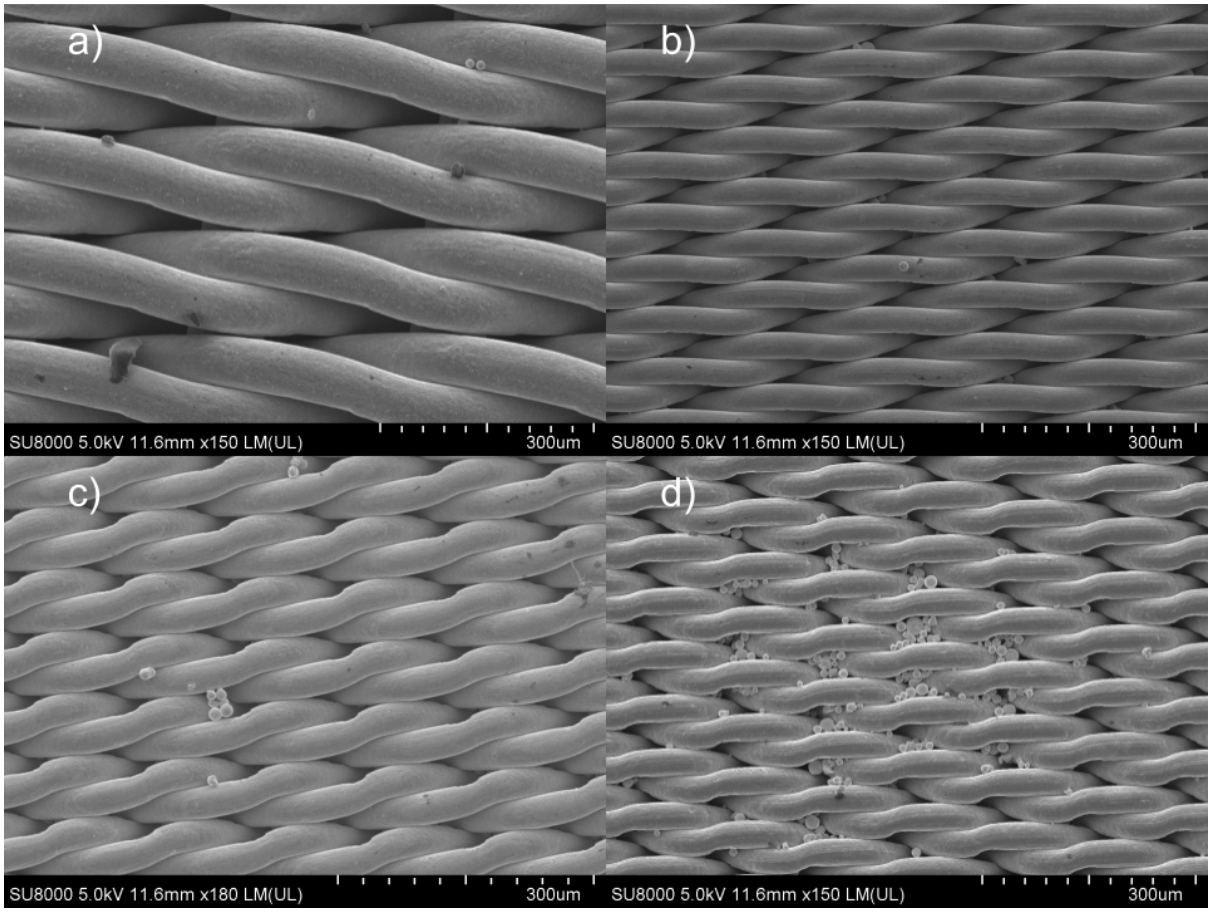

Figure 4.11: SEM Images of the Dust Injector Screens. All screens were imaged after use in the dust injector characterization experiment. In terms of sieve size we have: a) 25 μm, b) 14 μm, c) 10 μm, d) 5 μm. Here, a) has significantly fewer particles which are stuck within the mesh compared to d). This is readily explained by larger sieve sizes allowing particles to clear easier. Both b) and c) show some accumulation of particles, as their sieve sizes are between the extremes of a) and d).

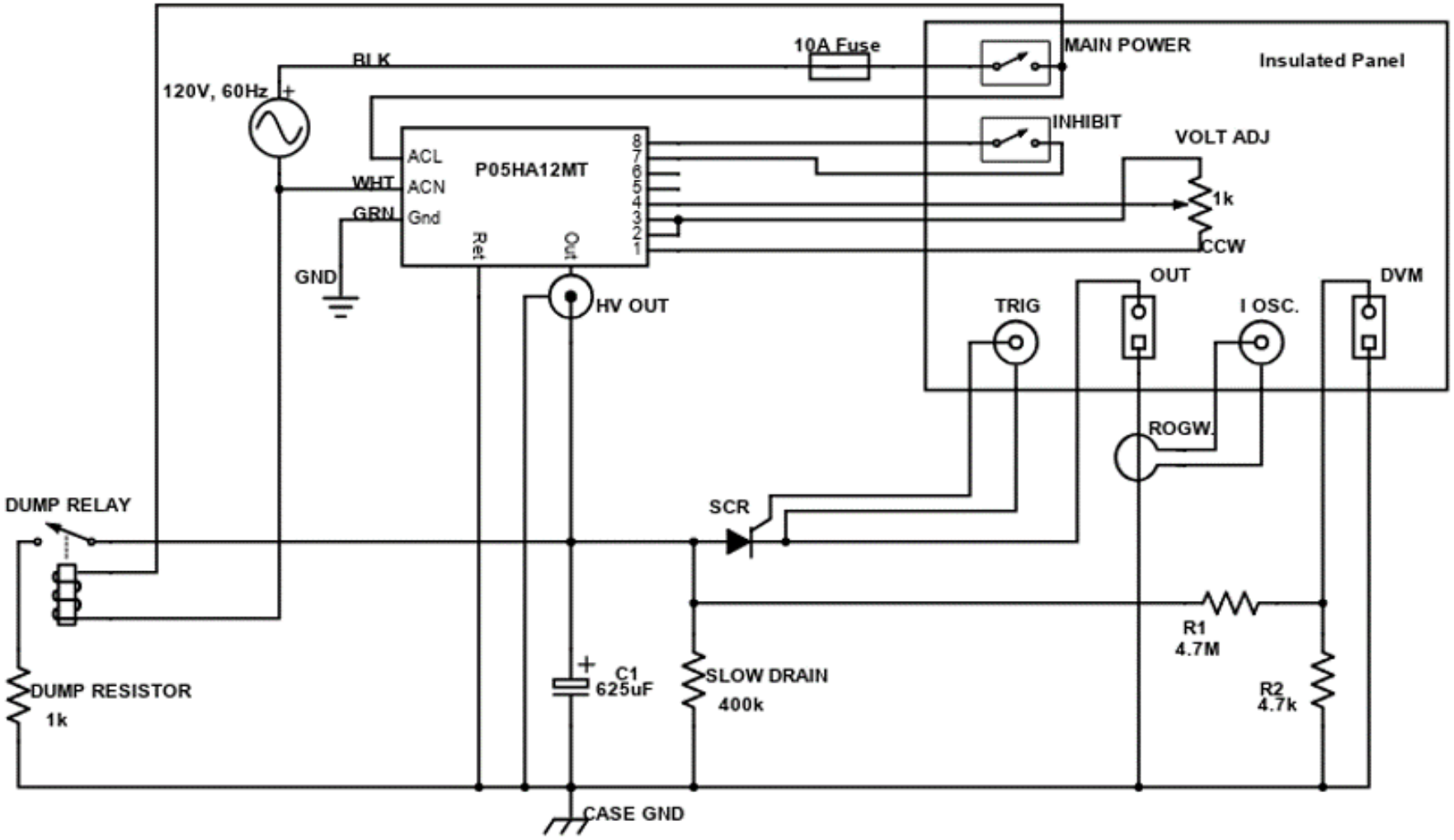

Figure 4.12: Pulsed Power Supply Schematic [82]

The P05HA12MT utilizes 120 V AC input voltage and is grounded through the wall outlet. The output may be set between 0-5 kV DC, with 12 mA max current. A high voltage insulated coaxial cable is utilized to charge C1, from the P05HA12MT output. The voltage of the power supply may then be changed via potentiometer (VOLT ADJ). Additionally, the P05HA12MT also comes equipped with an internal 1 A fuse.

A charge inhibit and main power supply switch are located on the insulated panel. A 10 A Fuse is utilized in series with the main power switch, in case of electrical fault. When the device is turned off via opening the main power switch, the dump relay coil is de-energized, and the dump switch is closed. C1 is then quickly discharged through the 1 kΩ, 200 W dump resistor to case ground.

C1 is composed of four 2500 μf capacitors in series (see Figure 4.13). Each of these capacitors is set in parallel with a 100 kΩ, 20 W drain resistor, which passively dissipate energy when charging is inhibited, primarily for safety. The voltage drop across C1 may be monitored with R1 in parallel with R2, resulting in a 1:1000 voltage monitor, where large resistor values are used to minimize current.

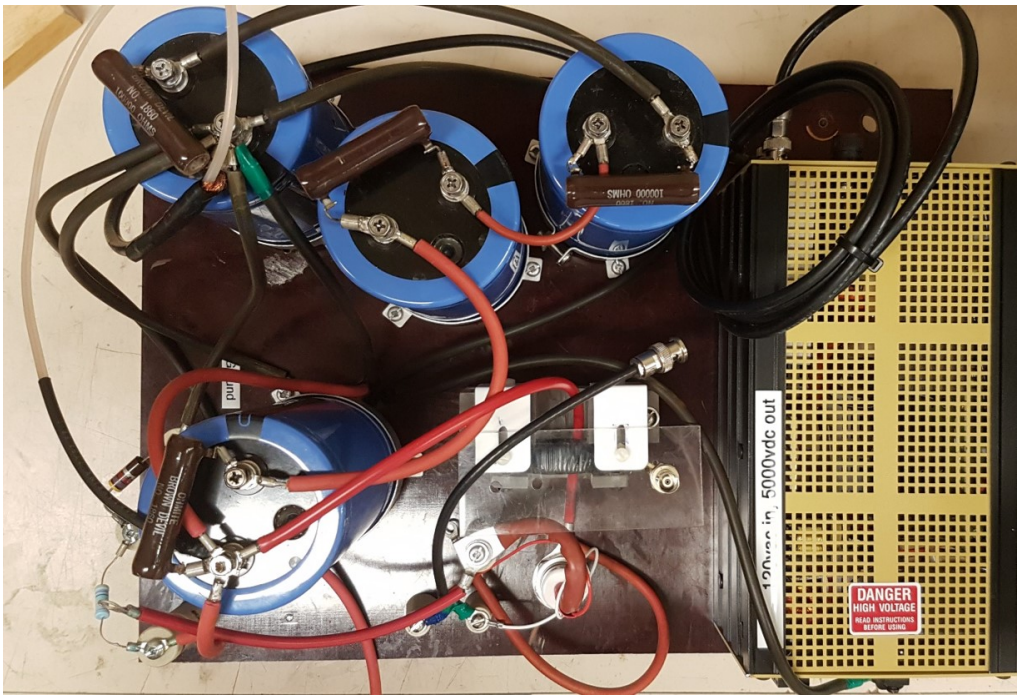

Figure 4.13: Pulsed Power Supply (Internals)

The SCR trigger utilizes a BNC connection (TRIG) located on the insulated panel.

An Approximate 4V trigger pulse is required to forward bias the SCR. In the case that manual triggering is desired, an external fiber optic connection is required as the trigger is floated on top of high voltage from the positive side of C1. Currently, a fiber optic transmitter and receiver pair are utilized for the purposes of triggering the pulsed power supply.

Upon discharging C1, the output current is analysed via Rogowski coil (ROGW.). An oscilloscope may be attached at (I OSC.) in order to determine the current signal. As the Rogowski coil output signal is proportional to dI/dt, a passive integrator is required to determine the current. $\tau = 1.5$ ms was found to be sufficient for the integrator.

Calibration of the Rogowski coil was done utilizing a Pearson probe, with known 100 A/V current measurement. From this, a 12 A/mV, critically damped, calibrated current output was determined for the integrated Rogowski coil output.

The pulsed power supply operates as a closed, modular unit inside of a metal Faraday cage. This is important, due to the high noise created by tokamak current drive. Wooden blocks, treated to be conductors under high voltage are utilized to secure the insulated base (figure 4.13), which the core electronics are mounted to. A small portion of the case is however, still open to radiation. Here, an acrylic, insulated strip is utilized as an attachment point for externals to the device.

4.4 Test Apparatus

An experimental test chamber has been designed and built, in which the dust injector is to be calibrated (Figure 4.14).

4.4.1 Vacuum Chamber

The main chamber has a cylindrical design, with five CF 2.75" ports located around its lateral surface. The front and back of the cylinder connect to a CF 8" flange. The front port of this cylinder serves as the main chamber view port, which is seen facing outward in Figure 4.14 (which yields a visual of the entire test chamber). The rear port is

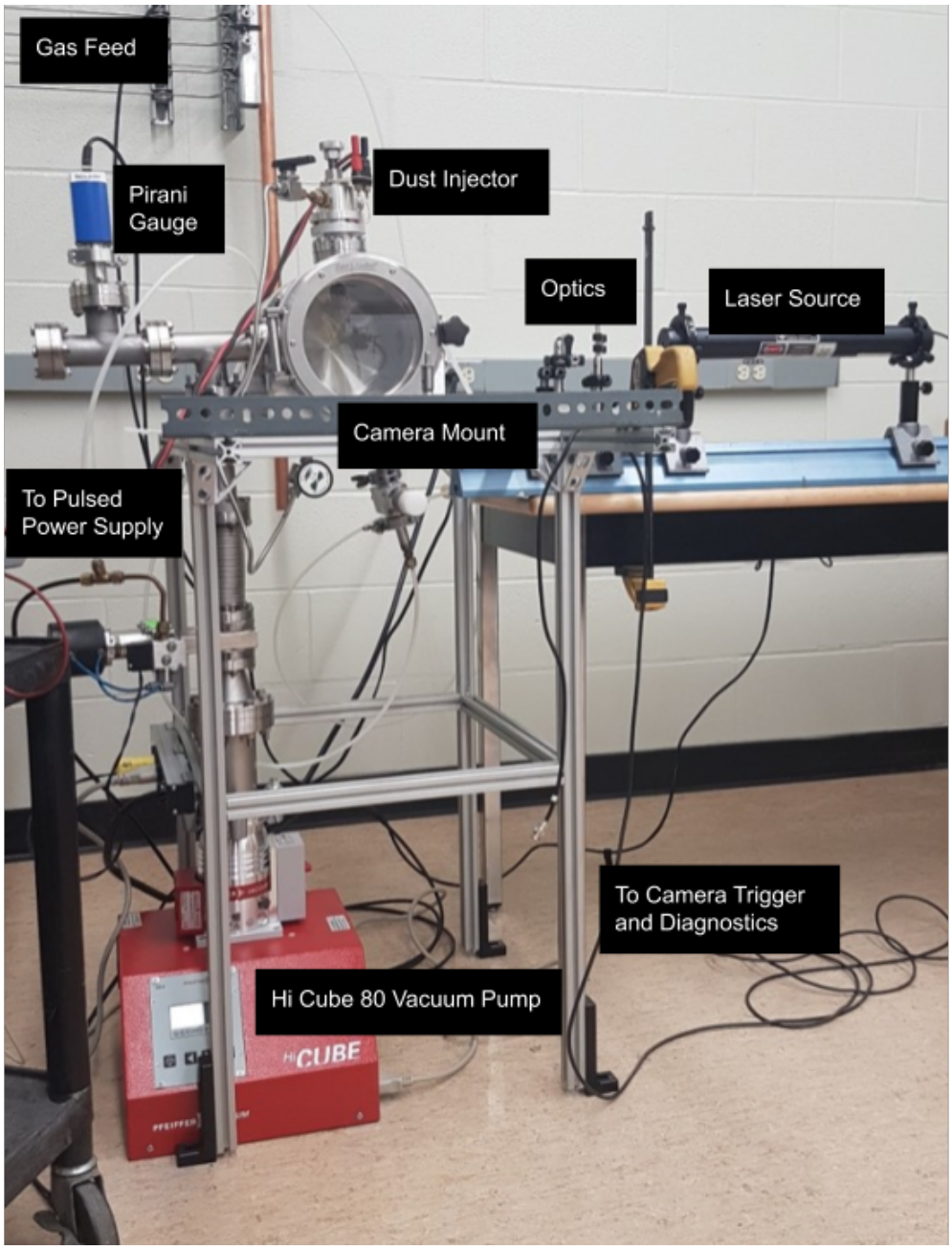

Figure 4.14: Full Test Apparatus

simply capped with a blank. The chamber is currently fixed on two custom mounts. One located at the front of the cylinder, the other at the back. These mounts are secured to the aluminum T bar frame of the apparatus, via screw points within the mounts. The chamber is held firmly in position with the use of two plastic straps, the ends of which are secured to the aluminum T bar frame. Additional zip ties are used to avoid rotation of the chamber on its smooth mounts.

All five ports of the main chamber are utilized. The dust injector is seen attached to

the top of the chamber. Electrical connections may be seen leading to the pulsed power supply. Additionally, two swagelok valves are connected to each side of the injector. One enables the injector chamber to be evacuated to chamber vacuum, while the other enables it to be pressurized with gas.

Moving clockwise around the main chamber, a view port is attached, such that the laser sheath (Section 4.4.4) may pass through the chamber. Next, a needle valve is attached on the bottom right of the chamber. Connected to pressurized gas, this allows the chamber pressure to be finely adjusted to +/- 1 μTorr. Next, Connected to the bottom left of the chamber is a stainless steel compression valve, which fits to a swagelok. When closed, this separates the top dust injector chamber, from the main chamber. Conversely, the injector chamber pressure and main chamber pressure may be equalized when this valve is open.

Finally, the most complex portion of the test chamber is located to the left of the main chamber. Two Tee's are attached here. The outermost Tee connects the cold-cathode pirani gauge, utilized for vacuum measurement and the second 2.75" view port which caps the end. The innermost Tee connect the vacuum chamber to the pump (Section 4.4.3) through a series of connections.

From top to bottom, a butterfly valve is used for the ability to conveniently and quickly halt pumping in the main chamber. Secondly a CF 2.75" extension is used in order compensate for the length of the pump connection. Afterwards, a flexible connect is attached. This connection helps to both compensate for alignment error in the pumping connection and to decouple vibrations from the pump to the rest of the vacuum system. Next, a pneumatic gate valve is used, which serves as protection for the turbo pump. The gate valve may be manually closed by removing power, or will automatically close in the event of a pressure decrease in the gas line, indicating a leak in the system. Finally, two adapters are used: a CF 2.75" to CF 4.5" is connected with a CF 4.5" to ISO K 4.5" which connects to the turbo pump.

4.4.2 High Speed Camera

The Chronos 1.4 high-speed camera, developed by Kron Technologies Incorporated, is utilized as the camera for this experiment. It is mounting on a screw, secured to a steel slotted angle iron, positioned in front of the main chamber window (see figure 4.14). Software version 3.1 was utilized during data acquisition. The camera has a monochromatic image sensor, allowing a maximum resolution of 1280x1024 @ 1057 fps, with a maximum frame rate of 38500 fps. 12 bit raw video data was recorded with a lens having: 6-60 mm focal length and F-number = 1.6.

4.4.3 HiCube 80 Vacuum Pump

The HiCube 80 is a self contained high vacuum pump system, developed by Pfeiffer Vacuum GmbH. It contains both a turbo and roughing pump which are controlled and monitored via electronic display. The turbo pump has an ultimate pressure of $7.5 \times 10^{-8}\ Torr$, which allowed the vacuum chamber (Section 4.4.1) to reach pressures on the order of $10^{-6}\ Torr$.

4.4.4 Laser Sheath

A simple and inexpensive laser sheath was built in order to track dust particles which are released from the dust injector. The system consists of a simple optical rail, a laser with two mounts, an iris, and a specific cylindrical diverging/converging lens pair with cylindrical lens holders and mounts. The Hughes 3225H-PC, 10 mW, 632.8 nm helium-neon laser is used for this experiment. Figure 4.15 illustrates the laser sheath setup.

Setting up the laser sheath is a simple exercise in geometric optics. Figure 4.16 illustrates the relevant dimensions of the beam. Ideally, we wish for the focal points of the initial and spread beam (outgoing beam) to be at infinity. Thus, we design the system with this assumption, simply placing lens 2 at the focal point of lens 1 in order to offset the diffraction needed to widen the beam.

Utilizing similar triangles, the following relationship between the focal lengths of the

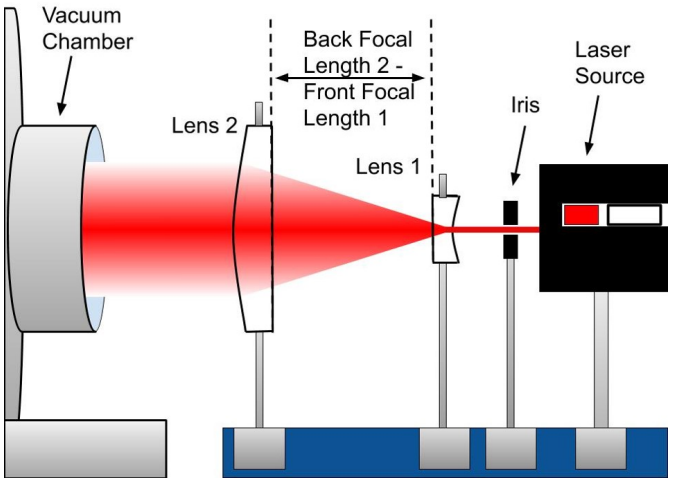

Figure 4.15: Laser Sheath Optics Train

lenses and the ingoing and outgoing beam diameters is obtained:

$$\frac{r_s}{r_0} = \frac{f_2}{f_1} \tag{4.7}$$

where, r_0 and r_s are the respective initial and scaled beam radii in the plane and f_1 and f_2 are the lens 1 and lens 2 focal lengths respectively.

Focal lengths of lenses 1 and 2 were chosen such that the initial beam of 1 mm radius, would expand to the approximate radius of the CF 2.75" chamber view port. Also, small lenses were desired for cost efficiency. Ultimately, the focal lengths of lenses 1 and 2 where chosen to be 3.9mm and 60mm respectively. A laser sheath width of 30 +/- 1 mm was measured.

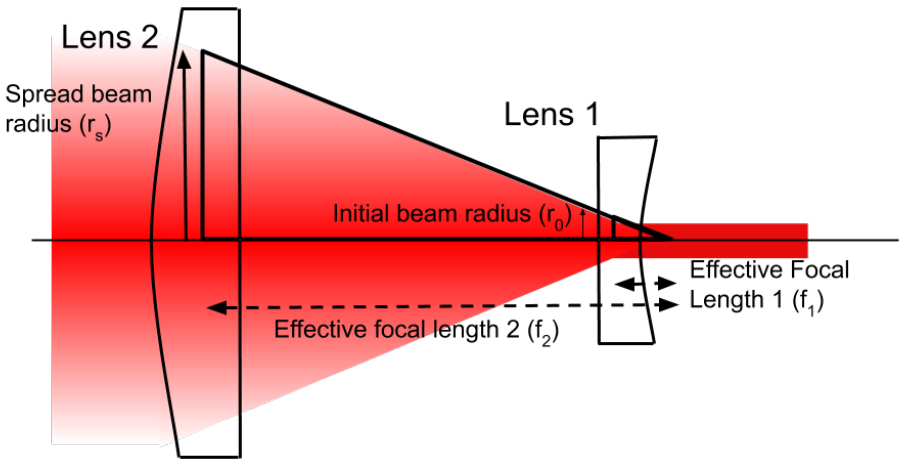

Figure 4.16: Laser Sheath Design

Chapter 5

Dust Injector Calibration

5.1 Introduction

A full characterization of the dust injector is required for dust injection experiments we wish to conduct on STOR-M. Two key pieces of information are required for this characterization. First, we require information on the shape and location of the dust plume, as it evolves with time. Second, the total injected mass of tungsten dust is required. Additionally, the amount of gas injected must be quantified. Figure 5.1 illustrates the data acquisition method, which will allow us to perform this characterization.

The dust injector is electrically triggered in order to begin dust injection into the vacuum test chamber. This electrical trigger for the dust injector is also shared with the camera trigger. As a result, the first recorded frame of the camera corresponds to the initial motion of the dust injector piston and thus the start of dust injection into the vessel. Dust particles are not observed in the experiment until they reach the laser sheath. The top of the laser sheath is located a distance, h_s (= 0.14 cm) below the dust injector screen. As particles travel through the laser sheath, scattered light is detected by the camera. A recording duration is chosen to be long enough (370 ms), such that dust particles are no longer found to be falling within the last recorded frame. Close to the end of recording, particles left within the frames have reached the bottom of the chamber and can be seen ricocheting back into the laser sheath. The plume may essentially be reconstructed from the observed trajectories of individual particles within the laser sheath

over the duration of the plume (t_1 - t_2). The extracted velocities of particles crossing the laser sheath, yield the basic structure of the plume at any time, assuming evolution of each particles under free fall. From this, the plume width and vertical location given by h_1 and h_2 may be determined. Furthermore, particle count data may simply be used to determine the total injected mass, assuming spherical tungsten dust particles.

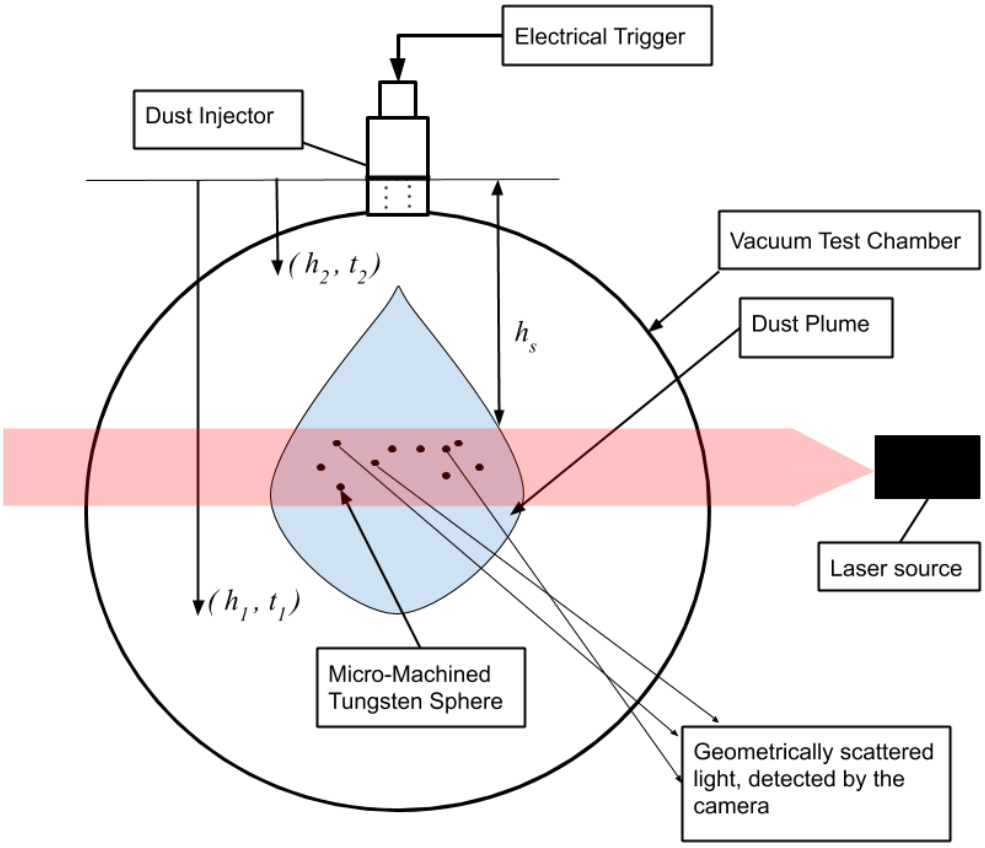

Figure 5.1: Data Acquisition Scheme for Dust Injector Calibration. The details of the test apparatus optical system in Figure 4.14 are shown.

5.2 Micro Machined Tungsten Dust

Micro-machined, spherical tungsten powder will be utilized to simulate reactor dust in the foreseen experiment using STOR-M. This powder was produced by Tekna Plasma Systems Incorporated and is graciously provided by our collaborators at the French alternative energies and atomic energy commission (CEA), Cadarache, France.

The size distribution of dust particles must be determined in order for meaningful

statistical analysis of injected particles to be conducted. In order to do this, a sample of tungsten dust was prepared for electron microscope imaging. Firstly, a small amount of dust was suspended colloidal in an alcohol solution with a syringe. Secondly, this solution was then injected onto a sample slide and left to dry. Utilizing the Hitachi SU8010, FE-SEM at the University of Saskatchewan, multiple images were taken of the tungsten dust sample. Figure 5.2 shows a characteristic, sample image. Unfortunately, micro-particle tungsten dust is dense and sticky enough that it tended to cluster together when it was injected onto the sample slide. Due to the overlap in particles on the sample slide, manual tracking was required.

Utilizing ImageJ software [83], The diameter of 1,842 tungsten particles were manually measured. The resulting data was fit to a log-normal distribution illustrated in figure 5.3. The log-normal distribution is given by:

$$f(s) = \frac{1}{\sqrt{2\pi}\sigma_d s} \exp\left(-\frac{1}{2}\left[\frac{ln(s) - \mu_d}{\sigma_d}\right]^2\right). \tag{5.1}$$

Here, s represents the diameter of dust particles. μ_d ($= 2.979$) and σ_d ($= 0.265$) are respectively the log-normal distribution parameters, related to the mean and standard deviation. If you were to take the exponential of these parameters, they would have units of μm.

5.3 Theory of Particle Tracking Velocimetry

Particle tracking velocimetry (PTV) is utilized in order to detect and subsequently trace the trajectories of countably many particles, with particular features. In general, a PTV algorithm must first define the objects, comprised of pixel clusters within the image frame, which it is looking for. In the the case of trackpy, which is used for this experiment, multiple variables enable the identification of objects with various brightness and size characteristics, possibly taking into account noise considerations in the data [26, 84].

Once the detection specifications have been set, the PTV algorithm effectively tries to find where particles in the current frame were located in the previous frame. This serves

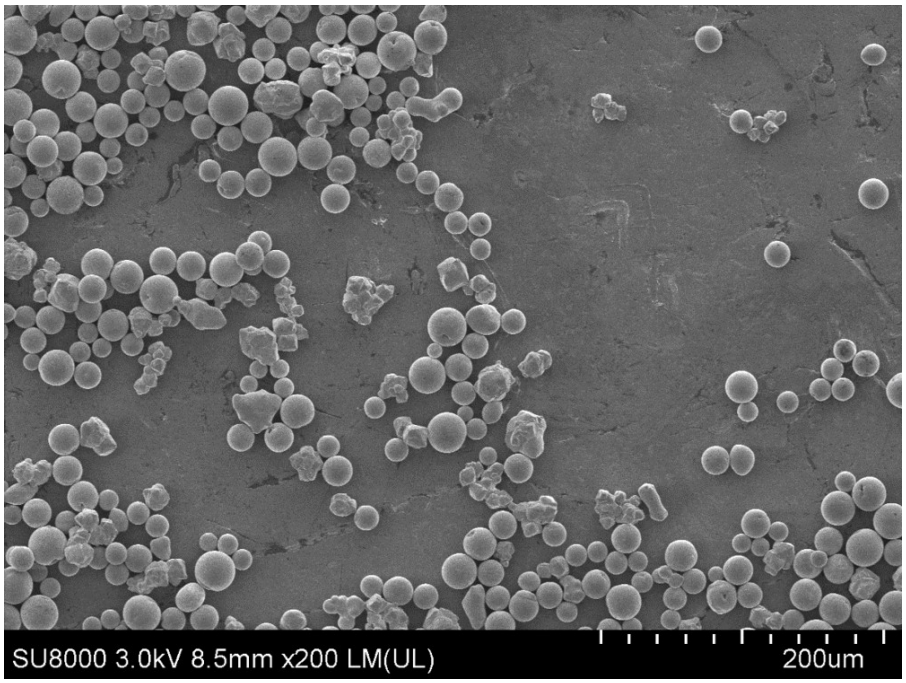

Figure 5.2: SEM Image of Tungsten Micro Particles

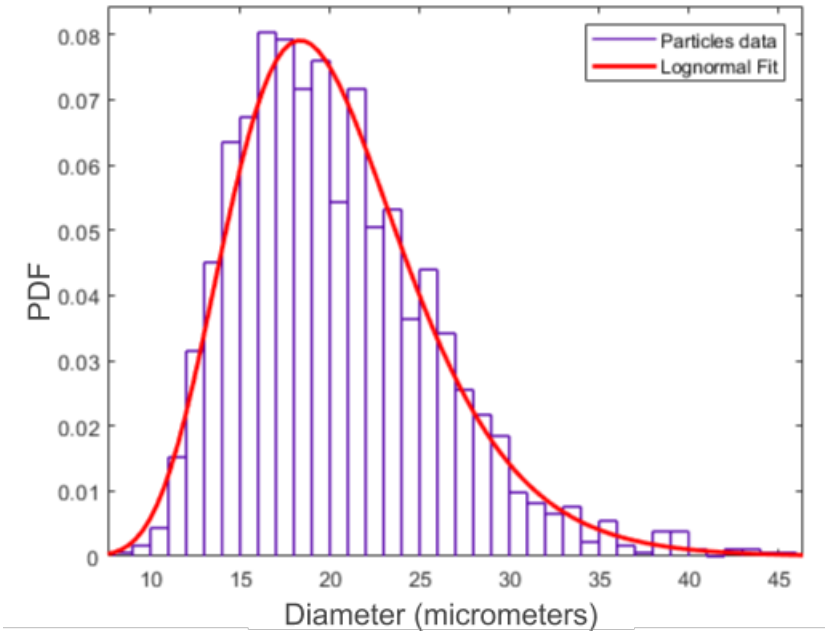

Figure 5.3: Size Distribution for Tungsten Dust.

to establish particle trajectories and is accomplished via an algorithm based on nearest neighbour detection [84]. For this reason, particles should not move much from frame to frame, as the algorithm is designed to detect small changes in position. In the case of trackpy, more sophisticated detection is enabled by identifying an associated velocity

with the mapped trajectory. Multiple variables may also be tuned for enhanced trajectory mapping, including: desired velocities, particle counts, particle separation, particle edge contrast and number of sightings to constitute a valid trajectory. Additionally, the algorithm may allow for particles to be missing in a few intermediate frames, while still producing an accurate trajectory.

5.4 Dust Injection Reconstruction

5.4.1 Particle Detection

12 bit tiff images, reconstructed from raw data captured by the camera, must first be preprocessed in order to optimize the feature detection process, implemented using Trackpy. The camera zoom, focus and distance from the laser sheath are all fixed in the dust injection experiment, thus all image frames have the same spatial calibration factor of 16.5 μm/pixel. Initially, images are found to posses background noise due to miscellaneous reflections within the vacuum chamber. The dust particles also appear slightly elongated in the direction of motion, due to the length of exposure time. This elongation serves to increase the apparent size of dust particles, allowing detection of particles which may otherwise be undetected.

With the use of a Gaussian filter, the noise found in the original images is smoothed. In order to implement a Gaussian filter for image processing, we must discretize the two-dimensional Gaussian function. As a result, the Gaussian filter matrix elements are describe by the following equation:

$$G_{xy} = \frac{1}{2\pi\sigma^2} \exp\left(-\frac{x^2+y^2}{2\sigma^2}\right), \tag{5.2}$$

where, σ is the standard deviation, x and y are respectively the discrete horizontal and vertical coordinates of the image frame pixels. In the context of image analysis, G is

known as the kernel. The Filtered image is defined by the following convolution [85]:

$$F_{ij} = (G * I)_{ij} = \sum_{a=1}^{n} \sum_{b=1}^{m} G_{ab} I_{(i+a-1)(j+b-1)}, \tag{5.3}$$

where, F_{ij} represents the filtered matrix elements, G represents the image kernel matrix and I represents the original image matrix. Note that n and m respectively correspond the the number of rows and columns in the kernel. As the Gaussian function is technically non-zero over its domain, the kernel matrix is theoretically infinitely large. However, impact of the kernel is only relevant in practice to within a few σ. Thus, the size of the kernel is finite and may in fact be relatively small compared to the image. As is required, this operation results in a filtered image with the same size as the initial image.

When choosing a Gaussian filter, the correct choice of σ is very important. Image filtering should be impactful enough to eliminate so called “salt and pepper noise", while not so overwhelming as to blur the dust particles which are being tracked. Figure 5.4 shows a comparison between the unfiltered image and various values of σ.

This smooth noise level is a drastic improvement to the original, due to the fact that it suppresses the intensity of peaks in the noise, which have comparable intensity to the dust particles we wish to track. The use of a longer exposure time (without saturation) is justified due to the enhanced particle brightness, improving detection. If the exposure were set too low, dust particles may be missed entirely. Finally, a binary threshold is applied on top of the Gaussian filtered frames, allowing for much easier particle detection by the algorithm. Figure 5.5 illustrates the results of this preprocessing routine.

Particle tracking is implemented on the processed, binary frames. The results of particle tracking are illustrated by Figure 5.6. During the tracking process, there are a few errors which regularly occur. Some of these are a result of noise which is still present in the data. As a consequence, the algorithm may detect a dust particle where none are present. This may be corrected by only considering particle trajectories which are linked through at least three consecutive image frames. Furthermore, the vertical velocity component of particle trajectories, must be at least as great as a particle falling under free fall, with zero initial velocity. This is due in part to the fact that particles do not appear to interact once

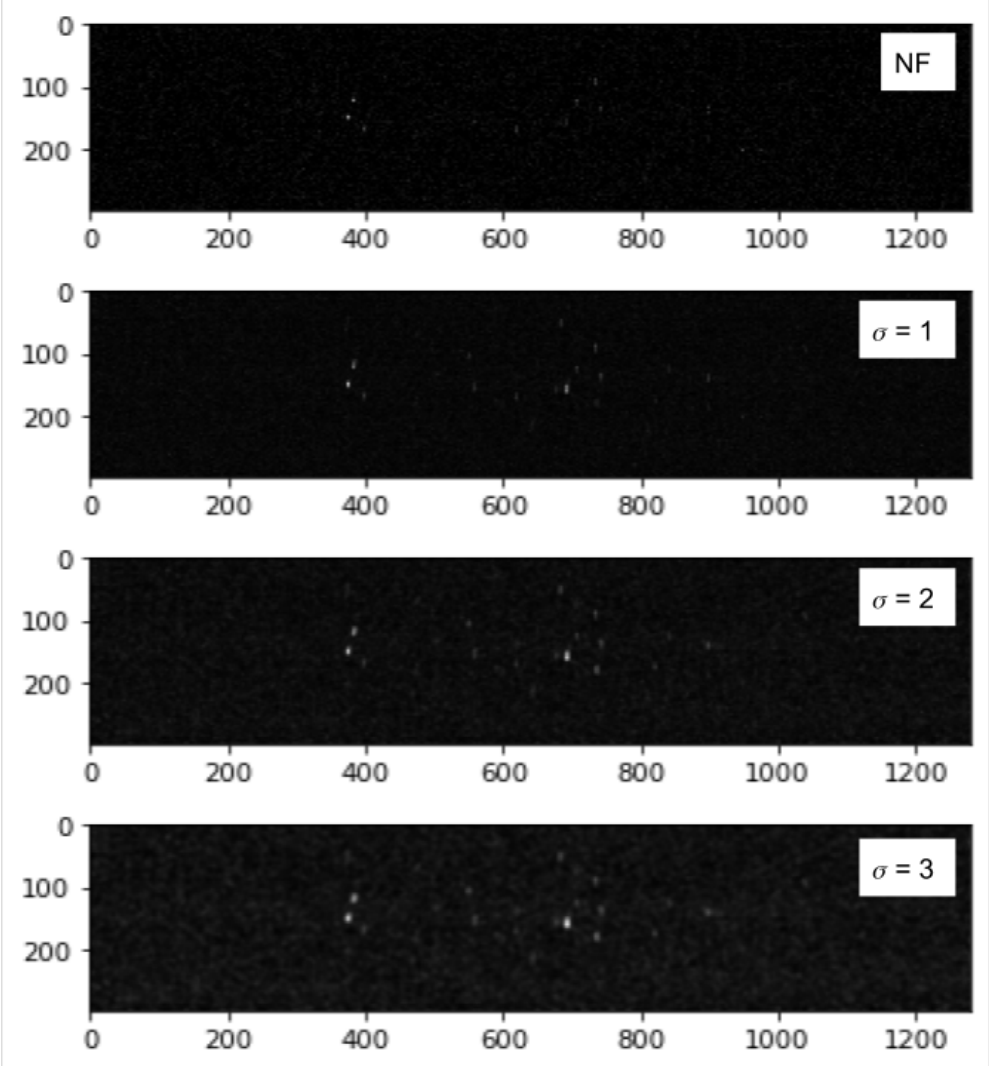

Figure 5.4: Effect of σ on Image Filtering. The unfiltered image is represented by, NF. Gaussian filtered images with σ value of 1,2 and 3 are shown. Here it is found that $\sigma = 2$ has the best trade off between noise reduction and particle contrast against the background.

injected past the screen. This may be explained due to the fact that dust particles are injected in sufficiently low numbers, such that they take up very little space within the test chamber. Along with the small size of dust particles, this results in an associated small collision cross section. This is seen in the final trajectories of particles, as they appear to follow straight lines within the illumination of the laser sheath. These trajectories are truly parabolic arcs when the entire trajectory is visible, validated by the plume reconstruction in Figure 5.11. Also, friction was found to be negligible as the Epstein drag force on dust particles was multiple orders of magnitude smaller than gravity.

There is also error due to counting multiple close particles as one unique particle.

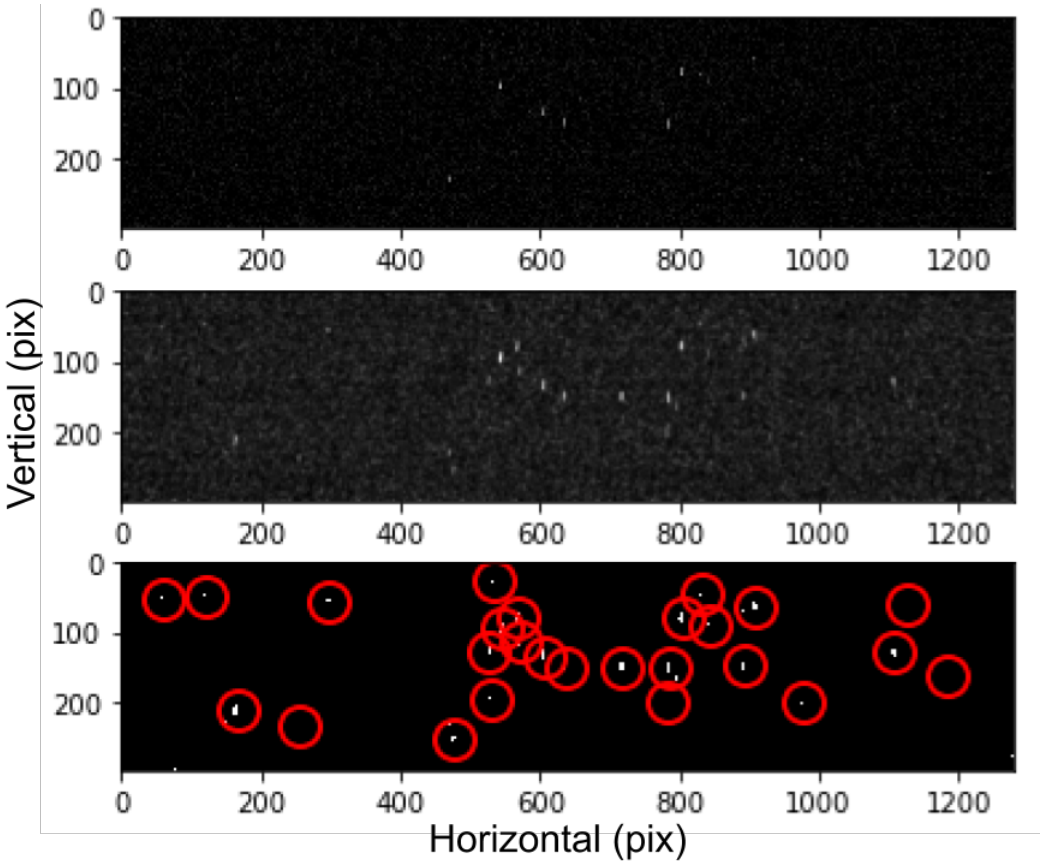

Figure 5.5: Processing Scheme for Dust Particle Tracking Data. Dust particles are shown, illuminated from the light of the laser sheath. The top image illustrates 12 bit raw image data collected during the experiment. Upon application of a second order Gaussian filter, the middle image is attained. The bottom image shows the effects of an applied binary threshold to the middle image. Tracked particles are circled in red.

This error is magnified as higher numbers of particles appear within the frame. In order to combat this, a count correction factor is established based on the intensity of light collected by the camera. The details of this correction factor are given in Section 5.5.

5.5 Reconstruction Analysis

5.5.1 Calibrating Particle Count

In order to gauge and correct for systematic error in particles detection, the intensity profiles of images taken may be utilized to accurately determine the number of particles on screen. In order to use this method, the intensity profile must map to a particle count. To obtain proper statistics, this operation will be interested in finding the intensity profile

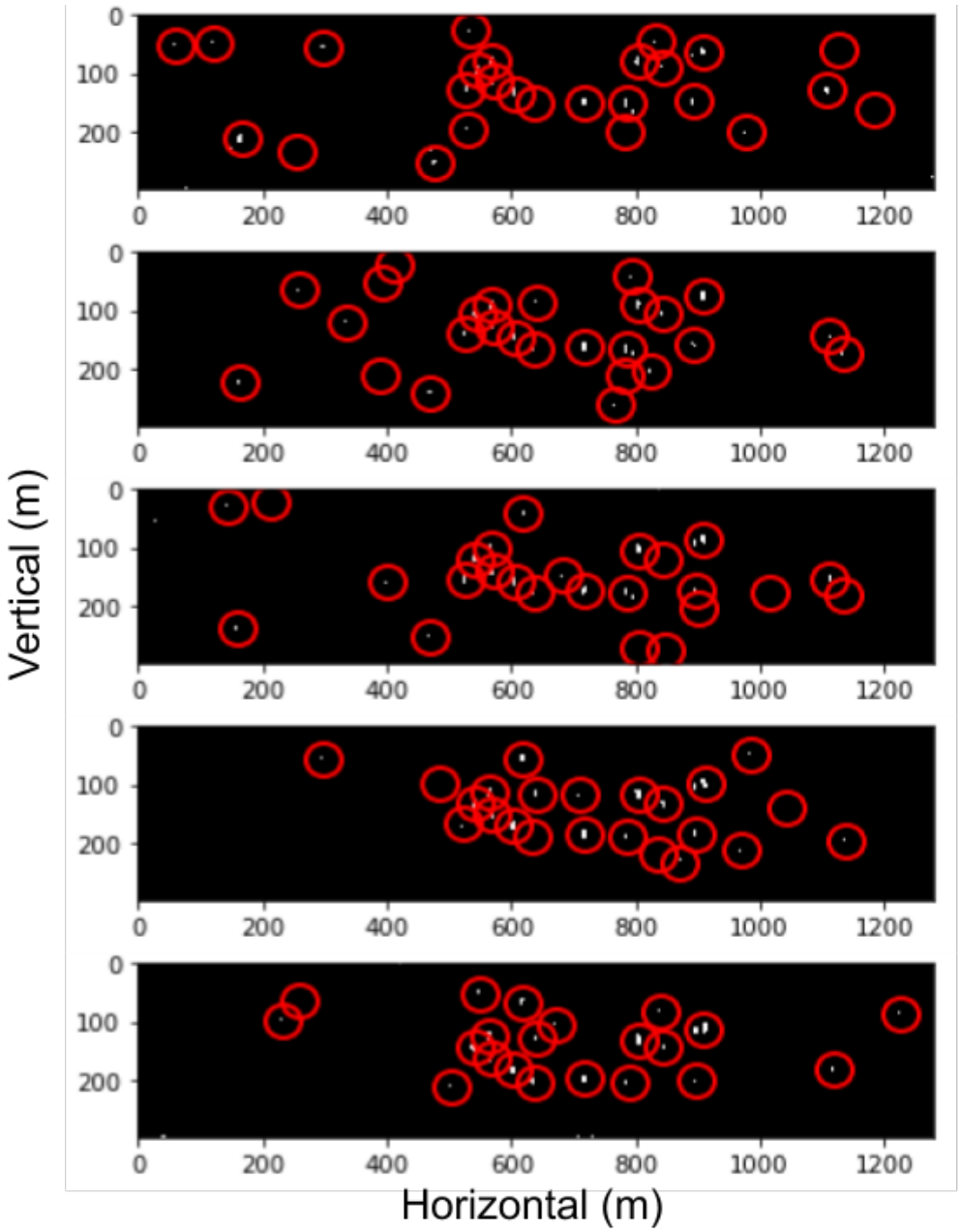

Figure 5.6: Particle Tracking Efficiency. The fall of dust particles within the laser sheath is shown over five sequential frames, ordered from top to bottom. The frame rate is 2162 fps. Here we notice that particles generally appear to move small amounts between frames and are detected appropriately. Tracking error is still present in the form of detected black regions and multiple particles contributing to a single detection, when particles are very close. This effectively results in the under counting of particles within the laser sheath. Section 5.5.1 describes the correction technique implemented to circumvent this error.

within the frame, during a particular time interval.

A manual particle count was conducted, yielding Figure 5.7, where x represents the horizontal position across the field of view of the camera. From this count, a metric was obtained for the number of particles crossing through the laser sheath. The count was

conducted over a 100 frame interval, utilizing particles found over the entire region of the frame. The normal distribution function obtained was then fit to the average intensity profile obtained during the same time interval. Figure 5.8(a) illustrates the correlation between particle number and intensity, with a normal distribution fit, utilizing the same μ (average) and σ (standard deviation) as in Figure 5.7.

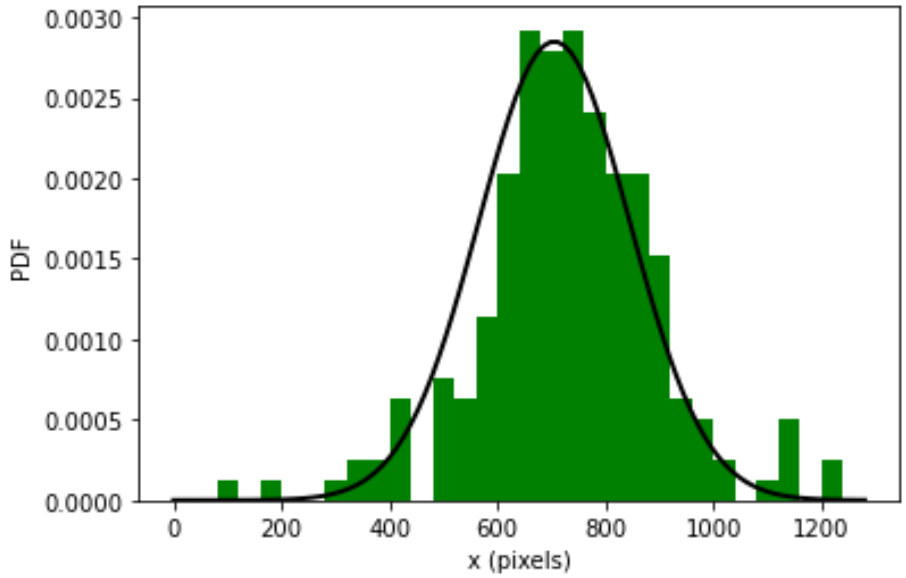

Figure 5.7: Manual Count and Normal Distribution Fit for Falling Dust Particles. $\mu = 705$ pixels and $\sigma = 140$ pixels. Here, μ is found to corresponds with the center position of the cylindrically symmetric dust injector. Injector voltage was set at $400V$ with a chamber pressure of $10^{-}5\ Torr$. The 10 μm screen was utilized. Particle contribution is from frames 300 to 400 at 2162 fps. 195 particles were counted in this figure with 32 bins.

The amplitude and offset of the intensity distribution change with time, as varying amounts of light illuminate the screen. Furthermore, changing injector voltage and pressure also change the amplitude and offset of the intensity profile. Though, for the same screen size, μ and σ are constants. This is illustrated by Figure 5.8(b). The light intensity distribution seen by the camera is described by the Gaussian fit as follows:

$$f(x,t) = \frac{A(t)}{\sqrt{2\pi}\sigma} \exp\left(-\frac{1}{2}\left[\frac{x-\mu}{\sigma}\right]^2\right) + C_{bl}. \tag{5.4}$$

Here, $A(t)$ is a time dependant amplitude, which changes as more particles pass into the cameras field of view. C_{bl} represents the increase in background light, as a consequence of increased reflection from a greater number of injected particles. Comparing Figures 5.7

and 5.8(a), we deduce a simple, though key calibration factor. For a 30 unit peak average pixel intensity, using the 10 μm screen, approximately 200 particles have passed through the laser sheath in a 100 frame (46 ms) time interval. In other words, every 30 units of the peak pixel intensity corresponds to an average particle flow rate of $\frac{200}{46}$ particles/s on the recorded interval. Utilizing this result, it is possible to correct the count of the tracking algorithm, via cross referencing the light intensity captured by the camera.

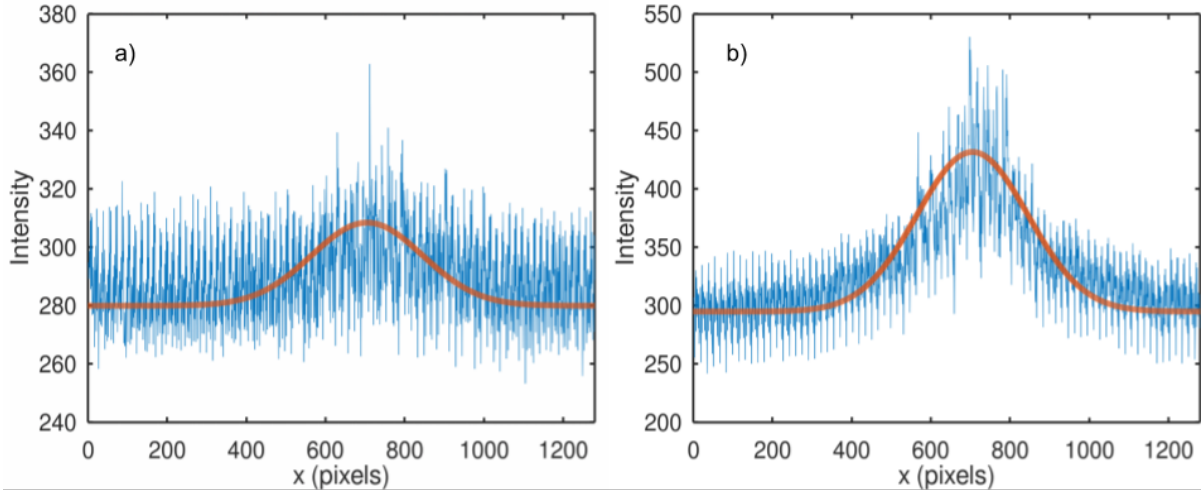

Figure 5.8: Fitted Intensity Distribution. $\mu = 705$ and $\sigma = 140$. The following intensity values are averaged over the laser sheath. The camera intensity ranges from 0 to 2^{16}, utilizing 2^{12} possible values within this range. The fluctuation seen in the Intensity data result after averaging the vertical pixel brightness for each x value. When intensity is plotted against x, data points do not connect smoothly due to random background noise fluctuations found across the screen. The following data was collected with the 10 μm screen.
a) Injector voltage was set at $400V$ with a chamber pressure of $10^{-}5\ Torr$. Contribution from frames 300 to 400 at 2162 fps.
b) Injector voltage was set at $450V$ with a chamber pressure of $10^{-}5\ Torr$. Contribution from frames 400 to 500 at 2162 fps.

Light intensity based measurements are proportional to the reflected area of particles. As a consequence, injector screens require different intensity calibrations, based on the mean diameter of particles allowed to pass through. The calibration factor may be determined for any secondary screen, by multiplying the 10 μm screen calibration factor by the following constant:

$$a_{screen} = \frac{\bar{A}_{10\mu m}}{\bar{A}_2} = \left(\frac{\bar{s}_{10\mu m}}{\bar{s}_2}\right)^2. \tag{5.5}$$

Here, $\bar{A}_{10\mu m}$ and $\bar{A}_2$ are the average reflected areas of particles let thought the 10 μm and secondary screen respectively and $\bar{s}_{10\mu m}$ and $\bar{s}_2$ are the average diameters of particles let thought the 10 μm and secondary screen respectively. This results in increased particle count for average dust diameters smaller than 10 μm and visa versa for diameters greater than 10 μm.

5.5.2 Particle and Gas Injection

A subroutine has been devised, which takes as input, the trajectory data from tracked particles in Section 5.4. For each unique particle trajectory, averages are computed for the vertical velocity and radial position (r), where $r = 0$ along the center axis of the dust injector. As there remain particular instances of miscounted particles in the data, a threshold value for particle velocity is set. This value ensures that particle velocities in the sheath are at least as great as free fall velocity entails. Additionally, a simple first order forward difference method is utilized for the algorithms velocity calculations. Based on the agreement between reconstructed data in Subsection 5.5.3 and visually inspected raw data, this is deemed to be sufficient. Velocities and radial positions are then binned according to the time interval they are found present within the laser sheath.

Vertical velocity measurements are rather straight forward. The average of the velocity distribution of particles varies slightly for different screens and injection voltages/pressure configurations, though is generally found to be peaked at approximately 1.8 m/s. This value is found to be consistent for both PTV data and manual tracking data. Due to the positioning of the screen above the laser sheath, this velocity indicates that free fall conditions are enough to describe the particles velocity, possibly with a small boost from the dust injector piston. In contrast to the aforementioned simplicity of particle velocities, the radial distribution of particles requires a slight correction.

Assuming a conical symmetry of the dust cloud, predicated on the cylindrical symmetry of the dust injector, the total number of particles injected may be determined from those observed in the laser sheath. For particles observed at various radii, the total number of particles scales proportionally to the ratio of the total area to the observed area, illustrated

in figure 5.9. Here, the scaling factor (S) for the area of the dark blue line which is not contained within the laser beam is simply:

$$S = \frac{2\pi}{2\theta} = \frac{2\pi}{4\sin^{-1}(\frac{w}{2r})} \approx \frac{\pi r}{w}, \tag{5.6}$$

where, θ is the angle extended from the center of the dust plume to the beam width, w at radius r. The beam width is relatively thin at 2 mm, making it an order of magnitude smaller than the diameter of the dust cloud passing through the laser. For this reason, the small angle approximation is justified in equation (5.6).

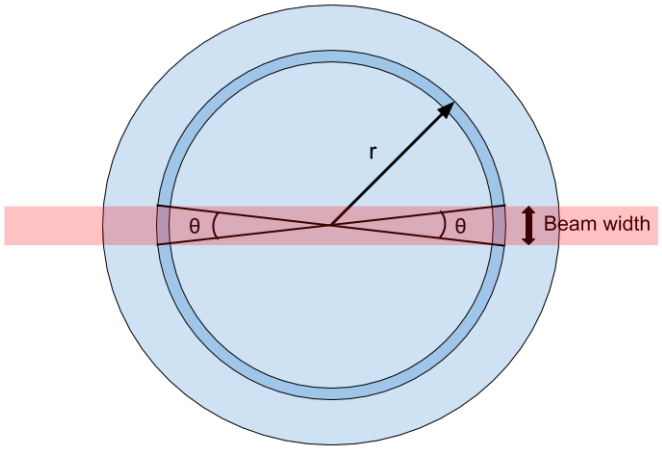

Figure 5.9: Dust Cloud Top View

Upon implementation of radial particle scaling, it is possible to determine the total number of injected particles into the test chamber. This is encapsulated by an original count. Upon implementation of the intensity based correction methods in Section 5.5.1, the corrected particle count may be determined. A substantial difference between the two counts is illustrated in figure 5.10. Table 5.1 shows a summary of the results for injected dust mass using various dust injector parameters.

Data was also collected in order to calibrate the gas puff during dust injector operation. By closing the gate valve on the test chamber, just before triggering the dust injector, an injection pressure was recorded. For an extreme case, where the dust injector voltage is set to 450 V at either 10^{-4} or 10^{-5} Torr, the injection pressure was found to be 20 mTorr. The pressure measured in the test chamber can be converted to an equivalent pressure

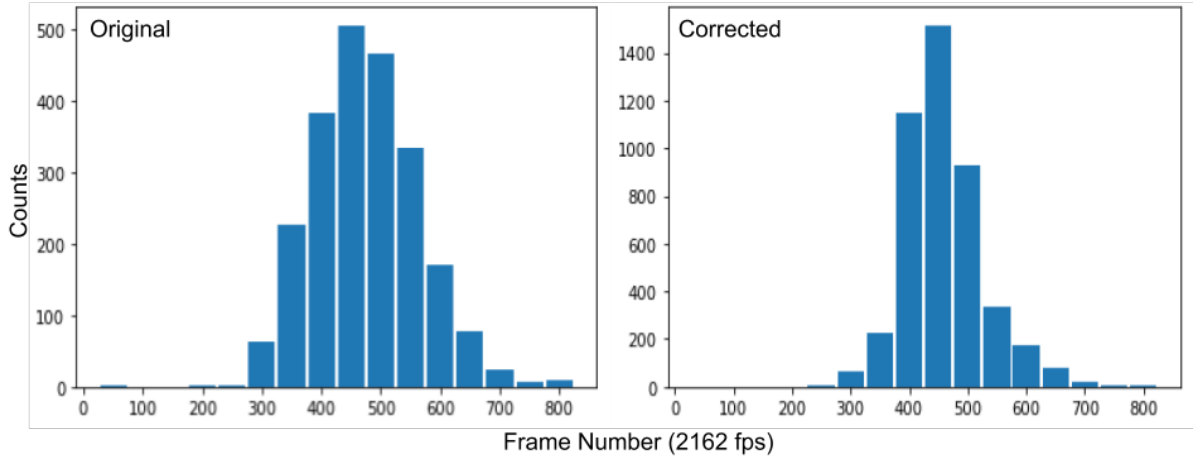

Figure 5.10: Temporal Evolution of Dust Particles Present in the Laser Sheath. The following data was produced from the average of the particle count, taken over eleven experiments in order to produce viable statistics for a single injection. The time in seconds may be determined on the horizontal axis, through division by 2162. Here, the results of particle counting before and after camera intensity correction are illustrated respectively as Original and Corrected. The correction is done for frames within the time interval of the bins plotted. Light intensity is only found to be required for the highest particle influxes, seen between bins 400 - 500. The total number of measured particles in the Original data and Corrected data are found to be 2268 and 4510 respectively. Thus, the correction shows an initial under counting by a significant factor of 2 times (utilizing the 10 μm screen at 400V).

in the much larger volume of STOR-M. This may be simply computed using the ideal gas law [86], considering constant temperature and injected number density. Given the test apparatus and STOR-M chamber volumes respectively as, 4 L and 218 L, a pressure increase of 0.37 mTorr is computed for STOR-M. This is found to be acceptable, as the pressure increase is of the same order of magnitude as that produced by fuel injectors currently outfitted on STOR-M.

Table 5.1: Injected dust mass for various combinations of dust injector voltages and screens. Green highlights conditions which are possibilities for experiment in STOR-M, without plasma quench. Red outlines conditions where quench of the STOR-M plasma is expected, due to excessive dust injection.

Screen Sieve Size (µm) \ Voltage (V)	250	350	400	450
5	NA	0.2 +/- 0.1	1.2 +/- 0.3	9.7 +/- 2.0
10	NA	3.8 +/- 0.8	35 +/- 7	264 +/- 53
14	NA	33 +/-17	> 145	
25	95 +/- 48	NA	NA	NA

Average Injected Dust Mass (µg) Based on the Injector Screen and Voltage

5.5.3 Reconstruction of the Dust Plume

In order to determine the structure of the dust plume, another subroutine, complimentary to that in the preceding Subsection has been devised. The algorithm employed is based on the same analysis of the original particle tracking data, used in determining the number of injected particles. However, unlike the previous subroutine which effectively measures and outputs the injected particle count, this algorithm extrapolates particle positions from there initial injection to an arbitrary time, simply assuming gravity as the only active force. In order to construct this relatively simple simulation, the velocity and time of arrival of particles in the sheath must both be utilized.

Considering the velocities of observed trajectories, the initial velocity of any dust particle may be determined as follows:

$$v_{y0} = \sqrt{\left(v_y^2 - 2g(y + h_s)\right)}, \tag{5.7}$$

$$v_{x0} = v_x, \tag{5.8}$$

where, v_{x0} and v_{y0} are the respective horizontal (x) and vertical (y) initial velocities of dust particles, v_x and v_y are the respective average velocities of particles within the laser sheath at the corresponding (x,y) coordinate within the laser sheath, g is the acceleration due to gravity and h_s (= 14 cm) is the height of the dust injector screen above the laser sheath.

The injection time of a dust particles into the test chamber (t_0) may be determined as follows:

$$t_0 = t - t_{fall}, \tag{5.9}$$

where, t is the time which has passed since the dust injector trigger and t_{fall} is the time it takes for the particle to reach the laser sheath, based on the vertical velocity it was observed traveling at within the laser sheath and the inferred initial velocity. t_{fall} is determined by solving for the positive root of the vertical dust particle position as follows:

$$t^2 + \frac{2v_{0y}}{g}t - \frac{2(y+h_s)}{g} = 0, \tag{5.10}$$

$$t_{fall} = \sqrt{\frac{v_{0y}^2}{g^2} + \frac{2y}{g}} - \frac{v_{0y}}{g}. \tag{5.11}$$

Knowing both the injection time and initial velocities of particles enables the determination of the dust plume at an any time during it's evolution. The dust plume may be visualized by overlaying the parabolic paths of all particles on a single plot window at any time. Cycling through times from the dust injector trigger to 370 ms afterwards, where the bottom of the dust plume passes the bottom of the laser sheath, results in a video recreation of the dust injected into the test chamber. The laser sheath itself is found within the vertical range of 14 cm to 15.9 cm. As seen in Figure 5.11, the dust plume reaches the top of the laser sheath between 74 and 148 ms, which agrees with the time dust enters the frame in experiment. Large amounts of dust are seen within the laser sheath around 222 ms, which agrees within the time range of 208 - 231 ms, in which the maximum number of dust particles are observed. As previously mentioned, the final dust particles pass the laser sheath at 370 ms, where the dust plume is fully formed and detached from the dust injector located at (0,0). Finally, the time at which the center of mass of the dust plume reaches the center of the STOR-M tokamak is numerically determined, as shown in Figure 5.12.

5.5.4 Dust Injection Statistics

In order to determine the effects of tungsten injection in STOR-M, we are interested in injecting a precise mass of particles. In addition, the effective mass injection rate should be of order, no more than 1 mg/s [48]. From this injection rate, a maximum injected mass may be inferred for a typical 35 ms STOR-M discharge. Simply multiplying maximum injection rate, by the plasma lifetime, we find a maximum injection mass of 35 μg. Considering this is an approximation, total injection masses on the order of 10^{-5} g will be taken as an upper bound for particle injection.

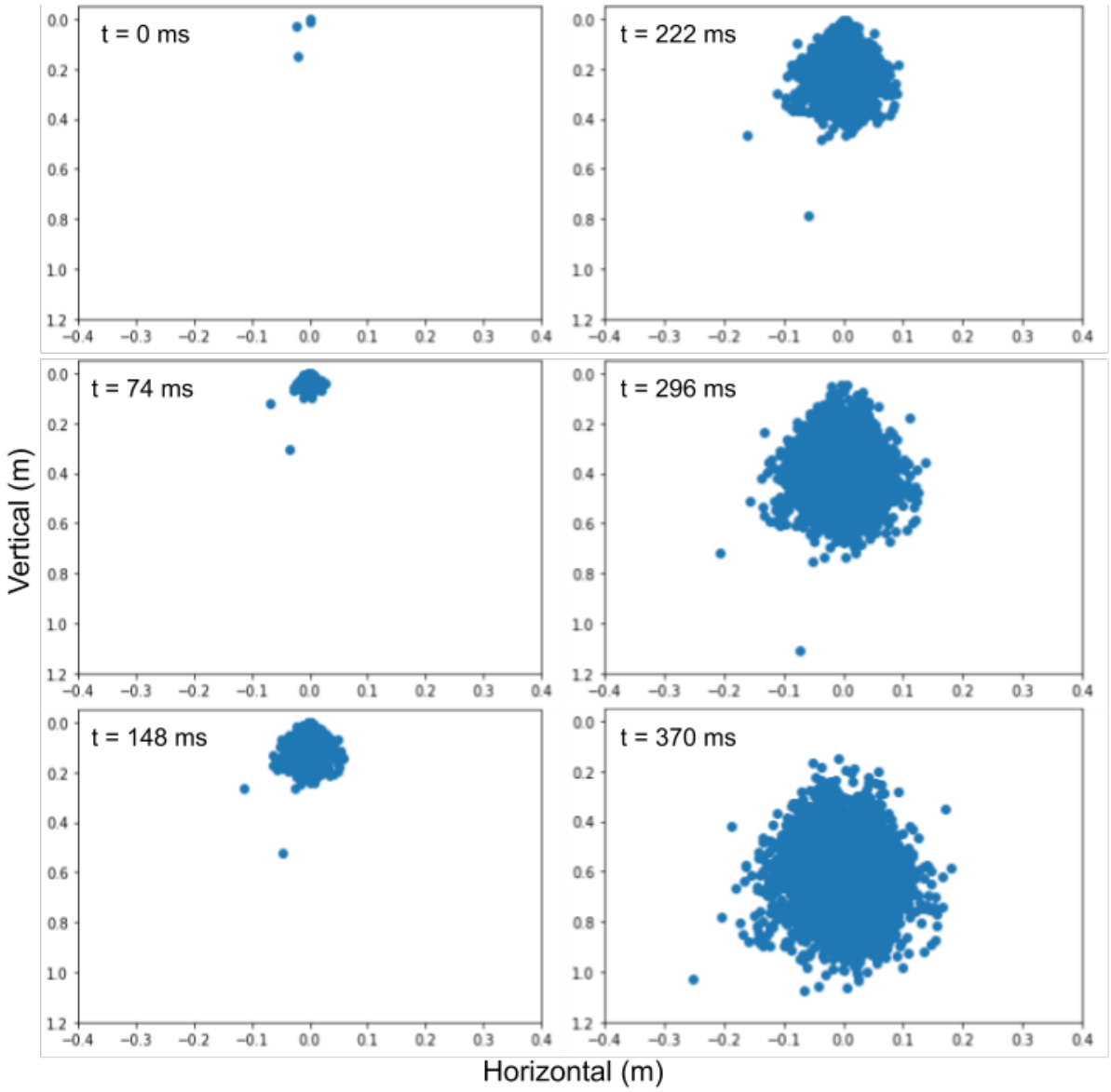

Figure 5.11: Dust Plume Evolution in Time. Individual particles detected over eleven experiments are superimposed on the same plot window at the various times they are found to be injected. Here, we can see that a dust plume manifests as a simple result of the proximity of multiple non-interacting dust particles injected by the dust injector. Relevant dimensions, such as the dust plume width and height may be read from the figure at various times after injection (shown in the upper left hand corner of each subplot).

As expected, when dust is injected, the dust injector screen serves to reduce the maximum particle size. Each screen used in the dust injector will thus have a new size distribution function. This new distribution is equal to $Af(s)$ over the domain of dust particle diameters allowed through the screen and is zero everywhere else. $f(s)$ representing the log-normal dust distribution function given in equation 5.1. The associated

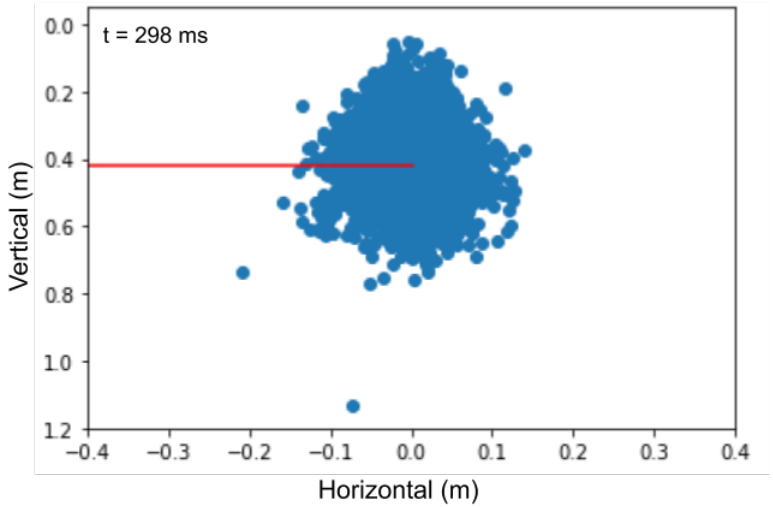

Figure 5.12: Centering The Dust Plume within the STOR-M Tokamak. Here, the red line indicates the position of the center of mass of the dust plume. This position is found to coincide with the center of the tokamak, located at 41.1 +/- 0.4 cm from the dust injector at time, t = 298 +/- 3 ms after dust injection. In this setup the dust injector is mounted on a vertical port, 24 cm in height.

normalization constant A, is determined as follows:

$$A\int_0^{s_{max}} f(s)\mathrm{d}s = 1, \tag{5.12}$$

$$A = 2\left(1+\mathrm{erf}\left(\frac{\ln(s_{max})-\mu_d}{\sqrt{2}\sigma_d}\right)\right)^{-1}, \tag{5.13}$$

where, s_{max} is the maximum particle diameter allowed through the screen. Note, that the integral on the left of equation (5.12) is effectively the cumulative distribution function (CDF) of the log-normal distribution. Once A has been determined, the average size of dust particles through the screen (s_{avg}) is obtained by performing the following integral:

$$s_{avg} = \int_0^{s_{max}} sAf(s)\mathrm{d}s, \tag{5.14}$$

$$s_{avg} = -\frac{A}{2}\exp\left(\mu_d+\frac{\sigma_d^2}{2}\right)\mathrm{erf}\left(\frac{\mu_d+\sigma_d^2-\ln(s)}{\sqrt{2}\sigma_d}\right)\Bigg|_0^{s_{max}}, \tag{5.15}$$

$$s_{avg} = \frac{A}{2} \exp\left(\mu_d + \frac{\sigma_d^2}{2}\right)\left(1 - \text{erf}\left(\frac{\mu_d + \sigma_d^2 - \ln(s_{max})}{\sqrt{2}\sigma_d}\right)\right). \tag{5.16}$$

From Figure 5.2, it is clear that most of the dust particles are indeed spherical, to a good approximation. As the spheres are made of pure tungsten, they each have a constant density. As such, the average mass (m_{avg}) of a tungsten dust grain is simply:

$$m_{avg} = \frac{\pi}{6}\rho_t s_{avg}^3, \tag{5.17}$$

where, ρ_t is the density of tungsten.

Finally, the total average injected mass (m_{total}) may be determined by considering the total number of particles injected through the screen (N_d) as each having the average mass, m_{avg}, allowed for that screen. This is expressed as follows:

$$m_{total} = N_d m_{avg}, \tag{5.18}$$

The error in this method reduces with increasing particle count, as it is likely the particles of higher mass offset the contribution of those with lower mass.

Chapter 6

Conclusion and Future Work

6.1 Conclusion

Dust particles generated by PWI against PFC's inside tokamaks generally have an adverse effect on the confined fusion plasma. In order to solve problems associated with dust in tokamaks, a dust injection experiment has been proposed for STOR-M. In order to prepare for this experiment, many new pieces of equipment were designed and built.

A new dust injector piston has been designed, machined and installed in the CT fast gas valve. This new configuration of the gas valve is referred to as a dust injector. The dust injector is capable of injecting both solid and gaseous material into STOR-M via electronic trigger. This trigger signal is provided by the pulsed power supply, which was designed based on the CT gas puffing fast bank. The pulsed power supply current pulse is shown to be a critically damped waveform, with a full width half maximum of 0.3 ms. As the dust fall time is on the order of 100's of ms, any trigger delay from this waveform is considered negligible.

As tungsten (W) is a promising candidate for PFC's in many tokamak designs, micro machined, spherical W-25 dust from Tekna Plasma Systems Incorporated was chosen for this experiment. The Hitachi SU8010, FE-SEM at the University of Saskatchewan was used to image a representative sample of these dust particles. It was determined by measuring the sizes of 1,842 W dust particles, that their size distribution fit well to a lognormal distribution with parameters $\mu_d = 2.979$ and $\sigma_d = 0.265$. This results in a mean

particle diameter of 20.4 μm for unfiltered dust particles.

A test apparatus has been designed, constructed and utilized for characterization of the dust injector. The center piece of this apparatus is the test vacuum chamber, which can operate down to μTorr pressure ranges. This pressure is achieved with the use of the HiCube 80 vacuum pump. The chamber gas pressure may be adjusted with the use of a needle valve and monitored with a Kurt J. Lesker, cold-cathode Pirani gauge.

Mounted vertically at the top of the test chamber is the dust injector. Directly underneath the injector, a 3.0 cm wide laser sheath is directed through the symmetric, horizontal view ports of the chamber. This serves to illuminate tungsten dust particles which pass through the laser sheath after injection, via the scattering of laser light. In order to observe these injected dust particles, the Chronos 1.4 high speed camera was focused on the center of the laser sheath. The camera exposure duration is set low enough such that pixels are not saturated, though high enough that smaller dust particles are observed in the frame. Image frames have been recorded in this experiment at 2162 FPS with 6 dB gain. Particle elongation as a result of slight over exposure at these settings is found to be advantageous for dust particle identification, as small dust particles appear clearer within the frame.

The dust injector requires a mesh screen as part of its design, in order to control the mass of particles entering the vacuum chamber. Four different screens were tested for the dust injector, including sieve sizes of 5, 10, 14 and 20 μm's. For each individual screen, a calibration experiment was conducted. The experiment consisted of firing the dust injector 11 times at an injector pressure of 296 kPa, within the aforementioned test apparatus at injection voltages of 350, 400 and 450V for chamber pressures of 10^{-5} and 10^{-4} μTorr. Here, the camera and the dust injector share a common electrical trigger, ensuring proper timing of dust injection and data collection.

In order to track dust particle trajectories a PTV algorithm was developed. Firstly, the algorithm applies a Gaussian filter to 12 bit raw image frames, captured by the camera during the calibration experiment. A threshold is then set to produce binary images, simplifying the task of particle identification. Trackpy is then used in order to map dust

particles between successive image frames and subsequently determine their trajectories. From these trajectories, the velocity and spatial distributions of particles passing through the sheath during certain time intervals after dust injection are determined. Additionally, the average vertical velocity of particles found within the laser sheath is 1.8 m/s and this is not found to change significantly based on the injector parameters or screen. Furthermore, it is apparent from this data that free fall conditions are sufficient to explain the trajectory of particles observed in the laser sheath, with the addition of a small initial velocity, from the dust injector piston.

In order to determine the position of the dust plume dispersed from the dust injector at any arbitrary time after injection, the known trajectories of particles in the laser sheath are once again utilized. Since the dust injector and laser sheath positions are fixed, the initial velocities and injection times of dust particles relative to the injector trigger may be calculated with the assumption that gravity is the only active force. Based on this model, the dust plume is determined to reach the center of the STOR-M tokamak within an error range of +/- 0.4 cm at time, t = 298 +/- 3 ms after dust injection.

The total number of injected dust particles may be determined by considering the depth of field illuminated by the laser sheath and assuming conical symmetry of the dust plume. With this scheme, one may determine the fraction of dust particles which were not observed and scale the number of counted particles appropriately. Additionally, the average brightness of pixels across the camera frame was determined to be directly proportional to the number of injected particles. Thus, the PTV particle count may be corrected using this data. Finally, the total injected mass of particles is determined by multiplying the corrected number of particle observations by the average mass allowed through the dust injector screen. In the case of the 10 μm screen, the total injected mass was found to be 35 μg. This is theorized based on evidence from dust experiments in other tokamaks, to be on the threshold of injected dust particle mass which can be delivered into STOR-M, without total plasma disruption.

6.2 Future Work

Two primary setups are prepared for dust injection in STOR-M:

1. The dust injector will be mounted to a vertical port on the STOR-M tokamak. The dust injector will then be automatically triggered with appropriate delay, allowing for the desired W dust positioning within the tokamak. Normal CT injection may then be implemented.

2. The dust injector will be mounted to a vertical port of the CTI. W dust and gas may then be injected during CT formation. The resulting CT may then deposit dust directly into the core of the active STOR-M tokamak plasma.

Figure 6.1, illustrates the intended experiment in STOR-M.

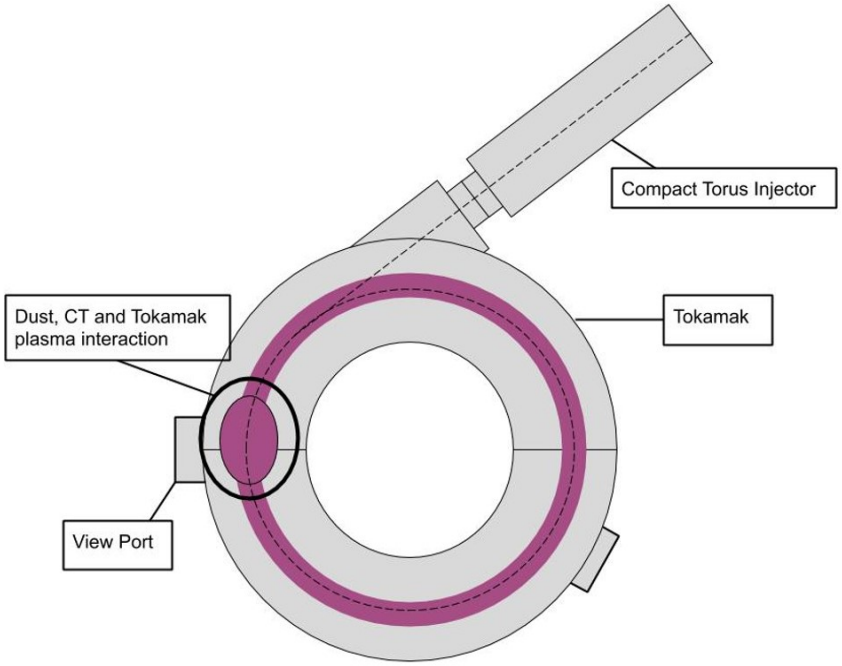

Figure 6.1: Proposed Dust Injection Experiment in STOR-M

Utilizing the light produced by the STOR-M discharge, we wish to track injected dust particles using the Chronos 1.4 high-speed camera. From this, we will be able to explore the effects of dust on plasma quality and stability, depending on the injected dust mass and location of dust particles within the tokamak. Due to the dust injector calibration analysis

in Chapter 5, mass and initial position of dust particles are controlled variables, thus the time evolution of dust particles within the tokamak may also be observed. Phenomena related to the various forces on dust particles and even plasma self cleaning [87] may be explored.

Dust particles are not noticeable under regular STOR-M operation, though a control experiment to determine background light intensity and other potential background particles will be implemented. This is simply accomplished by recording a normal STOR-M discharge with and without CT injection using the Chronos 1.4.

The initial dust injector parameters for the experiment in STOR-M have been determined from the characterization data in Chapter 5. The 10 μm screen has been chosen as the initial dust injector screen to be used on STOR-M. This is due to the 35 μg average injected mass of W dust determined to be filtered through the screen, which is within the target injection mass limit given by [48]. In order to achieve this mass of injected dust, the dust injector must operate at 400V with a fixed dust injector pressure of 296 kPa at test chamber pressures within the range of $10^{-}4$ - $10^{-}5$ Torr (STOR-M's operating pressure).

Current hydrogen gas puffing in STOR-M must respond on the order of ms for effectiveness. Due to the delay in dust injection, the dust injector gas puff will not serve to fuel the tokamak plasma.

Based on simulated data, which agrees with experimentally observed results from raw data, the position and evolution of the dust particle plume may be tracked in STOR-M. In particular, the center of mass of the dust injector plume is determined to reach the center of STOR-M within an error of +/- 0.4 cm, 298 +/- 3 ms after the dust injector trigger (utilizing the 10μm screen). This model of the dust plume enables us to gauge the initial condition of dust dispersed in STOR-M before plasma breakdown and analyze dust particle dynamics resulting from plasma interaction.

Bibliography

[1] Kulsrud R. M. *Plasma physics for astrophysics*. Princeton University Press, 2020.

[2] International Energy Agency. *Key world energy statistics*. Paris: International Energy Agency, 2007.

[3] S. H. Mohr et al. "*Projection of world fossil fuels by country*". In: *Fuel* 141 (2015), p. 120. DOI: 10.1016/j.fuel.2014.10.030.

[4] M. Tsoskounoglou, G. Ayerides, and E. Tritopoulou. "*The end of cheap oil: Current status and prospects*". In: *Energy Policy* 36(10) (2008), p. 3797. DOI: 10.1016/j.enpol.2008.05.011.

[5] C. Dinca A. Badea T. Apostol. "*Life cycle impact assessment of fossil fuels*". In: *U.P.B. Sci. Bull., Series C* 71(1) (2010), p. 115. URL: https://www.scientificbulletin.upb.ro/rev_docs_arhiva/full5321.pdf.

[6] International Energy Agency. *Key World Energy Statistics*. 2019. URL: https://www.iea.org/statistics/kwes/supply/ (visited on 06/15/2019).

[7] Chen F. F. *Introduction to plasma physics and controlled fusion*. Third Edition. Springer International Publishing, 2016.

[8] Fritz H. G. et al. "Differences in enthalpies of combustion and other related thermodynamic properties for regular and perdeuterated n-octane, isooctane, and benzene". In: *The Journal of Chemical Thermodynamics* 6(1) (1974), p. 75. DOI: 10.1016/0021-9614(74)90209-2.

[9] N. Afgan and M. Carvalho. "*Multi-criteria assessment of new and renewable energy power plants*". In: *Energy* 27 (2002), p. 739.

[10] D. Meade. "50 years of fusion research". In: *Nuclear Fusion* 50(1) (2009).

[11] Y. Shimomura et al. "*ITER: opportunity of burning plasma studies*". In: *Plasma Physics and Controlled Fusion* 71(12A) (2001), A385. DOI: 10.1088/0741-3335/43/12A/329.

[12] EUROfusion Consortium Research Institutions. *50 years of Lawson criteria*. 2005. URL: https://www.euro-fusion.org/news/detail/50-years-of-lawson-criteria/ (visited on 11/02/2020).

[13] J. Roth et al. "*Recent analysis of key plasma wall interactions issues for ITER*". In: *Journal of Nuclear Materials* 390-391 (2009), p. 1. DOI: 10.1016/j.jnucmat.2009.01.037.

[14] D. L. Rudakov et al. "*Dust measurements in tokamaks (invited)*". In: *Review of Scientific Instruments* 79(10) (2008), 10F303. DOI: 10.1063/1.2969422.

[15] M. Reinke et al. "*Avoidance of impurity-induced current quench using lower hybrid current drive*". In: *Nuclear Fusion* 59.066003 (2019). DOI: 10.1088/1741-4326/ab0eb2.

[16] Kleyn A. W., Lopes Cardozo N. J., and Samm U. "Plasma–surface interaction in the context of ITER". In: *Physical Chemistry Chemical Physics* 8(15) (2006), p. 1761. DOI: 10.1039/b514367e.

[17] G. Janeschitz. "*Plasma-wall interaction issues in ITER*". In: *Journal of Nuclear Materials* 290-293 (2001), p. 1. DOI: 10.1016/S0022-3115(00)00623-1.

[18] Brezinsek S. and JET-EFDA contributors. "*Plasma-surface interaction in the Be/W environment: Conclusions drawn from the JET-ILW for ITER*". In: *Journal of Nuclear Materials* 463 (2015), p. 11. DOI: 10.1016/j.jnucmat.2014.12.007.

[19] H. Bolt et al. "*Plasma facing and high heat flux materials – needs for ITER and beyond*". In: *Journal of Nuclear Materials* 307-311 (2002), p. 43. DOI: 10.1016/s0022-3115(02)01175-3.

[20] Y. Nobuta et al. "*Tritium retention properties of tungsten, graphite and co-deposited carbon film*". In: *Fusion Engineering and Design* 89(7-8) (2014), p. 1516. DOI: 10.1016/j.fusengdes.2014.04.004.

[21] Y. Ueda, K. Tobita, and Y. Katoh. "*PSI issues at plasma facing surfaces of blanketsin fusion reactors*". In: *Journal of Nuclear Materials* 313-316 (2003), p. 32. DOI: 10.1016/s0022-3115(02)01329-6.

[22] V. Barabash et al. "*Neutron irradiation effects on plasma facing materials*". In: *Journal of Nuclear Materials* 283-287 (2000), p. 138. DOI: 10.1016/s0022-3115(00)00203-8.

[23] M.Y. Ye et al. "*Blister formation on tungsten surface under low energy and high flux hydrogen plasma irradiation in NAGDIS-I*". In: *Journal of Nuclear Materials* 313-316 (2003), p. 72. DOI: 10.1016/S0022-3115(02)01349-1.

[24] Sabard J., Chaumeix N., and Bentaib A. "Hydrogen explosion in ITER: Effect of oxygen content on flame propagation of H2/O2/N2 mixtures". In: *Fusion Engineering and Design* 88(9-10) (2013), p. 2669. DOI: 10.1016/j.fusengdes.2013.02.128.

[25] M. Wirtz et al. "*Influence of helium induced nanostructures on the thermal shock performance of tungsten*". In: *Nuclear Materials and Energy* 9 (2016), p. 177. DOI: 10.1016/j.nme.2016.07.002.

[26] D. Allan et al. *soft-matter/trackpy*. Version 0.4.2. Oct. 16, 2019. DOI: 10.5281/zenodo.3492186.

[27] Harvard University. *Lorenz Effects*. 2020. URL: https://gmwgroup.harvard.edu/lorenz-effects (visited on 11/02/2020).

[28] Dave Burke. *Return of the Stellarator*. 2020. URL: https://lynceans.org/all-posts/return-of-the-stellarator/ (visited on 11/02/2020).

[29] Chen F. F. *Introduction to plasma physics and controlled fusion*. Vol. 1. New York: Plenum press, 1984.

[30] A. Hirose et al. "STOR-M Tokamak Design and Instrumentation". In: *Physics in Canada* March-April (2006), p. 111.

[31] Anthropocene Institute. *FUSION*. 2019. URL: https://www.anthropoceneinstitute.com/science/generation/fusion/ (visited on 11/02/2020).

[32] Stacey W. M. *Fusion plasma physics*. Second, Revised and Enlarged Edition. John Wiley & Sons, 2012.

[33] Eyink G. L. and Aluie H. "The breakdown of Alfvén's theorem in ideal plasma flows: Necessary conditions and physical conjectures". In: *Physica D: Nonlinear Phenomena* 223(1) (2006), p. 82. DOI: 10.1016/j.physd.2006.08.009.

[34] Turner W. C. et al. "Investigations of the magnetic structure and the decay of a plasma-gun-generated compact torus". In: *The Physics of fluids* 26(7) (1983), p. 1965.

[35] Olynyk G. and Morelli J. "Development of a compact toroid fuelling system for ITER". In: *Nuclear Fusion* 48(9) (2008). DOI: 10.1088/0029-5515/48/9/095001.

[36] Taylor J. B. "Relaxation of Toroidal Plasma and Generation of Reverse Magnetic Fields". In: *Physical Review Letters* 33(19) (1974), p. 1139. DOI: 10.1103/physrevlett.33.1139.

[37] Woltjer L. "A THEOREM ON FORCE-FREE MAGNETIC FIELDS". In: *Proceedings of the National Academy of Sciences* 44(6) (1958), p. 489. DOI: 10.1073/pnas.44.6.489.

[38] Geddes C. G. R.and Kornack T. W. and Brown M. R. "Scaling studies of spheromak formation and equilibrium". In: *Physics of Plasmas* 5(4) (1998), p. 1027. DOI: 10.1063/1.872632.

[39] Xiao C., Hirose A., and Sen S. "Improved confinement induced by tangential injection of compact torus into the Saskatchewan Torus-Modified (STOR-M) tokamak". In: *Physics of Plasmas* 11(8) (2004), p. 4041. DOI: 10.1063/1.1768177.

[40] M. Laberge et al. "*Acoustically Driven Magnetized Target Fusion*". In: *IEEE 25th Symposium on Fusion Engineering (SOFE)* (2013). DOI: 10.1109/sofe.2013.6635495.

[41] H. Gota et al. "*Achievement of field-reversed configuration plasma sustainment via 10 MW neutral-beam injection on the C-2U device*". In: *Nuclear Fusion* 57(11) (2017). DOI: 10.1088/1741-4326/aa7d7b.

[42] Raman R. et al. "Experimental demonstration of tokamak fuelling by compact toroid injection". In: *Nuclear Fusion* 37(7) (1997), p. 967. DOI: 10.1088/0029-5515/37/7/i05.

[43] A. Rohollahi. "*Experimental Studies Using Compact Torus Injector*". PhD thesis. University of Saskatchewan, 2017.

[44] Liu Z., Wang D., and Miloshevsky G. "Simulation of dust grain charging under tokamak plasma conditions". In: *Nuclear Materials and Energy* 12 (2017), p. 530. DOI: 10.1016/j.nme.2016.11.030.

[45] Thoma A. et al. "Spectroscopic measurements of tungsten erosion in the ASDEX Upgrade divertor". In: *Plasma Physics and Controlled Fusion* 39(9) (1997), p. 1487. DOI: 10.1088/0741-3335/39/9/014.

[46] Makhlaj V. A. et al. "Dust generation mechanisms under powerful plasma impacts to the tungsten surfaces in ITER ELM simulation experiments". In: *Journal of Nuclear Materials* 438 (2013), S233. DOI: 10.1016/j.jnucmat.2013.01.034.

[47] M. Mikikian et al. "*Dusty plasmas: synthesis, structure and dynamics of a dust cloud in a plasma.*" In: *The European Physical Journal Applied Physics* 49.13106 (2009). DOI: 10.1051/epjap/2009191.

[48] R. D. Smirnov et al. "*Tungsten dust impact on ITER-like plasma edge*". In: *Physics of Plasmas* 22.012506 (2015). DOI: 10.1063/1.4905704.

[49] A. Denkevits. "*Hydrogen/dust explosion hazard in ITER: Effect of nitrogen dilution on explosion behavior of hydrogen/tungsten dust/air mixtures*". In: *Fusion Engineering and Design* 85 (7-9 2010), p. 1059. DOI: 10.1016/j.fusengdes.2010.01.009.

[50] Senichenkov I. Y. et al. "On mechanisms of impurity leakage and retention in the tokamak divertor". In: *Plasma Physics and Controlled Fusion* 61(4) (2019). DOI: 10.1088/1361-6587/ab04d0.

[51] Chen Y. et al. “Measurement and analysis of Z eff in EAST tokamak”. In: *Plasma Physics and Controlled Fusion* 56(10).105006 (2014).

[52] Smirnov R. D. et al. “Laser-dust interaction and dust size distribution measurements on DIII-D”. In: *Physics of Plasmas* 14(11) (2007). DOI: 10.1063/1.2807025.

[53] Pitts R. A. et al. “Material erosion and migration in tokamaks”. In: *Plasma Physics and Controlled Fusion* 47(12B) (2005), B303. DOI: 10.1088/0741-3335/47/12b/s22.

[54] Pitts R. A. et al. “Status and physics basis of the ITER divertor”. In: *Physica Scripta* T138 (2009). DOI: 10.1088/0031-8949/2009/t138/014001.

[55] Reimold F. et al. “Experimental studies and modeling of complete H-mode divertor detachment in ASDEX Upgrade”. In: *Journal of Nuclear Materials* 463 (2015), p. 128. DOI: 10.1016/j.jnucmat.2014.12.019.

[56] Linke J. et al. “High heat flux testing of plasma facing materials and components – Status and perspectives for ITER related activities”. In: *Journal of Nuclear Materials* 367-370 (2007), p. 1422. DOI: 10.1016/j.jnucmat.2007.04.028.

[57] Shalpegin A. et al. “Fast camera observations of injected and intrinsic dust in TEXTOR”. In: *Plasma Physics and Controlled Fusion* 57(12) (2015). DOI: 10.1088/0741-3335/57/12/125017.

[58] Brown B. T., Smirnov R. D., and Krasheninnikov S. I. “On vapor shielding of dust grains of iron, molybdenum, and tungsten in fusion plasmas”. In: *Physics of Plasmas* 21(2) (2014). DOI: 10.1063/1.4866599.

[59] Smirnov R. D. et al. “Modelling of dynamics and transport of carbon dust particles in tokamaks”. In: *Plasma Physics and Controlled Fusion* 49(4) (2007), p. 347. DOI: 10.1088/0741-3335/49/4/001.

[60] A. M. Ignatov. “Basics of dusty plasma”. In: *Plasma physics reports* 31(1) (2005), p. 46. DOI: 10.1134/1.1856707.

[61] Tang X.-Z. and Luca Delzanno G. "Orbital-motion-limited theory of dust charging and plasma response". In: *Physics of Plasmas* 21(12) (2014). DOI: 10.1063/1.4904404.

[62] Bacharis M., Coppins M., and Allen J. E. "Dust in tokamaks: An overview of the physical model of the dust in tokamaks code". In: *Physics of Plasmas* 17(4) (2010). DOI: 10.1063/1.3383050.

[63] Thomas E. W. "Particle induced electron emission". In: *Atomic and plasma-material interaction data for fusion, Suppl. to Nuclear Fusion* 1 (1991), p. 79.

[64] Hippler S., Hasselkamp D., and Scharmann A. "The ion-induced electron yield as a function of the target material". In: *Nuclear Instruments and Methods in Physics Research Section B: Beam Interactions with Materials and Atoms* 34(4) (1988), p. 518. DOI: 10.1016/0168-583x(88)90160-7.

[65] Vaverka J. et al. "The influence of secondary electron emission on the floating potential of tokamak-born dust". In: *Plasma Physics and Controlled Fusion* 56(2) (2014). DOI: 10.1088/0741-3335/56/2/025001.

[66] Martin J. D. et al. "Modelling of dynamics and transport of carbon dust particles in tokamaks". In: *Modelling dust transport in tokamaks. EPL (Europhysics Letters)* 83(6) (2008). DOI: 10.1209/0295-5075/83/65001.

[67] Krasheninnikov S. I. et al. "On dust dynamics in tokamak edge plasmas". In: *Physics of Plasmas* 11(6) (2004), p. 3141. DOI: 10.1063/1.1724834.

[68] Shukla P. K. and Tsintsadze N. L. "Charged dust grain acceleration in tokamak edges". In: *Physics Letters A* 372(12) (2008), p. 2053. DOI: 10.1016/j.physleta.2007.08.074.

[69] Tsytovich V. N., Sato N., and Morfill G. E. "Note on the charging and spinning of dust particles in complex plasmas in a strong magnetic field". In: *New Journal of Physics* 5 (2003). DOI: 10.1088/1367-2630/5/1/343.

[70] Krasheninnikov S. I. "Modeling of Dust Particle Transport in Tokamak Plasmas". In: *AIP Conference Proceedings* (2005). DOI: 10.1063/1.2134575.

[71] Khrapak S. A. et al. "Ion drag force in complex plasmas". In: *Physical Review E* 66(4) (2002). DOI: 10.1103/physreve.66.046414.

[72] Ajay K. and Pandya S. P. "Experimental Results of Core Ion Temperature and Neutral Density Measurements on ADITYA Tokamak using Four Channels Neutral Particle Analyzer". In: *Journal of Fusion Energy* (2020). DOI: 10.1007/s10894-020-00245-6.

[73] Banerjee S. et al. "Observations of H_α emission profiles in Aditya tokamak". In: *J. Plasma Fusion Res* 9 (2010), p. 29.

[74] Liu B. et al. "Radiation pressure and gas drag forces on a melamine-formaldehyde microsphere in a dusty plasma". In: *Physics of Plasmas* 10(1) (2003), p. 9. DOI: 10.1063/1.1526701.

[75] T. Onchi et al. "*Development towards a Repetitive Compact Torus Injector*". In: *IEEE Transactions Plasma Science* 44(2) (2016), p. 195.

[76] A. Pant. "*Repetitive Operation of the University of Saskatchewan Compact Torus Injector*". MA thesis. University of Saskatchewan, 2009.

[77] Thompson Marc T and Ph. D. *Inductance Calculation Techniques — Part II: Approximations and Handbook Methods*. 1991.

[78] Dassault Systèmes. *SolidWorks 2018*. Vélizy-Villacoublay, France.

[79] E. Bernard et al. "*Tungsten dust in fusion tokamaks: relevant dust laser production, characterization and behaviour under tritium loading*". In: *Physica Scripta* 2016.T167 (2016). DOI: 10.1088/0031-8949/T167/1/014071.

[80] V Rohde et al. "*Dust investigations at ASDEX Upgrade*". In: *Physica Scripta* 2009.T138 (2009). DOI: 10.1088/0031-8949/2009/T138/014024.

[81] T. Onchi et al. "*Design and implementation of fast charging circuit for repetitive compact torus injector*". In: 89(11) (2014), p. 2559.

[82] Digi-Key Electronics. *Scheme-it*. URL: https://www.digikey.ca/en/resources/design-tools/schemeit (visited on 09/25/2020).

[83] Schindelin J. et al. “Fiji: an open-source platform for biological-image analysis”. In: *Nature methods* 9(7) (2012), p. 676. DOI: 10.1038/nmeth.2019.

[84] Crocker J. C.and Grier D. G. “Methods of digital video microscopy for colloidal studies”. In: *Journal of colloid and interface science* 179(1) (1996), p. 298. DOI: 10.1006/jcis.1996.0217.

[85] Umbaugh S. E. *Digital image processing and analysis: human and computer vision applications with CVIPtools*. CRC press, 2010.

[86] Moran M. J., Boettner D. D. Shapiro H. N., and Bailey M. B. *Fundamentals of engineering thermodynamics*. John Wiley & Sons, 2010.

[87] Krasheninnikov S. I., Smirnov R. D., and Rudakov D. L. “Dust in magnetic fusion devices”. In: *Plasma Physics and Controlled Fusion* 53(8) (2011). DOI: 10.1088/0741-3335/53/8/083001.